2018

Polymorphic transformations in oxides and metals processed by electric discharge assisted mechanical milling: indirect assessment of plasma temperature via microscopic and crystallographic approach

Monika Wyszomirska

University of Wollongong

POLYMORPHIC TRANSFORMATIONS IN OXIDES AND METALS PROCESSED BY ELECTRIC DISCHARGE ASSISTED MECHANICAL MILLING: INDIRECT ASSESSMENT OF PLASMA TEMPERATURE VIA MICROSCOPIC AND CRYSTALLOGRAPHIC APPROACH

Monika Wyszomirska

Supervisors:

Prof. Andrzej Calka, Dr. David Wexler

This thesis is presented as part of the requirement for the conferral of the degree of

Doctor of Philosophy

The University of Wollongong
School of Engineering and Information Sciences

March ,2018

Certification

I, Monika Wyszomirska, declare that this thesis submitted in fulfilment of the requirements for the conferral of the degree Doctor of Philosophy, from the University of Wollongong, is wholly my own work unless otherwise referenced or acknowledged. Thisdocument has not been submitted for qualifications at any other academic institution.

Monika Wyszomirska

29.03.2018

Abstract

The aim of the following thesis was to develop a fundamental understanding about the processing temperatures and mechanisms occurring during Electric Discharge Assisted Mechanical Milling (EDAMM). This was done through processing of a variety of materials which exhibit a phase transformation or polymorphic transformation in a known temperature.

A series of experiments using metal (Al, Mn, Ti, Cr), non-metal (Si, C) and oxide (TiO_2, $BaTiO_3$) starting powders was designed to estimate the minimum and maximum temperatures during EDAMM processing in inert Argon atmosphere and stainless steel electrode. The minimum processing temperature in these conditions was estimated according to the Al melting point and Mn polymorphic transformations. Intermediate processing temperature was determined from Ti+Cr and $BaO+TiO_2$ processed powders to form mixtures of low and high temperature stable $TiCr_2$ and $BaTiO_3$ polymorphs. The maximum processing temperature determination was done using Si+C powders reacted to form β-SiC phase. From these initial experiments the minimum temperature of 600°C and a maximum temperature <1600°C was determined. In additional series of experiments, two modifications of the conditions were studied by introducing (i) a TaC coating on the stainless steel ball electrode and (ii) changing the pure Ar atmosphere to $10\%O_2$/Ar gas. It was found that in both modifications the discharge affected surface of the EDAMM chamber is more uniform. On the other hand, temperature measurements showed that the TaC coating on the EDAMM electrode resulted in lowering of the processing temperature, whereas $10\%O_2$/Ar gas results in its increase.

Taking into account the abovementioned processing modifications, an in-depth investigation of their influence on the phase formations sequences from $BaO+TiO_2$ starting powders and the subsequent cubic↔hexagonal $BaTiO_3$ polymorphic transformation was done. The crystal structures were identified through XRD

whereas microstructure and elemental analysis was done via SEM/EDS and TEM. In the first type of modification, when introducing the TaC coating on the ball electrode, the initial stages of the processing revealed formation of nanometer sized powder particles with orthorhombic crystal structure and elemental composition consistent with $BaTiO_3$. Further processing resulted in the orthorhombic→cubic $BaTiO_3$ transformation and formation of the monoclinic $Ba_2Ti_6O_{13}$ secondary phase, both of which persisted until the end of the processing. Cubic $BaTiO_3$ is considered stable until ~1430°C if stoichiometric amounts of BaO and TiO_2 are used as a starting material, above which it typically transforms into the high temperature hexagonal polymorph. Second modification of the processing conditions, where BaO+TiO_2 starting powders were processed in 10%O_2/Ar atmosphere, showed a result consistent with the previous observations where the processing temperature was higher than when using the TaC coated electrode. Here, the initial stages of EDAMM processing revealed simultaneous formation of low temperature cubic and high temperature stable hexagonal $BaTiO_3$. After further processing only high temperature hexagonal $BaTiO_3$ polymorph, stable above ~1430°C, and a monoclinic $Ba_2Ti_6O_{13}$ secondary phase were sustained.

Thus, it was concluded that the TaC coating applied on the stainless steel electrode reduces the temperature of the processing. Additional analysis of the TaC coating revealed that it is not continuous and therefore decreases the plasma discharge energy by decreasing the area available for the electrons to escape the electrode. On the contrary, the 10%O_2/Ar atmosphere increased the processing temperature due to the higher energy of O_2 species in comparison to the pure Ar gas.

Cross-sectional areas of selected $BaTiO_3$ powder particles which undergone the EDAMM processing using a TaC coated ball electrode and the 10%O_2/Ar gas, were then analyzed by a new, advanced computational method developed at the UOW. This post-processing method allows for the phase and texture evolution analysis based on the crystallographic data obtained through EBSD and TEM, to develop phase

formation mechanisms. Firstly, orientation relationships between cubic $BaTiO_3$, hexagonal $BaTiO_3$ and monoclinic $Ba_2Ti_6O_{13}$ phases were found using selected area electron diffraction (SAED). EBSD mapping was performed on the cross-sectional areas of the selected particles and in conjunction with the orientation relationship data used to define the compliance or deviation of the interphase boundaries from the ideal orientation with the computational method. It was found that the deviation of the interphase boundary from the ideal orientation relationship correlates with the point in time when these boundaries were created. As a result, it was concluded that the monoclinic $Ba_2Ti_6O_{13}$-cubic $BaTiO_3$ interphase boundaries were formed at the beginning of the phase's formations and deformed due to the grain growth and plastic deformation occurring during EDAMM. Cubic $BaTiO_3$-hexagonal $BaTiO_3$ interphase boundaries were found to conform to the ideal orientation relationship to much greater extent which infers several conclusions; (i) the cubic-hexagonal orientation relationship found through SAED is the dominant relationship in this phase transformation regime, (ii) the cubic→hexagonal transformation occurred by the end of the EDAMM processing and (iii) the powder particles in EDAMM are cooled extremely fast as the high temperature hexagonal $BaTiO_3$ polymorph is sustained in the room temperature.

The above presented research gives new insights into the capabilities and limitations of EDAMM, how to control its processing parameters to affect EDAMM temperature, and the mechanisms that govern phase and polymorphic transformations induced under different processing conditions.

List of PhD related publications

I.S. Aisyah**, M. Wyszomirska**, A. Calka, D. Wexler, *Rapid Transformation of Hexagonal to Cubic Silicon Carbide (SiC) by Electric Discharge Assisted Mechanical Milling,* Plasma Chemistry and Plasma Processing, 36, 4 (2016) 1177–1186

I.S. Aisyah, **M. Wyszomirska**, A. Calka, D. Wexler*, Nitrogenation of hafnium carbide powders in AC and DC plasma by Electrical Discharge Assisted Mechanical Milling*, Journal of Alloys and Compounds, 715, 25 (2017) 192-198

Acknowledgments

I am grateful to the UOW for matching scholarship (Australian Research Council Discovery Grant DP130101390), which made it possible to perform the work presented in this thesis.

I would like to thank my supervisors Prof. Andrzej Calka and Dr. David Wexler for continuous support throughout the PhD project and offering a kind word in the time of doubt. I would like to give my sincere gratitude to Dr. Mitchell Nancarrow and Tony Romeo for help in sample preparation and scanning electron microscopy. I am particularly grateful to Dr. Azdiar Gazder, who provided his expertise in electron backscattering diffraction and his newly developed EBSD analysis tool. I'd like to also thank Dr. Gilberto Cassias Garcia for his expertise and sharing his knowledge in transmission microscopy field. Finally, to all EMC staff for their help when using the facilities, from training to the in-depth analysis of the research problems.

I would also like to thank all my international friends who made the research life so much more enjoyable; Pragathi, Cissy, Ali, Nick, Navjeet, Chinmay, Yvonne, Myrto, Nuria, Kaza and Robo. My special thanks go to my dear boyfriend Clint for patience during the tough times and encouragement throughout the whole period, no matter what the circumstances. To Ania Kosińska, Ania Jarka, Martyna, Gosia, Marta and Agata, and many others back in Poland, for remaining friends despite the distance and lifting my spirits when back at home.

Szczególne podziękowania składam moim rodzicom Leszkowi i Barbarze Wyszomirskim oraz mojej siostrze Kindze, którzy wspierali mnie przez cały okres doktoratu i umożliwili mi edukację w Polsce i Australii.

Notation

BCT	Body Centered Tetragonal
DC	Direct Current
EBSD	Electron Backscattering Diffraction
EDAMM	Electric Discharge Assisted Mechanical Milling
EDS	Energy Dispersive Spectroscopy
FCC	Face Centered Cubic
HAB	High Angle Boundary
HRTEM	High Resolution Transmission Electron Microscopy
LAB	Low Angle Boundary
OR	Orientation Relationship
ORBs	Orientation Relationship Boundaries
SEM	Scanning Electron Microscopy
TEM	Transmission Electron Microscopy
XRD	X-ray Diffraction

Table of Contents

List of Figures

CHAPTER 1

CHAPTER 2

CHAPTER3

CHAPTER 4

CHAPTER 5

List of Tables

CHAPTER 1

Literature review

In the following thesis, an influence of the electric discharge assisted mechanical milling (EDAMM) processing conditions on phase transformations is presented. Since the method comprises of both milling and plasma treatment elements, following review includes the current methods, which may assist in better understanding of EDAMM. These include; solid-state and mechanochemical processing such as ball milling and current plasma methods, which resemble the EDAMM set-up.

1.1 Mechanochemical synthesis

Mechanochemical processing of the powders is a common method for powders synthesis especially when non-equilibrium conditions are of the essence [1]. This process is based on interactions between the surfaces of the milling balls and milling chamber with powders mixed in stoichiometric ratios that define the final product. Depending on the setting of the process, powder particles are subjected to shear, compression or impact forces to form new and fresh surfaces. The accumulation of energy in the powders and their defective structure are typical results of such kind of processing as is the synthesis of metastable, intermetallic or amorphous phases, as well as extended solid-solutions and high temperature ceramics that are difficult to obtain [2]. Some powder mixtures may also experience a self-sustaining reaction induced by ball milling [3] where, initially, activation of the powders occurs after which ignition and combustion propagation takes place. These reactions rarely come to the completion right after ignition and therefore further milling is needed to obtain homogeneous and fully processed material.

Efficiency of ball milling can be improved by using a magnetic field to control ball movement (Fig. 1.1). Magnets positioned in specific areas adjacent to the milling chamber impart larger forces onto the balls in both shear and impact, and this proved to be suitable for processing high melting point intermetallics such as TiB_2 or Fe_2B [4].

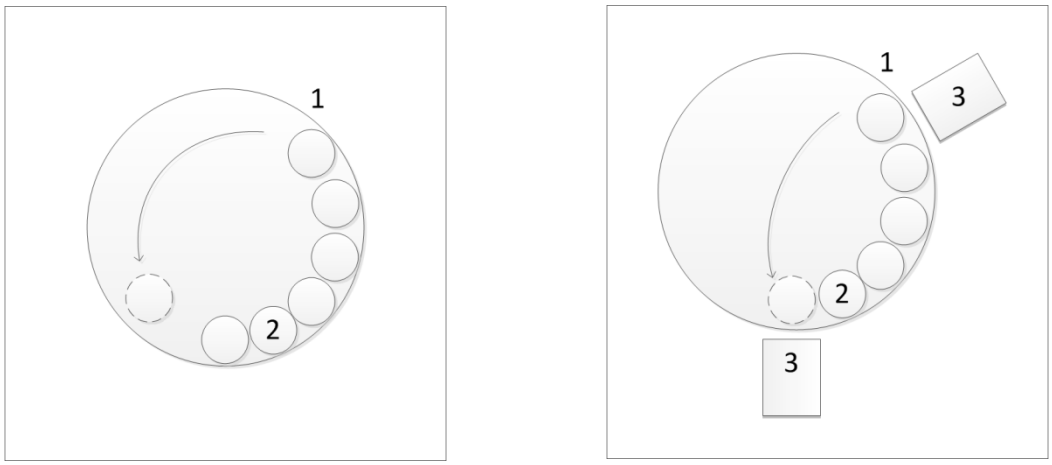

(a) (b)

Figure 1. 1: Schematic of the movement of the ball in (a) traditional ball milling device, impact mode and (b) enhanced ball force due to the magnetic field. Legend: 1- ball milling chamber, 2- milling balls and 3- magnets. (images based on [5])

As well as the milling equipment set up, the characteristics of the powders also play an important role in the processing mechanism. Ductile powders processing involves flatten the particles trapped between the surfaces of the balls as they undergo plastic deformation. Further processing of as-obtained powders with flat surfaces may lead to cold-welding and subsequent fracturing [6]. It is generally agreed that brittle powders processing is different as it does not rely on the alloying component. Ceramic powders with brittle-brittle components undergo continuous fragmentation until no further reduction in size is possible. Diffusion in materials such as brittle oxides is extremely limited; some researchers argue that it can be induced by plastic deformation or a local increase in temperature, while others state that diffusion does not occur in these conditions or at least does not play a significant role in processing [7]. Processing these powders often result in a nanocrystalline structures [8] and often an additional calcination at high temperatures is needed to allow for final phase formation [9]. As pointed out in the review of [10], we are yet to describe precisely the mechanisms which govern the formation of the phases under high energy ball milling conditions, so further investigation into the variety of alloys and compounds is needed.

1.2 Plasma assisted powder synthesis methods

Mechanical alloys and subsequent arc discharging

Improvement on the synthesis rates through ball milling can be achieved by subsequent arc discharging. As an example, it was previously observed that 7 hours of ball milling Ti and C powders in N_2 atmosphere resulted in a Ti(C,N) phase, but when the powders were milled for 1 hour and then subjected to arc discharging for 0.5-3 min, the Ti(C,N) phase was the major phase present[11]. Moreover, the longer the pre-milling time the more Ti(C,N) phase was detected. This result showed that arc discharge accelerated the transformation of raw material and therefore the overall efficiency is due to arc discharging and previously activated powders.

Dielectric Barrier Discharge Plasma

It was found in [12], that the efficiency of mechanosynthesis can be also increased when directly coupled with plasma heat treatment. This so-called "dielectric barrier discharge plasma assisted milling" was patented in 2009; a schematic image of this device is shown in Fig. 1.2. In this set up the electrode is suspended inside the chamber and remains stationary while milling takes place via the stainless steel balls in the milling chamber. An alternating current applied through the 22kV power supply is formed between the electrode inserted into the chamber and the stainless steel processing chamber, whereas mechanical milling occurs as the chamber vibrates. DBDP proved to be an efficient process for lowering the temperature of V_2O_5-C deoxidation [13], synthesizing WC [14] and AlN [15], surface modifications[16] and shortening the time required to decrease the particle size compared to traditional ball milling [17].

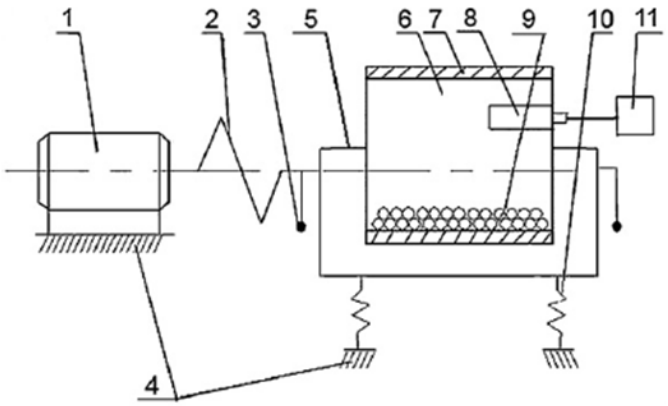

Figure 1.2: DBDP milling device components: electromotor (1), elastic joint (2), vibration exciter (3), base plate (4), framework (5), vial (6), refrigerant tank (7), electrode (8), steel balls (9), spring (10), DBDP power supply (11) [14].

1.3 Plasma synthesis of oxides by Electric Discharge Assisted Mechanical Milling (EDAMM)

The Electric Discharge Assisted Mechanical Milling (EDAMM) method enables powders to be synthesized by mechanical impact, similar to the impact mode of the ball milling method and simultaneous heat treatment of powders through pulsed electric discharges[18]. The setup and parameters are described in detail in "*Chapter 2 Materials Synthesis and Characterisation Methods"* whereas here the literature review on previous EDAMM studies is presented.

EDAMM is only available at the University of Wollongong where it was invented and developed therefore a literature review of the materials which were process is limited. Despite that fact, previous work can shed some light on the possibilities and capabilities of this unique processing method, which is explored further in the following thesis.

At present, experiments such as synthesis, decomposition, solubility, storage and transformation have proven the versatility of EDAMM. In terms of oxide processing, there are many publications, which analyse the relationship between processing conditions and the resulting compound synthesis. One of the earliest examples is the reduction reaction of hematite (α-FeO) to magnetite (Fe_3O_4) in N_2 atmosphere [19] which showed that Electric Discharge Assisted Ball Milling can reduce reaction time to 30 minutes, rather than the 20 hours needed for traditional ball milling. It was found that non-conductive oxides processed in hot milling conditions tend to fracture much more than conductive metals; this of course has implications for the final particle sizes.

Further work involved the synthesis of more complex oxides such as $LiCoO_2$, $LiFePO_4$ and $SrTi_{1-x}Co_xO_3$ from elemental oxides [20, 21]. For example, the optimisation of processing conditions for $LiFePO_4$ processed in N_2+3%H_2 atmosphere and AC mode, reduced the synthesis time to 10 minutes. Based on particles morphology, it was concluded that using high power during milling tend to melt the powder particles, whereas low power processing results in more porous particles with high specific surface area. $LiCoO_2$ synthetised from $LiCO_3$ and Co_3O_4 was processed for 10 min and resulted in fully processed powder, whereas had it been ball milled it would have taken more than 100h. The primary concern of Li evaporation during milling was not substantiated because the chemical composition of the final compound had an almost 1:1 Li to Co ratio. Moreover, processing under low power resulted in finer crystallites (43nm) than under high power processing (227nm). EDAMM proved to be a suitable tool for high temperature oxide synthesis as well, but it would typically require sintering temperatures over 1000°C. Thus, $SrTiO_3$, whose sintering temperature oscillates around 1100°C, was synthetised from elemental oxides in 10 min. The substitution of Ti by Co was achieved via a stoichiometric addition of CoO to the starting powders, and a range of substitutions from 10-50%Co in $SrTi_{1-x}Co_xO_3$ was successfully prepared.

Other typical high temperature reactions such as the reduction reaction of $FeTiO_3$ in Ar which also resulted in TiC/Fe_3C composite [22] were also examined. In this instance the reaction was completed within 5 min of processing, so the authors predicted that due to the powders morphology, the temperatures in EDAMM could possibly exceed 3000°C. This study was then expanded by exploring the influence of different atmospheres on the reactivity of ilmenite ($FeTiO_3$) powders such as CO_2, N_2, Ar, O_2 and air [23]. Starting powders of ilmenite and pseudorutile ($Fe_2Ti_3O_9$) were processed for 10 minutes, with the result that in all atmospheres pseudorutile was reduced to preudobrookite, and with O_2 and air, the reduction was complete and no ilmenite peaks were found by the X-ray diffraction patterns. That transformation typically takes place after the powder's reactivity has been increased by ball milling and sintering in Ar at 1400°C [24]; this again proved that EDAMM can substitute two processing steps with one.

One of the latest studies on processing oxide powders in EDAMM was done on $MgAl_2O_4$, $BaLa_2Ti_4O_{12}$ and $CaCu_3Ti_4O_5$ [25] by varying the processing atmosphere and the type of electric discharge. $MgAl2O_4$ was produced from oxides and metals in DC and AC modes and Ar, N_2, O_2 and He atmospheres for 15 min. XRD analysis suggested that processing the elemental oxides in N_2 atmosphere results in less unreacted powders. Moreover, an AC discharge used in these conditions proved to have the same effect. Further analysis of the XRD spectra led to the conclusion that AC discharge leads to substantial increased amount of nucleation sites but relatively limited growth of the grains, whereas a higher temperature DC discharges induced grain growth in this oxide. The CCT product on the other hand processed for 15 minutes in EDAMM in DC and Ar, showed nearly no peaks which could be matched to the final product. Further heat treatment in 1110°C in DTA resulted in a pure phase of CCT. $BaLa_2Ti_4O_{12}$ on the other hand was produced readily in EDAMM under the same conditions and the peaks matched the aimed phase very well.

A comparison between EDAMM and ball milling was done in [26] for $MgAl_2O_4$ and $CaCu_3Ti_4O_5$ compounds. The nanostructural character of the powders was recognised after 120 hours of ball milling, whereas EDAMM gave the same result after only 10 minutes of processing in Ar. Additionally, di-electric properties of EDAMM processed CCT proved to be an order of magnitude better than ball milled and sintered pellets.

All the materials presented above proved that the EDAMM method could produce compounds within minutes by mixing the stoichiometric powders of elemental oxides. The resulting powders have good dielectric properties and in many cases the final product can be tailored towards specific outcomes.

1.4 EDAMM plasma characteristics

1.4.1 Direct current pulsed plasma

The power used in the EDAMM set-up can be used to supply alternating current or direct current, but in this thesis only direct current (DC) discharge was used for all the processed materials (Fig. 1.3a-c). The discharge is supplied in a pulsed manner to prevent melting of the powder particles. As a result, ratio between the times when the discharge exists to the time when it's extinguished can be regulated. In this thesis, this parameter is called a "pulse on/off ratio" and is given as a percentage of the maximum pulse length until it is considered a continuous current flow. The pulse intensity can be regulated as well and is further given as a percentage of the maximum voltage. Consequently, the discharge energy increases with larger pulse on/off ratio and larger pulse intensity.

The direct current used in this thesis for all the experiments is thought to supply highly localised, branch-shaped discharges (Fig. 1.3c). When this kind of processing is applied to brittle powders such as oxides it is believed to increase the efficiency of phase transformation and facilitate new surface formation when coupled with

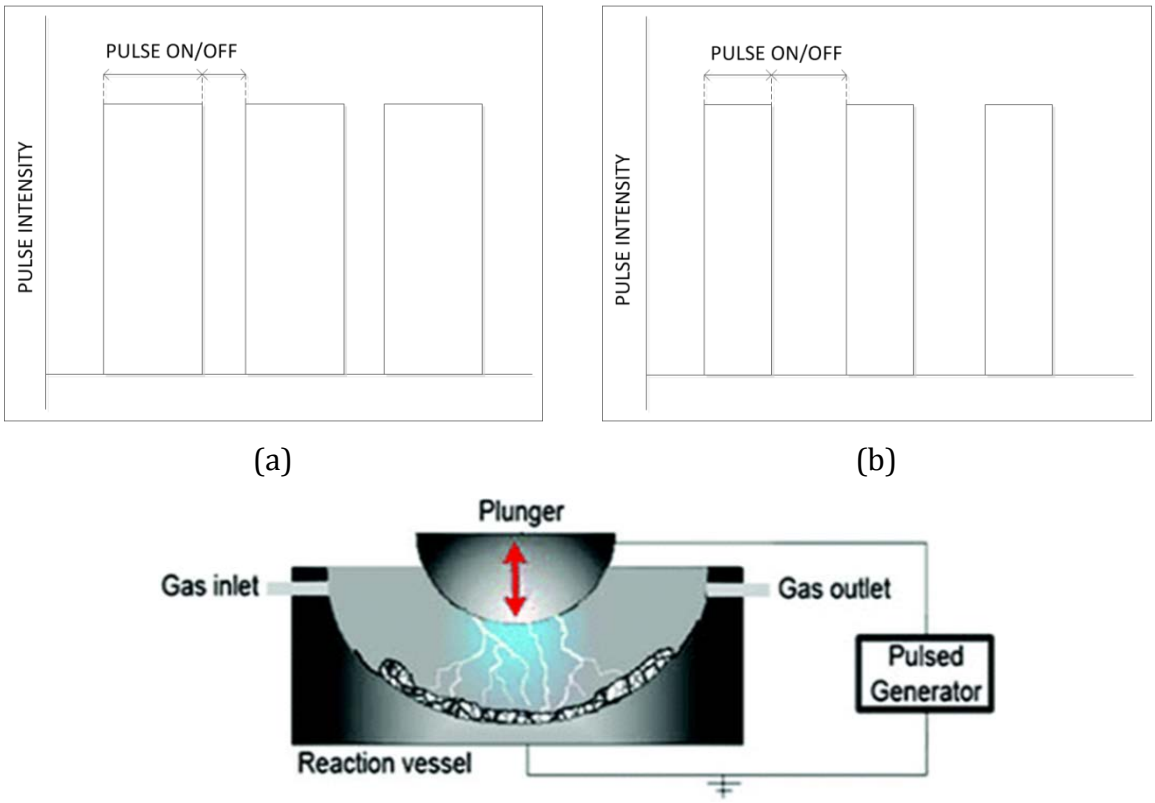

Figure 1.3: Schematic representation of (a) high pulse on/off ratio and high pulse intensity, (b) low pulse on/off ratio and high pulse intensity and (c) DC discharge distribution in EDAMM processing chamber.

mechanical milling. It is thought, that due to the pulsed character of discharges, powder particles are heated to a high temperature and then rapidly cooled down due to the short time of the discharge affecting the particles. Therefore, it is possible to obtain phases which are stable high temperature and preserve them in room temperature.

The discharge created due to the difference in the potential of the electrodes also depends on the vibration and the distance between them. Electrodes are normally connected to current flows without interruption but when this distance has increased plasma is created to retain the current flow. When this distance is fairly small, high

density plasma can be obtained, but as the distance increases the plasma has lower density, greater heat dissipation, and with pulsed plasma, the current flow can disappear and therefore the plasma is terminated. It must be realised that the character of pulsed plasma means that the pulse on/off ratio and pulse intensity must be considered simultaneously.

1.4.2 Dusty plasma

Dusty plasma is a complex mixture of electrons, ionized particles, metastable atoms, ions and neutral species that are referred to as dust particles. Within a dusty plasma environment, processes such as elastic and inelastic scattering, and ionization or excitation take place. The most mobile species in this system are electrons because they interact with each other (Townsend avalanche), and this allows for the gas to be conductive [21, 27]. Additionally, the power supply used in EDAMM is designed to induce plasma suitable to effectively enhance kinetic energies of the ions and allow formation in highly reactive species such as free radicals.

Gas atoms and molecules contained in the EDAMM processing chamber may undergo dissociation (di-atomic gases) and/or ionization (mono-atomic gases) as a result of the flow of electrons (Fig. 1.4a). All of the species interact with dust particles (Fig. 1.4b), during which various processes increase their energy enough to allow for phase transformations. These energies include Joule heating, also known as resistive heating, and recombination on the surface of the particles

It is though that dust particles increase the efficiency of the synthesis but they may also be a source of contamination due to current flow from the ball electrode to the stainless steel reaction vessel. The surface of the electrode erodes over time because atoms are detached from the surface during the initial part of the discharge and then transferred to the processed powder material. However, the amount or type of “contamination” can be changed by coating the electrode or leaving it “dirty” after the previous experiment.

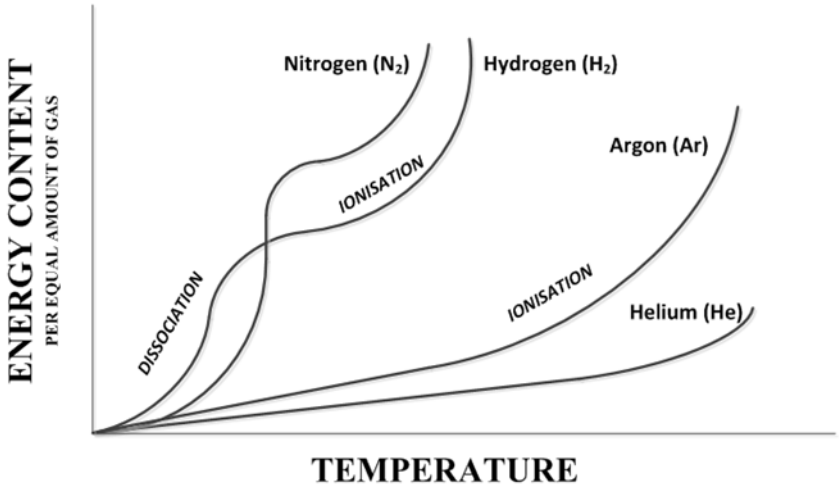

(a)

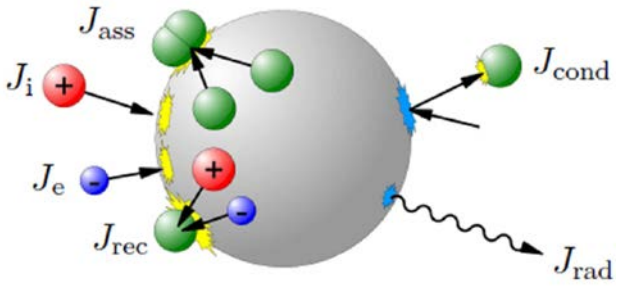

(b)

Figure 1.4: a) Energy content of various gases versus temperature graph and b) and flux densities between the particle and plasma environment [28].

CHAPTER 2

Experimental and analytical methods

2.1 Electric Discharge Assisted Mechanical Milling (EDAMM)

EDAMM is a custom-made device which incorporates plasma treatment and the mechanical milling of powders. An EDAMM chamber is confined within a stainless steel base, a polymer cylinder and a lid; the whole device stands on a vibrating plate. The lid is connected to a high voltage power supply and an electrode is suspended from the lid over the plasma chamber. The electrode is a conducting stainless steel ball that hits the powders when vibration is present and through local contact with the stainless steel base, plasma is created (Fig.1). The type of plasma environment created between the electrodes depends on whether the current is direct or alternating (DC or AC). In DC mode the plasma is more localised when passing through the powders, whereas in AC mode in the plasma is a more uniform, glow discharge type.

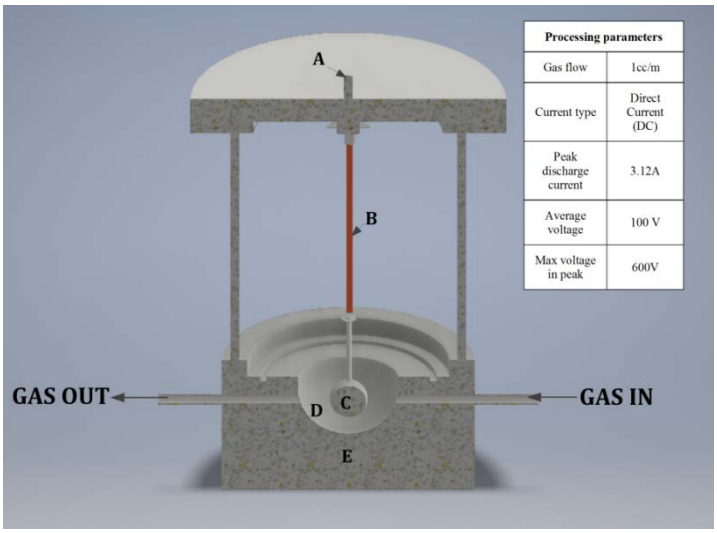

Figure 2. 1: Schematic of the EDAMM device; A-power supply attachment, B- copper tape, C-top electrode, D-processing chamber, E-stainless steel base.

The powders used in this thesis were supplied by Sigma Aldrich, and their particle sizes and purities are listed in Table 2. The powders were weighted to the second

decimal place and mixed in stoichiometric ratios to a total weight of 0.2g. Most of the powders were kept under vacuum and did not need any further preparation preceding the synthesis, but the BaO powder was dried at 200°C for ~2 hours before each experiment because of its hydrophilic nature.

Unless stated otherwise, the EDAMM electrode was sand blasted with fine, 60 mesh Al_2O_3 particles and then polished with SiC paper.

TaC electrode coating: The surface of electrodes used in experiments with the $BaO - TiO_2$ powders were modified by mixing the Ta and C powders in stoichiometric ratios to 0.2 g and then processing them in EDAMM in Ar atmosphere for 15 minutes. After every 5 minutes of processing EDAMM was stopped and the processed powders were removed and replaced with newly mixed powders; this procedure was carried out three times. The electrode and the chamber were not cleaned after removing the processed power and replacing with newly mixed powders. After the electrode was coated the EDAMM chamber was cleaned with the abrasive paper to remove any loosely attached Ta and C or Ti and C particles, and the electrode was cleaned with a paper tower and ethanol. The chamber was allowed to cool for 1 hour in air before further experiments were carried out.

Table 2.1: TaC electrode coating preparation regime.

Total time (min)	**Pulse on/off ratio (%)**	**Pulse intensity (%)**	**Target current (A)** δ = ± 0.1 A	**Power input (A)** δ = ± 0.07 A	**Effective power (A)** δ = ± 0.02 A	**Vibrations (V)**
3 x 5 min	70	80	3.89	2.46	0.45	0.5

Table 2.2: Materials used in the following thesis.

Name	**Company**	**Ref. number**	**Powder purity**	**Particle size**
BaO	Sigma Aldrich	288497	97%	n/a
TiO_2	Sigma Aldrich	204757	99.99%	n/a
Cr	Johnson Matthey	n/a	99.95%	50 mesh
Ti	Pure Tech	n/a	99.99%	-60/+200 mesh
Mn	Sigma Aldrich	463728	99.99%	n/a
C	n/a	n/a	n/a	n/a
Si	Towson and Mercer	n/a	97/98%	n/a

2.2 Temperature measurement

Thermocouple measurements were taken to observe changes in the temperature of the chamber during plasma processing and as the pulse intensities changed. Figure 2.2 shows the how the thermocouple setups were arranged. In the first setup the surface of the thermocouple was in contact with the wall of the EDAMM base and was ~10cm from the processing chamber, while in the second arrangement a thin thermocouple needle was inserted into the cavity at the bottom of the EDAMM base and placed ~1mm below the surface of the processing chamber.

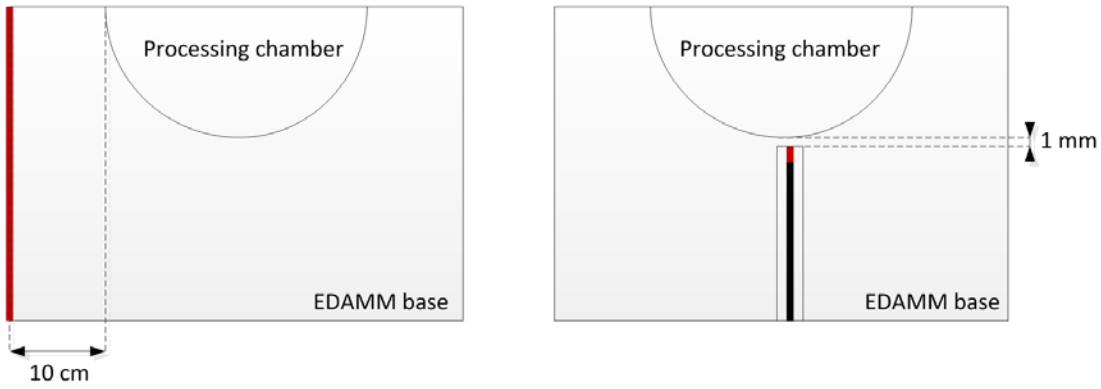

Figure 2.2: Position of the thermocouples for measuring the temperature of the EDAMM base after each experiment, a) external along the EDAMM base wall and, b) close to the processing chamber.

2.3 X-ray diffraction (XRD)

Powder particles obtained via EDAMM were characterised by X-ray diffraction to reveal the crystalline character of the constituent phases. This examination was done using an XRD Philips Diffractometer with Cu Kα radiation and a graphite monochromator. Diffractometer output was analysed using Traces Version 5.1.0 and an online version of Full Profile Search Match software with Crystallography Open

Database (COD) [29]. Phase identification was carried out using the International Centre for Diffraction Data (JCPDS-ICDD 2000) Powder Diffraction Files (PDF).

The powder samples prepared for the X-ray diffraction were mixed with a mortar and pestle and placed on a quartz disc. The powders are typically secured to the disc by mixing them in ethanol or acetone and then placing the mixture onto a quartz surface and allowing it to dry and form a smooth surface. In this instance, due to the hydrophilicity and sensitivity to alcohol of some powders, high vacuum, amorphous grease was used to secure the powders in situ.

2.4 Sample preparation for electron microscopy

The powders processed in EDAMM were pressed into 4.5 mm diameter pellets using a hand press with a 1MPa load. Note that the powders were not crushed in a mortar or pestle before being pressed to ensure the larger particles would be suitable for microstructural analysis. Moreover, no binder was used to stabilise the pellet in order to avoid contamination during the energy dispersive X-ray spectroscopy (EDS) analysis, so rather than automated mechanical polishing, the pellet was lacerated diagonally and its cross-sectional surface was hand polished with the #2000 SiC paper until smooth. The pellet was then mounted onto a copper sheet with silver paint such that its surface protruded from the copper sheet by ~2mm (Fig. 2.3). As-prepared sample was once again mounted onto an aluminium holder with silver paint that is compatible with the Leica EM-TIC020 ion milling stage. The surface of the pellet was then polished in a Leica EM-TIC020 by utilising three fixed ion beams to cut across the cross section and return a flat surface. This mill was operated at 6.5 kV, 3.5 mA for ~8 hours. After polishing, the pellet was then mounted onto the Leica EM-RES101 holder and then ion milled in the Leica EM-RES101 with the stage rotation set to ±60° and operating at 8 kV, 2.5 mA for up to 15 hours, depending on the thickness of the original pellet. The end result was highly polished flat, surfaces that were free of

defects and therefore suitable for imaging, energy dispersive X-ray spectroscopy (EDS), and electron back-scattering diffraction (EBSD) work.

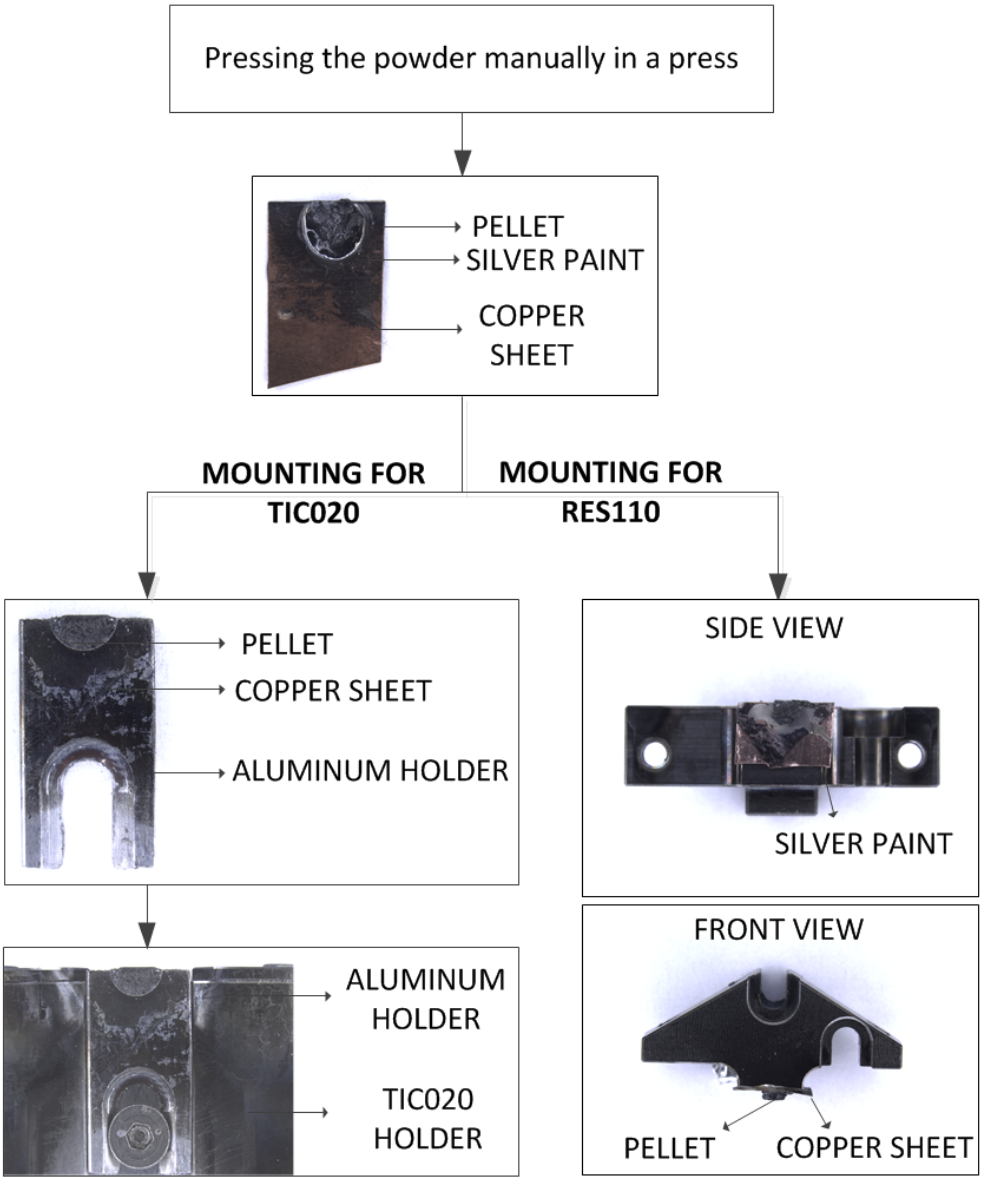

Figure 2.3: Sample preparation regime with the usage of TIC020 and RES101 ion milling devices.

2.5 Scanning electron microscopy/energy dispersive X-ray spectroscopy (SEM/EDS)

SEM/EDS was undertaken with a JEOL JSM-7001F microscope field emission gun-scanning electron microscope operating at 15 kV, ~6.5 nA probe current and at 12 mm imaging working distance and 10 mm working distance when used for EDS work. Elemental composition analysis was carried out using Energy Dispersive X-ray Spectroscopy (EDS) with Oxford Instruments X-max^N 80mm^2 detector system running in semi-quantitative standardless analysis mode and analysed using the Aztec software. Ba/Ti ratio in $BaTiO_3$ compound included in Chapter 5 was obtained by averaging at least 8 EDS points from areas that were chemically similar.

2.6 Electron back scattering diffraction (EBSD)

EBSD was undertaken on a JEOL JSM-7001F field emission gun-scanning electron microscope operating at 15 kV, ~6.5 nA probe current at 12 mm working distance and 4000× magnification, and which was fitted with an Oxford Instruments Nordlys-II(S) camera interfacing with the AZtec acquisition software suite. A step size of 0.035 μm was used such that a map consisting of 1024 x 768 pixels was collected over 15:5:38 hours that corresponded to an area of 40 x 30 μm.

At each pixel, the image of the electron back-scattered pattern was saved upon acquisition at an exposure time of ~18 ms using 4 × 4 binning and three background frames. Subsequent post-processing involved indexing up to 8 Kikuchi bands within each EBSP using 50 (monoclinic $Ba_2Ti_4O_{13}$), 44 (hexagonal $BaTiO_3$) and 50 (cubic $BaTiO_3$) reflectors at a constant Hough resolution of 60.

Post-processing of EBSD data

The EBSD maps were post-processed using an Oxford Instruments Channel-5 software suite. The maps were cleaned by removing the wild spikes, cyclic extrapolating the zero solutions to five neighbours and thresholding the band contrast to delineate unindexed regions. In this study, phases are superimposed onto the band contrast map such that red, green, blue and white denote monoclinic $Ba_2Ti_4O_{13}$, hexagonal $BaTiO_3$, cubic $BaTiO_3$ phases and unindexed regions, respectively. For all calculations, misorientations between 2°-15° and greater than 15° were classified as low (LABs, in yellow) and high (HABs, in black) -angle boundaries, respectively.

2.7 Focused Ion Beam sample preparation method

Focused ion beam (FIB) sample preparation was carried out with an FEI Helios NanoLab G3CX dual (electron and ion) beam analytical scanning electron microscope. The lamellas were lifted out with the automated EasyLift needle and then prepared to undertake transmission electron diffraction and transmission kikuchi diffraction t on the three phases present in the $BaO - TiO_2$powders after EDAMM processing.

The surface of the sample was first polished to a high quality flat surface suitable for high quality EBSD mapping and then the regions of interest were chosen. Grain boundaries that could be used to study cubic-hexagonal, cubic-monoclinic and hexagonal-monoclinic phases in $BaO - TiO_2$ EDAMM processed powders were located. Lamellas were cut perpendicular to the surface of the samples and then polished according to the method summarised in Table 3.

Table 2.3: Focused ion beam sample preparation conditions.

Process	Voltage (kV)	Current (nA)	Surface orientation†
Pt deposition (E-beam)	2	2.8	⊥ to E-beam
Pt deposition (I-Beam)	30	0.23	⊥ to I-beam
Trenching (multi-pass)	30	9.3, 2.5	⊥ to I-beam
Trench clean-up (single-pass)	30	2.5	⊥ to I-beam ± 1.5
Lamella undercut	30	0.8/2.5	⊥ to E-beam
Lamella to EasyLift weld	30	0.018	⊥ to E-beam
Cleaning Cu holder	30	21	⊥ to I-beam
Cutting trench in holder	30	21	⊥ to I-beam
Welding lamella to holder	30	0.023	═ to E-beam
	30	2.5	═ to I-beam ± 0.5
	30	0.79	═ to I-beam ± 0.7
Lamella polishing (single-pass)	30	0.43	═ to I-beam ± 0.7
	30	0.23	═ to I-beam ± 1.5
	5*	0.15	═ to I-beam ± 5.0

* - final polishing with 5kV was carried out to remove the amorphous layer typical when using high voltages[30].

†- Orientation following lift out is edge-on to the lamella.

2.8 Transmission Electron Microscopy (TEM)

Transmission electron microscopy was carried out on high resolution JEOL JEM-ARM200f operating at 200 kV with a resolution of <0.08 nm, equipped with cold field emission gun source, Gatan UltraScan 1000XP CCD camera (2k x 2k) and fitted with advanced Cs spherical aberration-corrector for the condenser lens. Additionally, JEOL

JEM2011 operating at 200 kV fitted with LaB6 transmission electron with a spatial resolution of 0.16 nm and Gatan Orius CCD camera was used for some diffraction experiments.

The samples presented in CHAPTER 5 were analysed with the JEOL JEM-ARM200f; this also included diffraction analysis and (EDS) mapping. The nanometre size powder particles were dispersed on the lacey carbon grid.

The images of interphase boundaries analysed in CHAPTER 6 were taken in bright-field mode and the samples were prepared by the FIB technique. TEM used in this part of the research was utilized to provide information about the crystallographic structure of the constituent phases and also to reveal the orientation relationship in between the phases in ceramic materials. For the cubic-hexagonal interphase boundary diffraction analysis, the diffraction patterns were then taken on $[111]_c$ and $[0001]_h$ cubic and hexagonal zone axis, respectively. In order to re-confirm the orientation relationship in cubic-monoclinic interphase boundary the beam was tilted to reach the [002]c zone axis which caused distortion (elipticity) in the diffraction pattern. This distortion was corrected using the "Ellipse Fitting Analysis" script from the [31]. Diffraction patterns were then taken at $(002)_c$ || $(0\bar{2}0)_m$. The diffraction analysis on the hexagonal-monoclinic interphase boundary was undertaken when tilted to $[\bar{2}21]_h$ || $[0\bar{1}0]_m$ zone axis of hexagonal and monoclinic phases, respectively.

CHAPTER 3

Polymorphic transformations in selected materials

3.1 Overview

In this chapter a series of powders were processed in EDAMM in order to:

I. To investigate the influence of plasma discharges on polymorphic transformations in selected materials,
II. Study the effect of coating electrode on polymorphic transformations,
III. Determine the plasma temperature in EDAMM.

In this study, we selected materials which show polymorphic transformations at different temperatures. The aim was to indirectly measure the plasma temperature in variety of plasma conditions and investigate their influence on polymorphic transformations. Therefore, the term *"plasma equivalent temperatures"* is presented in this chapter which means that specific EDAMM conditions caused changes in materials equivalent to those observed in equilibrium heating/cooling conditions or other information based on the literature. This kind of approach was used previously to estimate the temperature of the low energy milling conditions in planar-type ball mill for selected materials (TiB_2, Fe_3N and $Mg_{70}Zn_{30}$)[32].

It is important to know the plasma temperature as the higher temperatures are more beneficial for high melting point materials and transformations (e.g. ceramics), whereas lower ones can be targeted for low melting point materials and transformations, such as synthesis of metal hydrides. Detailed processing conditions are listed in the Table 3.1 below.

Table 3. 1 EDAMM processing conditions of materials presented in CHAPTER 3.

Sample name	Processing conditions					
	Gas type	Pulse on/off ratio (%)	Pulse intensity (%)	Time (min)	Electrode type	Power input
Mn	Ar	70	20-90*	5	SS** ball	DC
Al	Ar	70	20	5	SS** ball	DC
TiO_2	Ar	70	30-80*	5	SS** ball	DC
Ti-Cr	Ar	70	80	5	SS** ball	DC
BaO-TiO_2	Ar	70	80	5	SS** ball	DC
SiC	Ar	70	40-90*	5	SS** ball	DC

* indicates gradually increasing electrical conditions throughout the experiment ** SS-stainless steel

3.2 Results and discussion

3.2.1 EDAMM processing of Mn in Ar

Mn exists in the four crystal structures listed in Table 1, the lattice parameters of the unit cells given in the table are the newest available in the ICSD database. All the Mn crystal structures are cubic with variety of different symmetries (Table 3.2). The type of the crystal symmetry is dependent on the processing temperature and results in the lattice constant reduction with increased temperature. The crystal structure that is stable up to 710°C (or even 700°C [33]) is a body-centred cubic α-Mn, with the highest lattice constant of 8.911Å[34]. After being heated it transforms into a primitive cubic β-Mn with lower lattice parameter that is stable until it reaches 1086°C. This α→β transformation temperature will be used in the following section to determine the minimum equivalent temperature for plasma in low electrical conditions in EDAMM. Note that both forms of Mn are hard and brittle[35] which during EDAMM processing usually helps with efficient milling, crushing, and micro-sintering processes.

Table 3.3 Manganese crystal structures and their equilibrium temperature ranges.

Symbol	Crystal type	Space group	Lattice constant, a	Temp range
α	Cubic (body-centered, hextetrahedral)	I-43m	8.911 Å [36]	RT to 710°C
β	Cubic (primitive, gyroidal)	$P4_132$	6.315 Å [37]	710-1086°C
γ	Cubic (face-centered, hextetrahedral)	Fm-3m	3.863 Å [38]	1086-1137°C
δ	Cubic (body-centered, hexoctahedral)	Im-3m	3.081 Å [38]	1137-1244°C

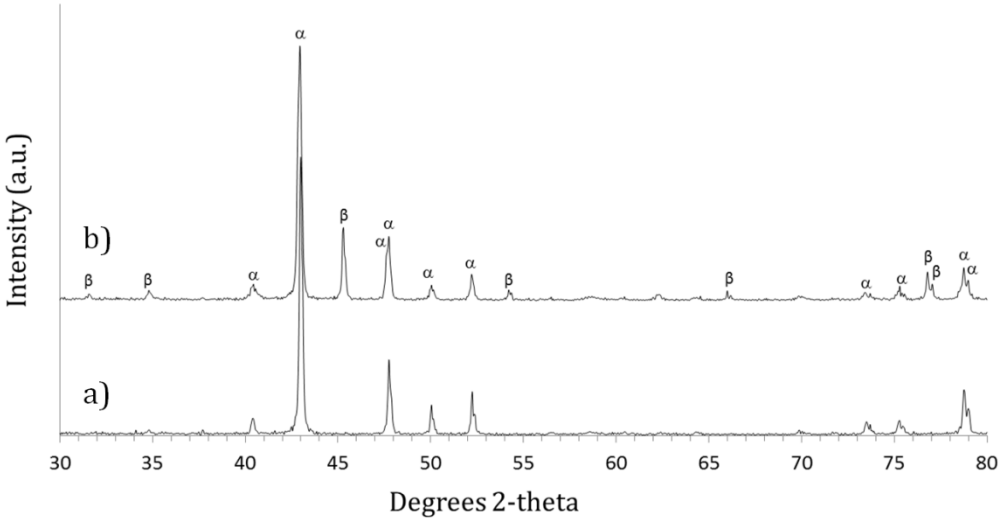

Figure 3.1: XRD of a) Mn starting powder and b) Mn processed in EDAMM in Ar with 20% pulse intensity.

In Figure 3.1 the X-ray diffraction of Mn processed in Ar is shown. It can be seen that the Mn starting powder consists of only α-Mn phases but processing of the powder in only 20% of maximum EDAMM pulse intensity results in the formation of a significant

amount of β-Mn. It is thought that the minimum plasma equivalent temperature in this case is 710°C.

Further investigation of the EDAMM chamber heating during the experiment as shown in Figure 3.2 indicates that the biggest increase occurred between 60-70% of maximum pulse intensity, where the temperatures were 26˚C and 34˚C, respectively.

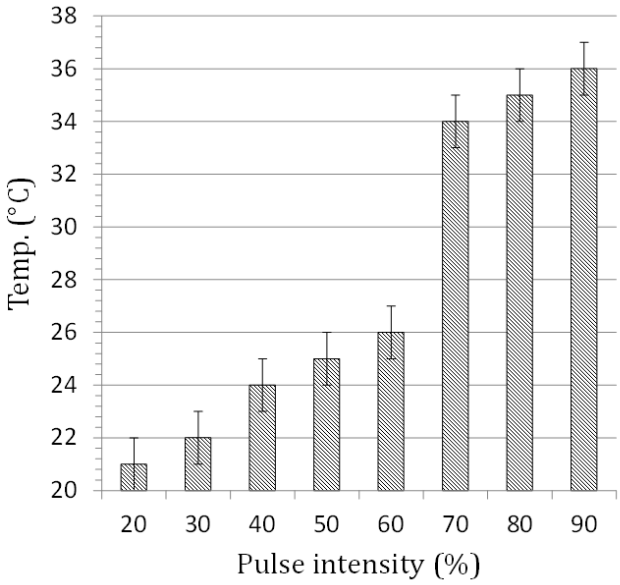

Figure 3.2: EDAMM chamber temperature change during Mn processing in Ar.

3.2.2 EDAMM processing of Al in Ar

To further confirm the minimum temperature obtained in EDAMM in low discharge energies, Al powder was processed in Ar at 20% of maximum power intensity. As expected, and as shown in Figure 3.3, Al powder melted even in such low electrical conditions. The figure shows rounded particles which are thought to have melted or even evaporated and instantly solidified during pulsed EDAMM processing. It is quite typical for low melting point metals to form large agglomerates of sintered particles.

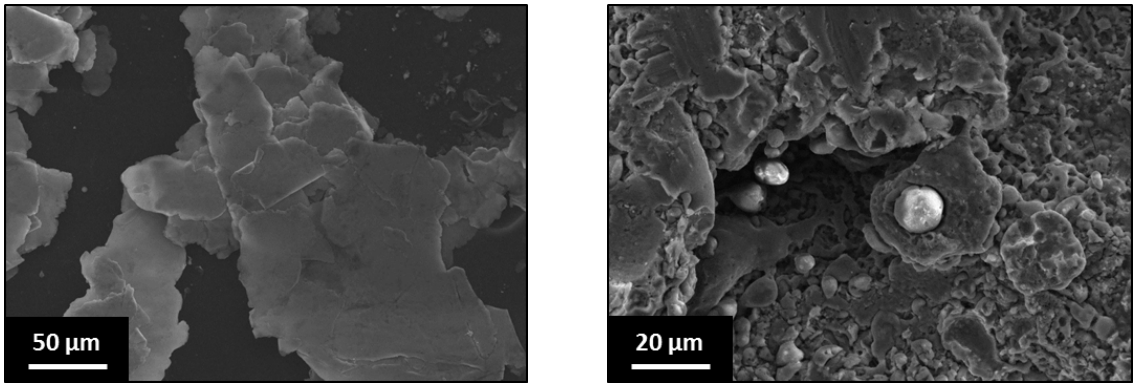

(a) (b)

Figure 3.3: Secondary electron images of (a) Al starting powder and (a) Al processed in EDAMM with 20% pulse intensity.

3.2.3 EDAMM processing of TiO_2 in Ar

TiO_2 is known to have many polymorphs, of which three are the most commonly studied, i.e., brookite, anatase, and rutile. Rutile is thought to be more stable than anatase at all pressures and temperatures [39]. It is widely accepted that the bulk transformation of anatase to rutile occurs at temperatures above 600°C, but depending on the processing method, the atmosphere type, particle size [40] and impurities or doping level [41, 42], this temperature may vary between 400 and 1200°C.

To determine the minimum plasma equivalent temperature, TiO_2 powder containing anatase and rutile was processed in EDAMM in Ar and the phase transformation was observed. It has been found that even low discharge energies (40% pulse intensity) resulted in complete anatase→rutile transformation (Fig. 3.4). Once again varied pulse intensities was used to observe the temperature change of the chamber (Fig. 3.5) which showed the largest increase in 50-70% of maximum pulse intensity. The result is similar to the one obtained for the Mn powder which confirms that the

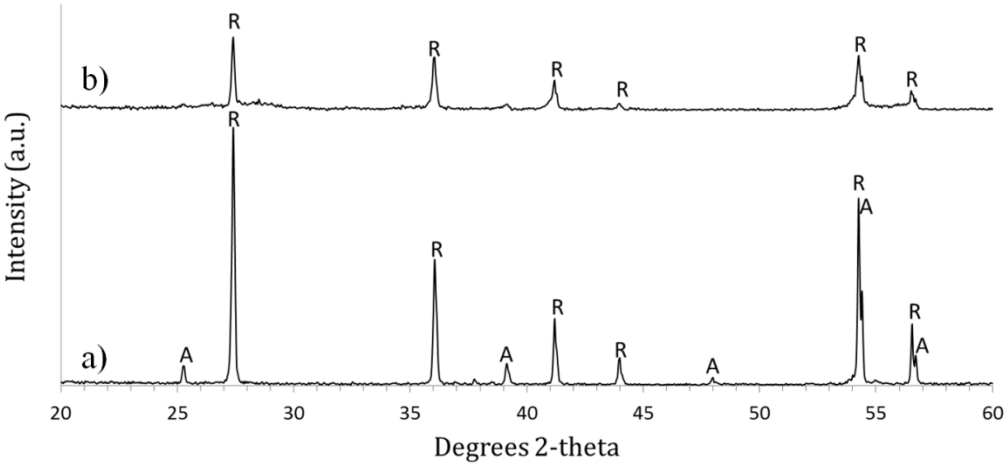

Figure 3.4: XRD of a) TiO_2 starting powder and b) TiO_2 processed in EDAMM in Ar with 40% pulse intensity.

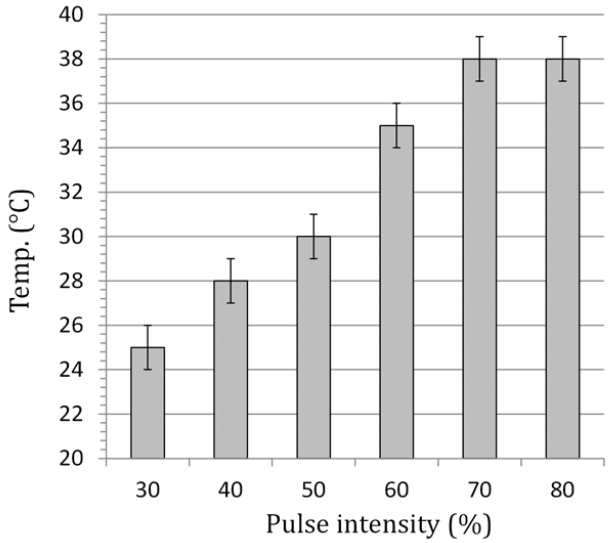

Figure 3.5: Temperature change of EDAMM chamber when processing TiO_2 in Ar.

3.2.4 EDAMM processing of Ti-Cr in Ar

$TiCr_2$ belongs to the class of compounds called Laves phases and can exist in three polytypes;

1. Low temperature $MgCu_2$-type cubic (C_{15}),
2. $MgNi_2$-type hexagonal (C_{36})
3. High temperature $MgZn_2$-type hexagonal (C_{14})[43, 44].

C_{36} phase was reported to be metastable and it was suggested that it only exists with Cr excess and after quenching [45]. More commonly, high temperature C_{14} phase transforms directly to C_{15} phase upon cooling.

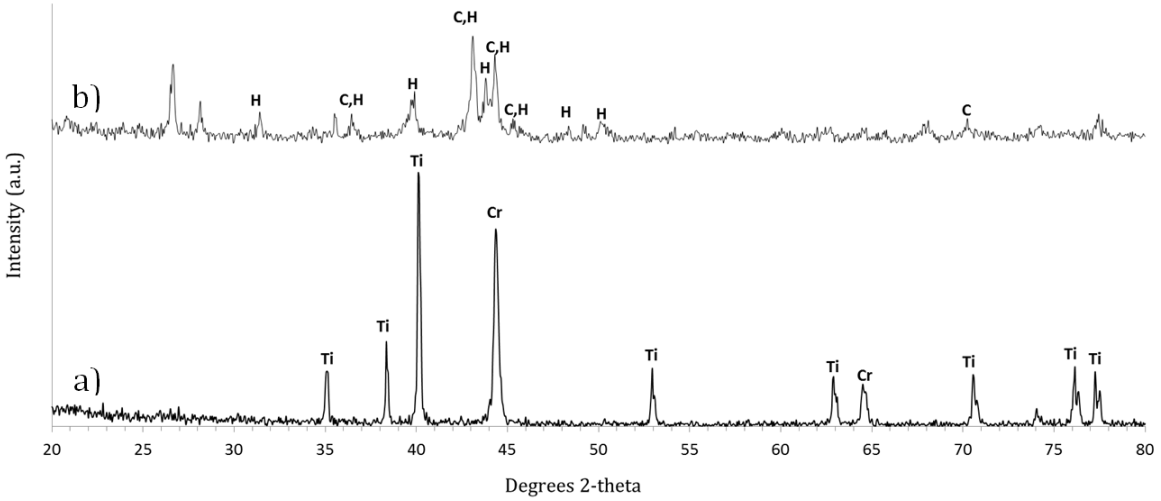

Figure 3.6: XRD of a) Ti and Cr starting powders and b) $TiCr_2$ processed in EDAMM with 80% pulse intensity. Legend: C- cubic $TiCr_2$ (C_{15}), H-hexagonal $TiCr_2$ (C_{14}), C,H-peaks common for both phases.

Starting powders consisting of Ti and Cr metals mixed in stoichiometric ratios (65wt%Cr) were processed in EDAMM in Ar gas and 80% pulse intensity for 5 min (Fig. 3.6). Based on the phase diagram [46], high temperature C_{14} phase exists up till 1370˚C, above which it forms β-TiCr solid solution. No peaks of β-TiCr phases were found on the X-ray diffraction pattern what indicates that the temperature of the

processing didn't exceed 1370˚C. Some peaks could not be identified but they do not correspond to the β-TiCr phase. On the other hand, peaks corresponding to the cubic C_{15} phase were found on the XRD pattern what indicates that some portion of the processed material was affected to a lesser extent by the highly localized, high temperature discharges passing through the particles. This temperature gradient within the particles during the plasma discharge processing results in presence of both low and high temperature $TiCr_2$ phases.

3.2.5 EDAMM processing of BaO-TiO_2 in Ar

$BaTiO_3$ ceramic powders can be obtained from mixing BaO and TiO_2 in stoichiometric ratios. Based on the phase diagram (Fig. 3.7) [47], low temperature cubic $BaTiO_3$ phase undergoes polymorphic transformation at 1430˚C above which it forms hexagonal crystal structure. Slight non-stoichiometry in the processed powders may lead to the presence of secondary phases. If TiO_2 excess is present those phases are typically $BaTi_2O_5$ and $Ba_6Ti_{17}O_{40}$, whereas excess of BaO may result in formation of $Ba_{1.054}Ti_{0.964}O_{2.964}$ and Ba_2TiO_4. Moreover, even small TiO_2 excess (1-2mol%) may result in the shift of the cubic→hexagonal transformation temperature from 1430°C to even 1539°C.

BaO and TiO_2 mixed in stoichiometric ratios were processed in EDAMM in Ar and 80% pulse intensity for 5 min (Fig. 3.7). XRD result shows that the starting powder was fully transformed into a mixture of hexagonal and cubic $BaTiO_3$. The same result, although not shown here, was obtained when powders were processed with 90% pulse intensity. Due to the fact that both cubic and hexagonal phases were observed, the average processing temperature can be estimated as ~1430°C. Similarly to the $TiCr_2$ phases analysed beforehand, the presence of both low and high temperature phases indicates that the highly localized, high temperature discharge results in the temperature gradient within the particles.

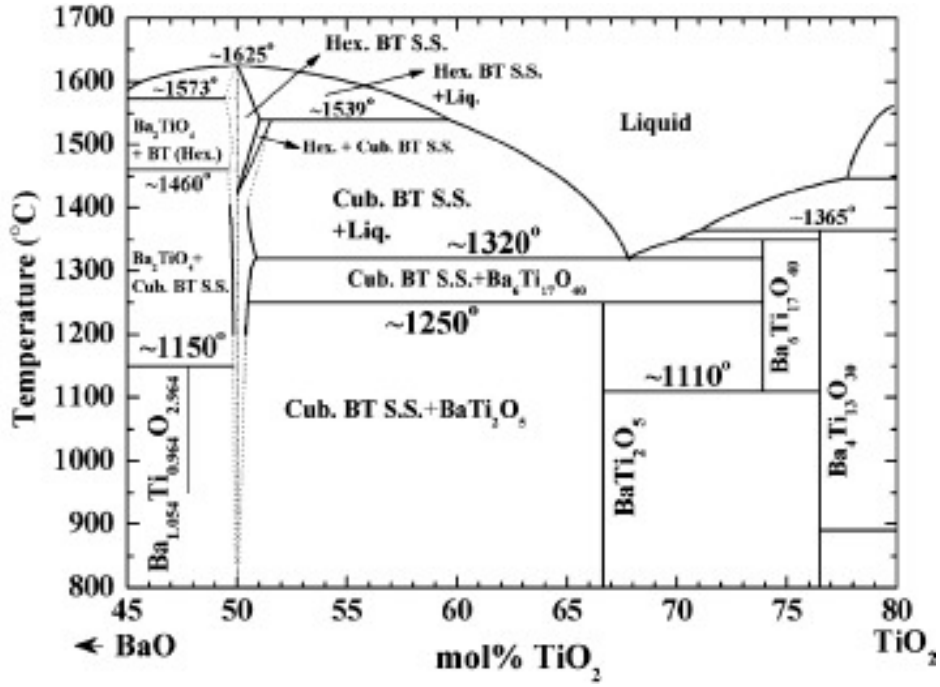

(a)

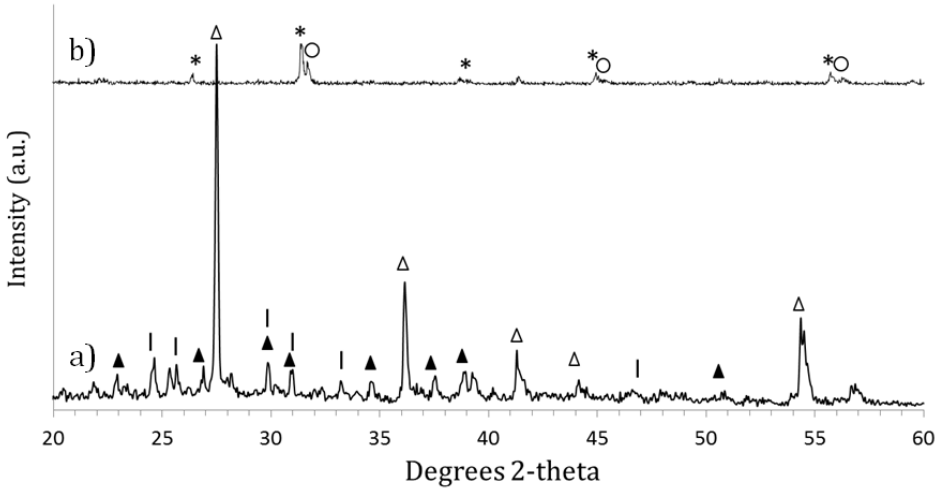

(b)

Figure 3.7: (Top): BaO-TiO_2 phase diagram [48] and (Bottom): a) XRD of BaO-TiO_2 starting powders and b) XRD of $BaTiO_3$ synthetised in EDAMM in Ar with pulse intensity of 80% from BaO and TiO_2. Legend; Δ- TiO_2 rutile, ┣ BaO, ▲- $BaO_{1-x,}$ ○ - cubic $BaTiO_3$ and *- hexagonal $BaTiO_3$.

3.2.6 EDAMM processing of SiC in Ar

SiC is a ceramic material that experiences polymorphism of a large number of polytypes which differ in their stacking sequence;

I. 3C-SiC (β)
II. 4H- SiC
III. 6H-SiC (α)

Their formation can be altered by the processing temperature and atmosphere[49]. Low temperature SiC exists as a cubic crystal structure that preferably crystallises around 1200°C, whereas the high temperature version of hexagonal β-SiC can be preferably be obtained between 1500-2200°C [38]. Fully hexagonal α-SiC can, however, be obtained at 1600°C [50].

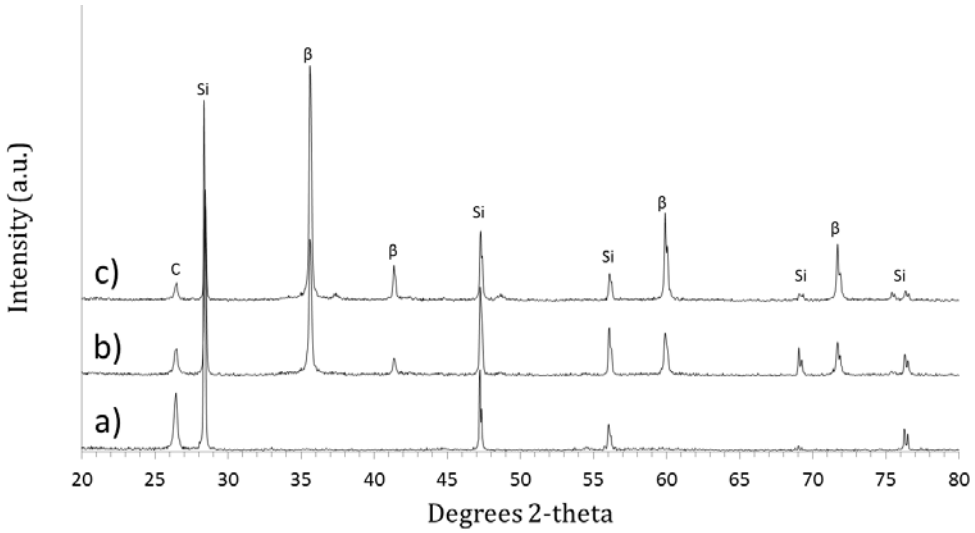

Figure 3.8: (a) Si+C starting powder and SiC synthesis in EDAMM in Ar from elemental Si and graphite (C), at (b)40% and (c)90% pulse intensity.

Figure 3.8 shows the XRD of Si+C powders processed in Ar with 40 and 90% pulse intensities. It can be seen that not all the Si+C starting powder was transformed into β-SiC because some of the peaks of the starting powders can be still identified even after processing at the highest electrical conditions. The β-SiC identified in the XRD

pattern is typically stable below 1600°C, and therefore the maximum temperature obtained in the process was lower.

Analysis of the change in the temperature of the chamber during the SiC processing experiment (Fig. 3.9) reveals that the largest increase occurred between 50-60% of maximum pulse intensity, which is similar to the results obtained for the other materials. The final temperature obtained through processing was the highest yet recorded.

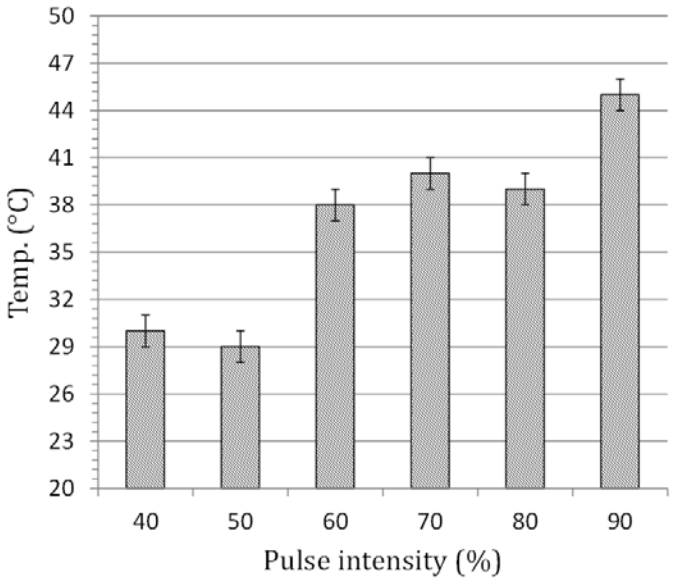

Figure 3.9: Change in temperature of EDAMM chamber while processing SiC in Ar.

The publication prepared by our research group showed that the transformation of β→α-SiC was not possible in Ar atmosphere and can only be achieved when using N_2 gas [49]. The reason for that is that the N_2 gas molecules are di-atomic and therefore undergo dissociation and then ionization which increases their energy level. This energy is then utilized to increase the efficiency of the plasma processing by increasing the processing temperature.

3.3 Altering of the EDAMM processing temperature through atmosphere and electrode coating

Apart from the pulse on/off ratio and pulse intensity of the power supply used in EDAMM by selecting gas and electrode material we can additionally control the processing temperature. Monoatomic gases such as Ar and He contain relatively low amounts of energy at low temperatures, but as the temperature increases the atoms become more mobile and there is the likelihood of inelastic scattering, so the energy content in each mole of gas increases. In monoatomic gases this increase in energy is quite small over a wide temperature range, so to make EDAMM processing more efficient, diatomic gases such as N_2, H_2 or even O_2 can be used because even low temperatures cause the diatomic molecules to dissociate and become ionized [51]. Moreover, their energy content is much higher than monoatomic gases.

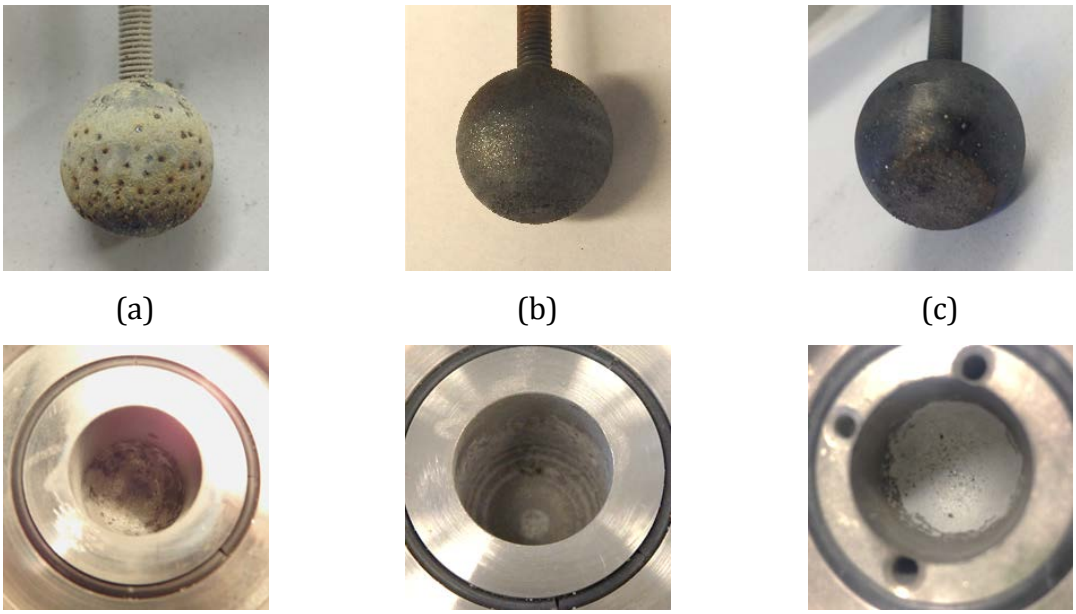

(a) (b) (c)

(d) (e) (f)

Figure 3.10: EDAMM ball electrodes and surface of the chamber after (a, d) processing in Ar, (b, e) processing in O_2/Ar and (c, f) processing in Ar with a TaC coating applied onto the electrode.

In the following experiment, the results of processing in three conditions are compared; Ar, 10%O_2/Ar and Ar with the TaC coated electrode. Firstly, Figure 3.11a and d show that processing in Ar results in a range of highly concentrated discharges that were visible on the electrode and the surface of the processing chamber. This distribution of discharges, although highly effective in the path of the discharge, may result in incomplete processing of the powder in the chamber.

It was found that when the mixture of 10%O_2/Ar was used, processing on both surfaces was much more uniform (Fig. 11b and e), so rather than highly localised discharge spots, the concentrically distributed areas are visible. Note that the surfaces on the electrode and the chamber oxidized under these conditions and most likely contain a wide variety of iron oxides. An oxide layer may form in the first few seconds of processing, which results in a more uniform distribution of discharges later in the process. By measuring the surface temperature using thermocouple, as it is presented in the earlier parts of this chapter, the highest increase in temperature occurred between 20-40% of the maximum pulse intensity (Fig. 3.12), which is much lower than 50-70% found previously for Ar gas. Although the surface measurement only indicates the processes occurring in EDAMM, rather than giving some specific values, this result shows that much lower temperatures are needed to transfer heat efficiently in this plasma environment.

The last type of processing condition selected to potentially lower the plasma temperature was applying a TaC coating on the EDAMM ball electrode. The coating was prepared by mixing Ta and graphite powders in stoichiometric ratios and processing them in EDAMM in Ar for 15 min. After each 5 and 10 min of processing the processed powder was retrieved from the chamber and substituted with a fresh one. As can be seen in Fig. 3.11 c and f, the discharge area visible on the surface of the chamber is much more uniform than in the case of bare stainless steel ball electrode processed either in Ar or 10%O_2/Ar. It leads to the conclusion that the discharges must have been much more evenly distributed across the chamber during the processing. Additionally, it was noticed during the processing that the ball electrode's

movement in the chamber was much more regular than in the previous cases. The ball didn't seem to weld itself to the surface of the chamber either, whereas during the experiments in Ar and 10%O_2/Ar the electrode had to be sometimes detached manually to proceed with the experiment.

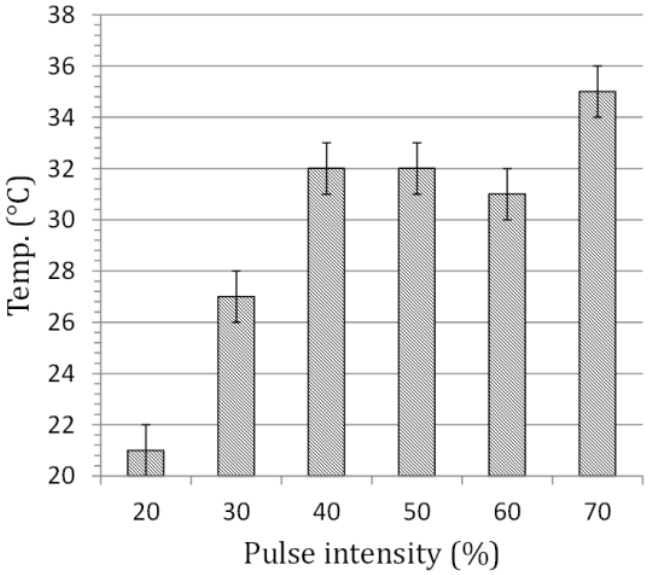

Figure 3.11: Change of temperature of EDAMM chamber when processing in 10%O_2/Ar with 70% pulse module and varied pulse intensity.

We believe that TaC effect is the opposite to adding O_2 to Ar gas, which means the TaC coating may be slowing down the electrons in the EDAMM chamber by providing non-homogeneous distribution of TaC on its surface. TaC and other metal carbides are already used to coat stainless steel to improve its hardness and wear resistance. Interestingly, Ta was also found to form TaC with the carbon diffusing from the stainless steel [52] at intermediate temperatures between 1115-1155°C in a combination of casting and heat treatment. This fact may work in favour of the efficiency of coating in EDAMM. Here, however the process could be better compared with TaC powder plasma spraying method, such as in [53], where the TaC coating retained a porosity of around 14% on average.

In order to look at the effects of the three abovementioned conditions more closely, we introduced a thermocouple underneath the processing chamber, in ~1mm distance from the bottom surface (details in the method section). The values were recorded right after the processing was finished, to observe the temperature change when the chamber was cooling down. In the Figure 3.13 the cooling lines are shown. The top, broken line shows the cooling rate of the 10%O_2/Ar condition. It is clear, that the chamber temperature was the highest right after the processing, decreased quickly in the first few seconds and then was cooling down slower. It is an important indication that the overall heating of the chamber was in a high range and is consistent with the relatively large area of the chamber being affected and shown in Fig. 3.11b and e. Oxidation of the chamber surface which is an exothermic process may be one of the reasons for this elevated temperature to be observed. The second, dotted line in the Figure 3.13 is a representation of the chamber cooling after Ar gas processing condition. Here, a much larger drop in the temperature is observed straight after the processing but it plateaus below 50˚C. Again, this result is consistent with the previous observations of the discharge spots visible in Fig. 3.11a and d which suggests that the discharges affected some localized areas of the chamber surface rather than being evenly distributed. The continuous line in the Figure 3.13 corresponds to the EDAMM processing with the TaC coating on the electrode. Interestingly, the temperature right after the processing was near 50˚C and did not drop significantly over time. In accordance with the previously observed large discharge affected area the we suspect that the TaC coating caused much more even discharge distribution across the processing area and therefore decrease in the overall plasma temperature.

The above presented observations indicate that the TaC coating and selection of a different gases composition can contribute to EDAMM discharge temperature control which can be utilized in processing of large number of materials. In the following CHAPTER 5 and CHAPTER 6 this fact is further used to optimize the $BaTiO_3$ processing towards different polymorphs.

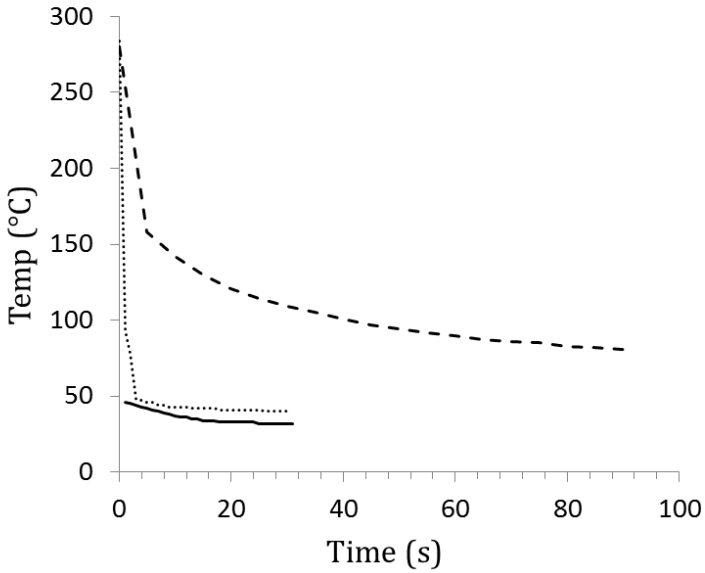

Figure 3.12: Change in temperature of EDAMM chamber while processing in a mixture of 10%O_2/Ar (broken line), Ar (dotted line) and in Ar with TaC coated electrode (solid line).

3.4 Conclusions

From the experiments presented in this section we can conclude that the temperature of the EDAMM chamber increases significantly over specific ranges of pulse intensity (Fig. 3.10). For Mn and TiO_2, the largest increase in temperature was recorded between 50-60% pulse intensities whereas SiC experienced a significant increase between 60-70%. It is thought that this increase of the temperature of the chamber is connected with the fact that the intensity of the discharge is large enough to be self-sustaining, despite the distance between the electrode and the bottom of the chamber. This result implies that the discharge supplied by the pulse power can exist continuously throughout processing and also explains why conductive metals processed under high pulse intensities would very often form large, micro-sintered particles whereas brittle ceramic powders would remain as fine particles.

EDAMM uses a power supply which creates discharges that are pulsed in order to prevent the materials from melting. For metals with relatively low melting temperatures, such as Al, it is impossible to prevent them from melting even in the lowest pulse intensities. This result defined the minimum equivalent processing temperature obtained at 20% pulse intensity, which was assessed to be 600°C. Processing of the materials experiencing a polymorphic transformation on the other hand, namely $TiCr_2$ and $BaTiO_3$, was employed in order to gain more information about the intermediate temperatures attained during EDAMM processing. It was found that both materials undergo an incomplete transformation at 80% of pulse intensity which is equivalent to less than 1370°C for $TiCr_2$ and an average of 1430°C, for $BaTiO_3$. This incomplete transformation is an indication that although at a given pulse intensity the processing temperature is high, the temperature gradient due to the localized discharges is too large to transform the whole material to the high temperature stable polymorph.

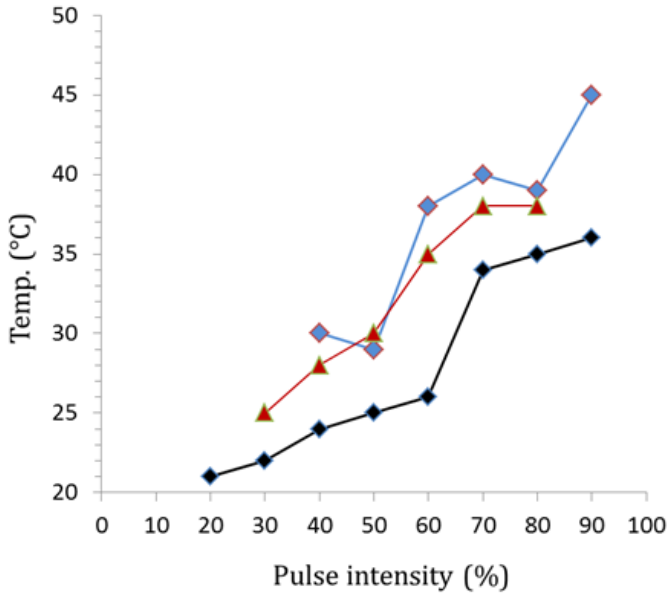

Figure 3.13: Comparison of the EDAMM chamber temperature with various pulse intensities for Mn (black), TiO_2 (red) and SiC (blue).

The maximum equivalent temperature in Ar processed at 90% pulse intensity was established through experiments performed on SiC powder and defined as lower than 1600°C, at which it would transform to higher temperature polymorph.

Further experiments involving modifications of processing conditions by (i) applying TaC on the stainless steel ball electrode and (ii) introducing 10%O_2/Ar gas instead of Ar, were performed. It was found that the overall temperature of processing was lowered in the instance of the TaC coating whereas changing from Ar to O_2/Ar gas mixture resulted in its increase. Additionally, the surface of the EDAMM chamber affected by the discharges was more uniform for both of these modifications in comparison to the processing with pure Ar gas.

CHAPTER 4

$BaO - TiO_2$ system phase transformations induced by pulsed plasma processing in EDAMM

In this chapter the optimization of EDAMM parameters to synthesize the specific crystal structure of $BaTiO_3$ from BaO and TiO_2 starting powders is investigated. The variables in this processing procedure are (1) the processing atmosphere, (2) the TaC coating on the stainless steel electrode and (3) the discharge energy of each process. The results are then validated and supported by supplementary experiments with Ta and C doping in an Ar atmosphere.

The resultant crystal structures were analysed by X-ray diffraction and the microstructure of the grains was via secondary electron microscopy (SEM). The chemical composition and elemental distribution analysis was derived from statistical information obtained through energy dispersive spectroscopy (EDS) point analysis and mapping.

This investigation was an advanced study into the change of crystallographic structures obtained under several different EDAMM conditions, and is therefore an extension of previous studies into complex $MgAl_2O_4$ and $CaCu_3Ti_4O_{12}$ and $BaLa_2Ti_4O_{12}$ oxides[25].

4.1 Introduction

Barium Titanate ($BaTiO_3$) is a ceramic material that is widely used in the electronics industry as a semi-conductor, thermistor, piezoelectric transducer and capacitor with high dielectric constant. Its properties and final application depend on Ba/Ti stoichiometry [54-56], the crystal structure [57], grain size and type [58, 59], the amount of dopants [60-63] or even the presence of a liquid phase in the early stages of processing [64] or intergranular phases[65].

$BaTiO_3$ powders can be synthetised by variety of different methods such as solid state or chemical methods. The solid state synthesis is typically performed using the ball milling method with BaO or $BaCO_3$ and TiO_2 starting powders [66, 67]. High energy ball milling proved to be an attractive tool for processing of this ceramic as the

mechanically activated powders exhibit much higher sinterability [68]. It was concluded that the activation of the powder has a large influence on the density of the final product and therefore on the dielectric properties. Other processing methods include hydrothermal processing which is highly sensitive to the precursor type. It was shown that the temperature of the process can be lowered to 250˚C and result in a tetragonal type of $BaTiO_3$ when the crystallites are larger than 1 μm [69, 70]. Below this crystallite size, the crystal structure of $BaTiO_3$ was observed as cubic. Sol-gel methods, typically relying on organometallic precursors, also proved to be a good way of nano powders preparation, where the temperature of the process was shown to be as low as 700˚C and results in pure cubic $BaTiO_3$ [71]. Sintering of the powders above 1200˚C resulted in significant grain coarsening for up to 20 μm and was even more pronounced at higher temperatures.

For many years, research concentrated on determining how the grain size influenced the materials' properties because a growth in grain above 1.2 μm generally reduces the dielectric constant and piezoelectric coefficient [72], and it is optimal between 0.99 and 1.2μm [73]. From a fundamental research perspective, the crystal structure determines the electronic properties of $BaTiO_3$, so one of the main challenges is to control the synthesizing process to allow for the production of a specific polymorph.

4.1.1 Crystal structures of $BaTiO_3$

$BaTiO_3$ exists as either rhombohedral (<-90°C), orthorhombic (-90-5°C), tetragonal (5-120°C) cubic (120-1430°C), and hexagonal (>1430°C) (Fig. 4.1a) crystal structures. Impurities and/or dopants can hugely influence the stabilization of the specific type of crystal structure. Elements such as Mn, Fe, Cr, Co, Cu, Ru, Rh are said to favour the formation of a hexagonal polymorph at lower temperatures [74, 75]. Si^{4+} ion and most isovalent substitutions on the other hand suppress the formation of hexagonal polymorph and large rare earths are reported to have a similar effect [76]. Since Fe is one of the most common impurities, it has been a subject of research where various

amounts of Fe_2O_3 powder were added to the BaO and TiO_2 starting powders [77]. They found that even small additions of 4at% can reduce the temperature of cubic ↔ hexagonal transformation from 1430°C to 1300°C. For many years the hexagonal form was perceived as an undesirable phase that is usually formed by over-firing above 1430°C, but recent studies have shown that the $BaTiO_3$ hexagonal phase can have unique properties such as giant permittivity [78]. The equilibrium diagram (Fig. 1b) shows that 50/50 mole% of BaO/TiO_2 results in the formation of pure $BaTiO_3$. Any deviation from that value gives secondary phases in the form of $Ba_6Ti_{17}O_{40}$ if an excess of TiO_2 is added, or Ba_2TiO_4 when an excess of BaO is present. At temperatures above 1350°C a liquid phase appears which may be a leading factor in determining what mechanism of formation takes place.

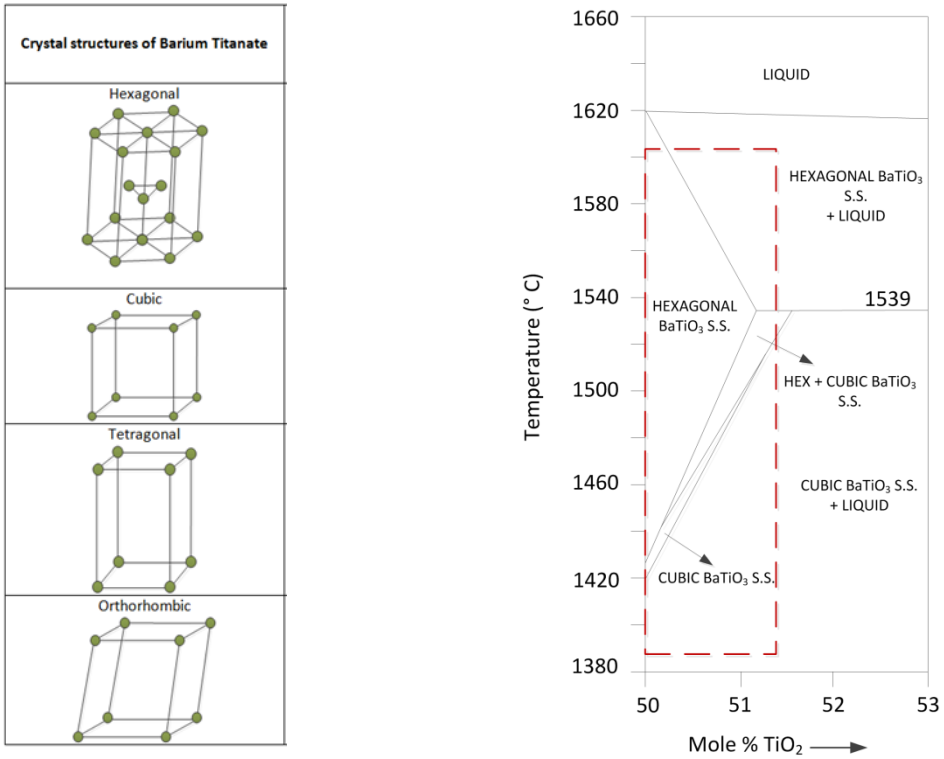

(a) (b)

Figure 4.1: (a) Simplistic representation of the crystal structures of $BaTiO_3$ and (b) fraction of the phase diagram of near stoichiometric $BaO\text{-}TiO_2$ (based on [48]).

Transformations of the various crystallographic forms of $BaTiO_3$ are diffusion-less processes based on a slight rearrangement of the atoms in the unit cell. These kinds of second order "displacive" transformations, which can be temperature and/or shear induced, may be regarded as martensitic and are mostly treated as such in literature [79]. The main aim of the research presented in this chapter study and determination of the equivalent temperature of the cubic→hexagonal $BaTiO_3$ transformation. Figure 4.2a and b, shows the basic unit cells of those two crystal types. The ideal cubic crystal structure of $BaTiO_3$ is typically called an ideal perovskite structure; whereas its transformation to hexagonal type results in the atoms misarrangement resulting in oxygen deficiency. This transformation temperature can be influenced by the type of processing, atmosphere, or the type and level of dopants or impurities as shown in the next sections.

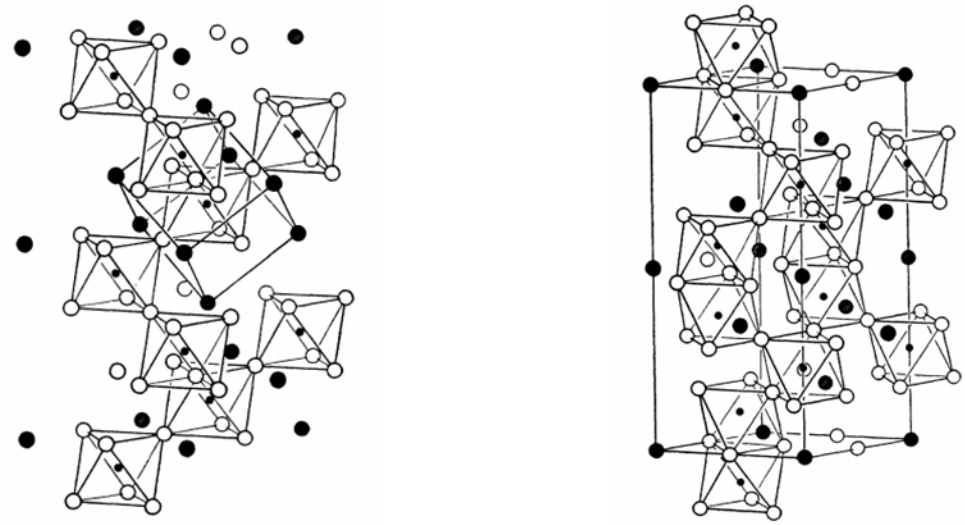

(a) (b)

Figure 4.2: Basic unit cells of (a) cubic and (b) hexagonal $BaTiO_3$ with visible oxygen octahedra, where • - Ti, ● - Ba and ○ - O atoms [80].

4.1.2 Fe contamination

The contamination of Fe during preparation can lead to formation of a variety of different secondary phases such as $Ba_4Ti_{10}Fe_2O_{27}$, $Ba_6Ti_7Fe_4O_{27}$, $Ba_4Ti_3Fe_4O_{16}$ or isostructural to $Ba_6Ti_{17}O_{40}$ - $Ba_4Ti_{10}Fe_2O_{27}$ and $Ba_2Ti_4Fe_2O_{13}$ and can affect the dielectric constant of the material, as summarised in [63]. The latter three cannot be distinguished by kikuchi diffraction because the lattice parameters of their monoclinic crystals are similar, therefore an EDS and TEM analysis was done on the samples to determine the level of Fe contamination and derive conclusions from the electron diffraction data. The influence of Fe on the dielectric properties of $BaTiO_3$ has already been studied by several researchers. For concentrations up to 4at%, Fe is said to slightly increase the dielectric constant of $BaTiO_3$ at room temperature, whereas shifting the Curie temperature to lower values, and even at 2 at%, reduces the formation of hexagonal polymorphs [81, 82]. Above 4at% Fe, the dielectric constant decreased when the Fe had completely dissolved into the $BaTiO_3$ lattice. Fe contamination and its influence on phase formation was included in the analysis because the use of stainless steel for the electrode and base material of EDAMM makes its appearance and, to a lesser extent, the appearance of Ni and Cr in the processed powders is highly probable.

4.1.3 Al contamination

Al is a second and often unavoidable impurity in the preparation process. It can form $Ba_4Ti_{10}Al_2O_{27}$ secondary phases which are also isostructural to $Ba_6Ti_{17}O_{40}$. When formed in the matrix in an irregular shape it does not show the orientation relationship with tetragonal $BaTiO_3$ but when it has grown on its {111} habit plane it shows up clearly, possibly assisting the formation of abnormal grain formation [58].

4.1.4 Ta-doping influence

The results in the later part of this chapter will show that Ta is another element which can influence the formation of a particular type of phase. Research into Ta doped tetragonal $BaTiO_3$ shows that it can substitute the Ti^{4+} in the crystal lattice and lead to a slightly higher dielectric constant; apparently it can also suppress the formation of abnormal grain growth and in small amounts promotes densification [62, 83]. In some cases Ta doping is realised by the addition of Ta_2O_5, where small amounts of a dopant in the ferroelectric tetragonal type of $BaTiO_3$ reduces resistivity in low doping level contents by up to 0.3mol%[84]. Moreover the microwave dielectric properties are enhanced for a single phase $Ba_{10}Ta_{7.5}Ti_{0.6}O_{30}$ where the precursor was Ta_2O_5 and the samples were ball milled and calcined at 1000°C [85].

A coating of TaC on the stainless steel electrode can potentially reduce the uptake of Fe to the processed powders and reduce the temperature of the plasma in EDAMM, but it can potentially lead to the intake of Ta or TaC to the processed powders as well. The degree of contamination from these elements and compounds was assessed with EDS and TEM analysis.

4.1.5 Influence of the processing atmosphere

That the atmosphere significantly influences the type of $BaTiO_3$ obtained during processing has been proven by many studies which involved air and H_2/Ar reducing atmospheres. For example, a pure H_2 reducing atmosphere during final sintering is thought to reduce the cubic-hexagonal transformation temperature from 1430 to 1330°C[86]. It was also observed that $Ba_6Ti_{17}O_{40}$ improves this transformation and is thought to form a eutectic liquid with $BaTiO_3$ at 1320°C. A statement was made that this melt could possibly encourage a discontinuous grain growth which would result in a coarse microstructure.

During traditional heat treatment methods in a H_2/N_2reducing atmosphere and temperatures above 1300°C, the only phases formed on the basis of the $BaO\text{-}TiO_2$-

Ti_2O_3 phase diagram were Ba_2TiO_4, $BaTiO_{3-\delta}$, $Ba_2Ti_6O_{13}$ and hollandite phases[47]. Reducing atmospheres during synthesis or sintering reduced the Ti^{4+} to Ti^{3+}, introducing oxygen vacancies. Attempts were made to restore the oxygen stoichiometry in the material, such as in [55], where annealing in air was done at 850°C after preparing the sample using the SPS method. In this case the results showed that the best dielectric properties were obtained when the samples were quenched in air after short annealing times. Seemingly, low partial pressures of oxygen during processing are better for hexagonal phase formation than ambient conditions. Moreover, experiments carried out in [87] indicated that the tetragonal $BaTiO_3$ obtained through the thermal decomposition of $BaTiO(C_2O_4) \cdot 4H_2O$ and reduction in H_2 caused its oxygen deficiency, but further heat treatment in an O_2 atmosphere at 1375°C returns the tetragonal/cubic modification. This effect was only partially observed at 1320°C.

4.2 Characterisation of starting powders and $BaO - TiO_2$ processing conditions

BaO belongs to a group of oxides with a hydrophilic nature and easily forming $Ba(OH)_2*H_2O$, as can be seen on the XRD pattern of the starting powder (Fig. 4.3a). Apart from stoichiometric BaO, the powder also contains a small amount of BaO_{1-x} (PDF 47-1488). TiO_2 powder however, consists of both rutile and anatase polymorphs.

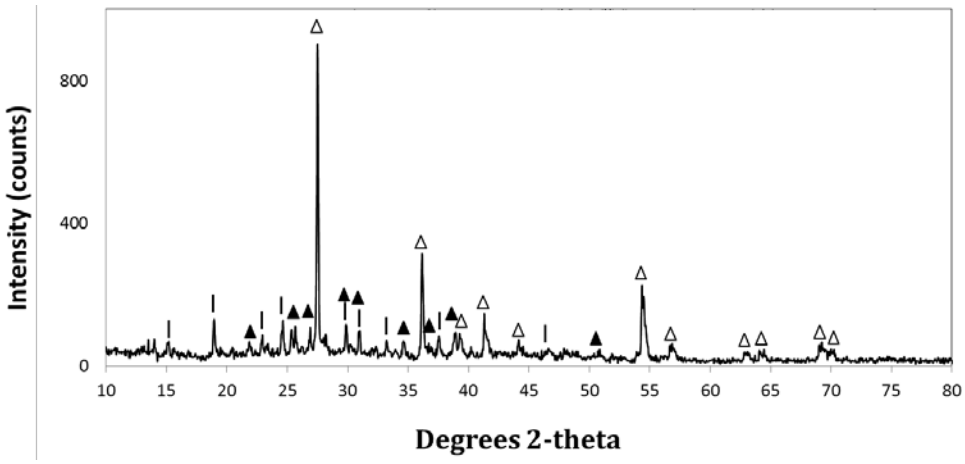

(a)

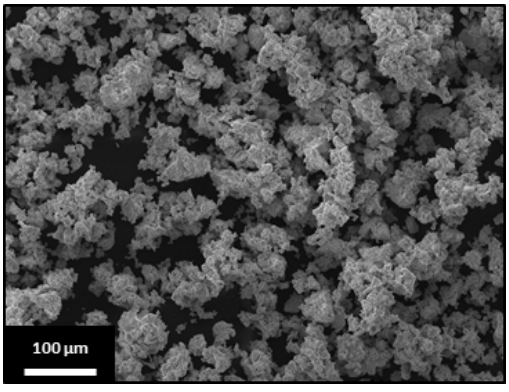

(b)

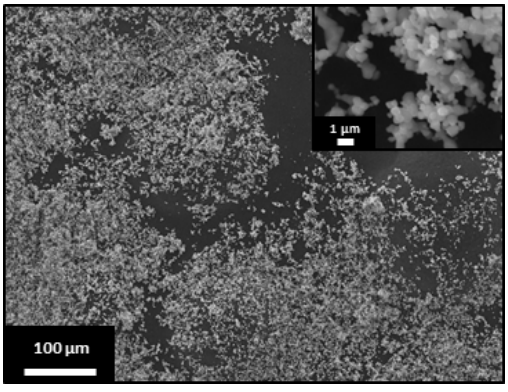

(c)

Figure 4.3: (a) X-ray diffraction of the $BaO - TiO_2$ starting powders and SEM images of morphology of b) BaO and (c)TiO_2 starting powders. Legend: Δ - TiO_2 rutile, **|** - BaO, ▲ - BaO_{1-x}

The morphology of the starting powders is shown in Fig. 4.3b and c. BaO particles tend to aggregate together due to their hygroscopic nature, although the sizes of individual BaO and rutile particles are actually similar.

$BaO - TiO_2$ starting powders were processed in EDAMM in a variety of conditions where the variables included: time, type of gas, electrical conditions, the pulse on/off ratio and pulse intensity, the type of electrode, the presence of a coating on the electrode (Table 4.1). An extensive investigation into the effects of the synthesis in these conditions is presented in this chapter, where an optimisation of these processing conditions resulted in obtaining powders chemistry with a minimal amount of secondary phases present.

The samples were divided into the following groups (see Table 4.1):

Ar_ B group

Samples in this group were processed in an Ar atmosphere for up to 30 minutes and with a ball electrode. This experiment was carried out to determine whether or not excessive EDAMM processing times influences the final crystal structure of $BaO - TiO_2$ processed powders. This analysis was carried out via X-ray diffraction.

TaC_Ar group

In this group, a coating of TaC was applied onto the surface of the electrode to: 1. reduce the amount of Fe contamination in the milled powders and/or shift the type of contamination e from Fe to Ta, 2. to possibly alter the temperature of the plasma by introducing a barrier between the stainless steel electrode because it has the potential to change the characteristics of the plasma. The latter are discussed more widely by A. Aksenczuk in his PhD thesis [88]. The samples were processed in EDAMM for 1, 2, and 4 minutes and the results for the sequence of processing conditions are presented. This analysis includes an X-ray diffraction (XRD), scanning electron microscopy (SEM), and energy dispersive spectroscopy (EDS). Moreover, SEM/EDS

analysis of the surface of the TaC coated electrode and transmission kikuchi diffraction (TKD) was carried out on the lamella prepared from the surface layer of the electrode coated with TaC.

O_2/Ar group

A 10%O_2/Ar mixture was used to increase the temperature of the plasma due to the higher energies carried by O_2molecules and then compare the result to monoatomic Ar [51]. The samples were processed in EDAMM for 1, 2, and 4 minutes and the results for the sequence of processing conditions are presented. The results presented in this chapter include the XRD, SEM and EDS analysis.

Ar_C group

The starting powders of BaO and TiO_2 were weighted in stoichiometric ratios and then an additional amount of 0.006g (3 wt%) of graphite was added. The mixture was processed under the same conditions as the Ar group samples. Due to the possible transfer of Ta and C into the processed powders, adding graphite to the mixture could help the possible effect it has on the processed powders.

Ar_Ta group

After mixing the BaO and TiO_2 powders in stoichiometric ratios, an additional amount of 0.022g (11 wt%) of Ta powder was added, and then an X-ray diffraction analysis of the resultant powders was carried out.

Table 4.1: Detailed processing conditions for preparation a variety of $BaTiO_3$ samples.

Group name	Sample name	Processing conditions					
		Gas type	**Pulse on/off ratio (%)**	**Pulse intensity (%)**	**Time (min)**	**Electrode type**	**Power input type**
Ar_B	Ar_B_20	Ar	70	80	25	SS** ball	Direct current
	Ar_B_30	Ar	70	80	30	SS** ball	Direct current
TaC_Ar	TaC_Ar_1	Ar	70	80	1	TaC coated SS** ball	Direct current
	TaC_Ar_2	Ar	70	80	2	TaC coated SS** ball	Direct current
	TaC_Ar_4	Ar	70	80	4	TaC coated SS** ball	Direct current
O_2/Ar	O_2/Ar_1	10%O_2/Ar	40-50*	80-90*	1	SS** ball	Direct current
	O_2/Ar_2	10%O_2/Ar	40-70*	80-90*	2	SS** ball	Direct current
	O_2/Ar_4	10%O_2/Ar	40-90*	80-90*	4	SS** ball	Direct current
Ar_C	Ar_C_4	Ar	40-90*	80-90*	4	SS** ball	Direct current
Ar_Ta	Ar_Ta_4	Ar	40-90*	80-90*	4	SS** ball	Direct current

* indicates gradually increasing electrical conditions throughout the experiment ** SS-stainless steel

Table 4.2: Processing conditions of TaC_Ar group powders.

Total time (min)	**Processing time (s)**	**Pulse on/off ratio (%)**	**Pulse intensity (%)**	**Target current (A)** δ = ± 0.1 A	**Power input (A)** δ = ± 0.07 A	**Effective power (A)** δ = ± 0.02 A	**Vibrations (V)**
4 min	30	70	80	3.89	2.46	0.45	0.8

Table 4.3: Processing conditions of O_2/Ar group powders.

Total time (min)	**Processing time (s)**	**Pulse on/off ratio (%)**	**Pulse intensity (%)**	**Target current (A)** δ = ± 0.1 A	**Power input (A)** δ = ± 0.07 A	**Effective power (A)** δ = ± 0.02 A	**Vibrations (V)**
4 min	30	40	80	1.20	0.40	0.13	0.8
	30	0	0	0	0	0	0.8
	30	50	80	2.20	1.30	0.28	0.8
	30	60	90	3.50	2.18	0.42	0.7
	60	70	90	4.20	2.71	0.50	0.7
	60	80	90	4.67	3.10	0.59	0.7
	30	90	90	4.65	3.07	0.57	0.7

4.3 Results and discussion

4.3.1 "Ar_B group" samples

Samples in group Ar_B were processed in an Argon atmosphere for 25 and 30 minutes. The results show that processing in an Ar atmosphere and using clean stainless steel electrode always results in a mixture of hexagonal (PDF no. 34-0129) and cubic (PDF no. 05-0626) polymorphs of $BaTiO_3$. Many previous experiments also revealed that the ratio of those two phases is quite random, which supports the fact that the processing time in constant electrical conditions is not a factor when forming a specific polymorph of $BaTiO_3$. In our case, the experiment was carried out several times and each time the hexagonal/cubic $BaTiO_3$ ratio varied. Thus, analysis of the phase content based on the two graphs presented in Figure 4 would not be representative. The following research was carried out to determine the specific conditions needed to obtain only one phase cubic or hexagonal polymorph.

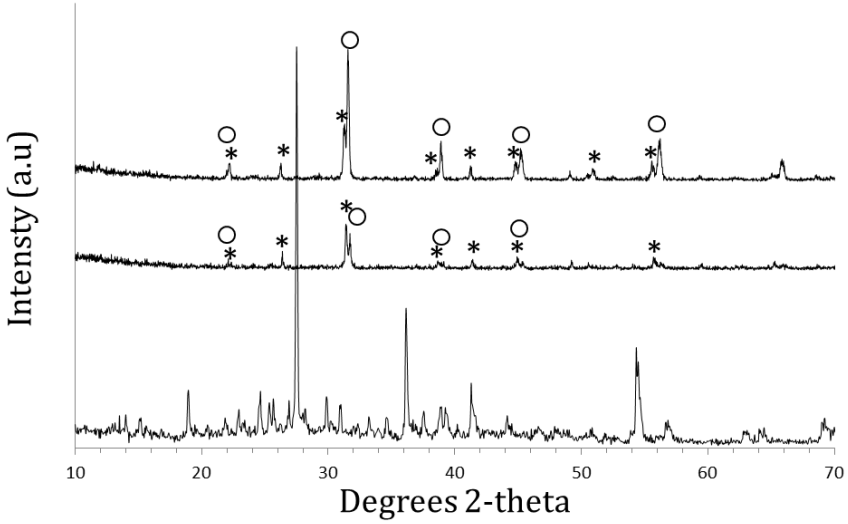

Figure 4.4: XRD of the Ar_B group samples; a) starting powder, and $BaO - TiO_2$ processed for b) 25 and c) 30 min. Legend: ○ - cubic $BaTiO_3$ and * - hexagonal $BaTiO_3$.

4.3.2 "TaC_Ar group" samples
Electron microscopy and X-ray diffraction

BaO and TiO_2 powders of the TaC_Ar group were processed for up to 10 minutes in an Ar atmosphere using ball electrode coated with TaC; the electrical conditions set for processing are shown in Table 2.

Figure 4.5 presents the XRD patterns for samples of the TaC_Ar group; here the XRD analysis shows that an almost single phased cubic $BaTiO_3$. It obtained within 2 minutes of processing, with a minor amount of a secondary phase and further processing did not lead to further transformation into a high temperature polymorph with a hexagonal crystal structure. Therefore, once the temperature reached its maximum and the cubic phases were formed, there is no further increase in the processing temperature.

Figure 4.6 shows the XRD pattern of TaC_Ar_1 sample; here the peaks were indexed to three phases; cubic $BaTiO_3$, a remnant of the TiO_2 starting powder- rutile and the nanocrystalline phase of orthorhombic $BaTiO_3$. The latter is most commonly reported as being of the Amm2 space group, but the existence of a Pnma type of structure at room temperature and under high pressure has been reported [89, 90]. Because of the nature of EDAMM and a history of reported nanostructural and metastable phases, this result is not surprising despite the fact that this crystal structure is considered to be stable below 5°C. As stated in [91], the stability of $BaTiO_3$ phases is connected to the size of the crystallites, so if the crystallite is smaller than 280nm, $BaTiO_3$ probably exists as an orthorhombic crystal rather than tetragonal or cubic.

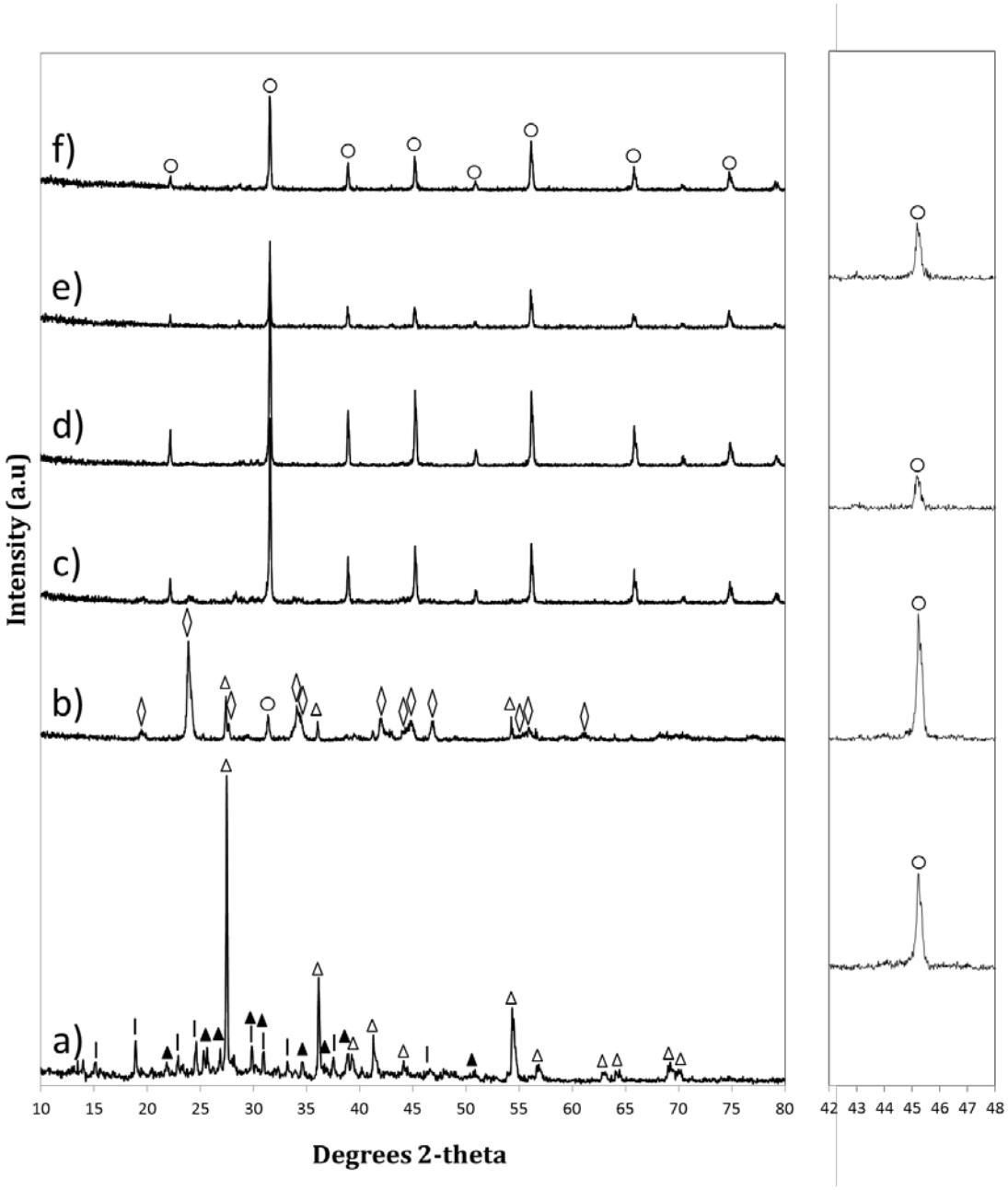

Figure 4.5: XRD patterns of a) $BaO-TiO_2$ starting powders, and TaC_Ar group powders processed in EDAMM for b)1 min, c)2 min, d)4min e)5min and f)10 min. On the right hand side a magnified 42-48 degrees 2-theta peak is shown as a proof of cubic crystal structure. Legend: Δ - TiO_2 rutile, | - BaO, ▲- BaO_{1-x}, ◊ - orthorhombic $BaTiO_3$ and ○ - cubic $BaTiO_3$.

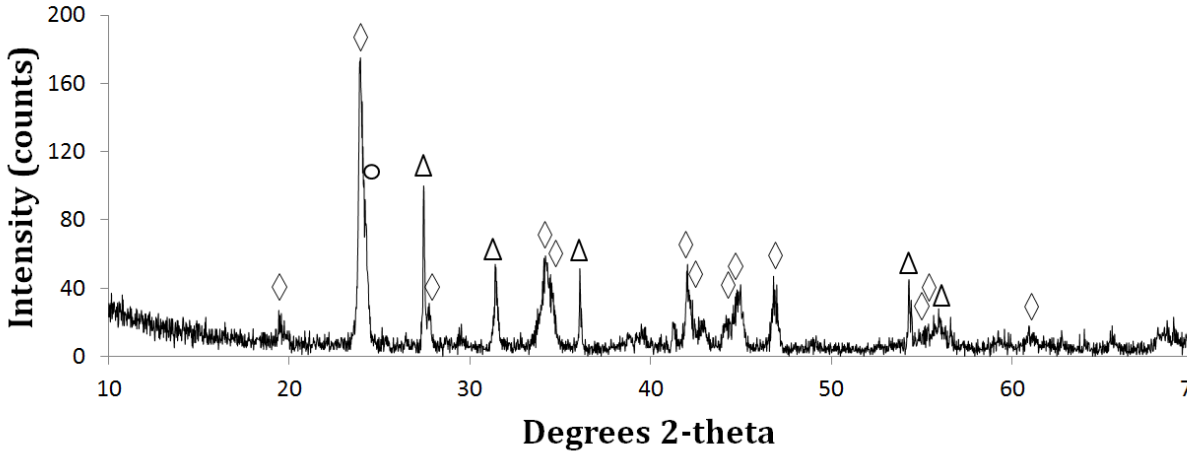

Figure 4.6: X-ray diffraction pattern of TaC_Ar_1 sample. Legend: Δ - TiO_2 rutile, ○ - cubic $BaTiO_3$ and ◊ - orthorhombic $BaTiO_3$.

Figure 6 shows the XRD spectrum with broad peaks corresponding to the nanostructural Pnma type of orthorhombic $BaTiO_3$, previously observed in [89, 90]. Through the selected area, the electron diffraction of the nanocrystalline powder particles (Fig. 4.7b) shows that diffraction spots corresponding to the specific set of planes in Pnma crystals differ slightly from than indicated in the literature; they are compared in Table 4.4.

Table 4.4: Orthorhombic $BaTiO_3$ reflection list compared with the literature data [89].

Experimental d-spacing	Lit. d-spacing	Deviation	h	k	l
4.576	4.556	0.020	0	1	1
3.752	3.712	0.040	1	1	1
3.552	3.645	0.093	2	0	0
3.106	3.215	0.109	2	1	1
2.652	2.658	0.006	0	2	0
2.649	2.631	0.018	2	1	1

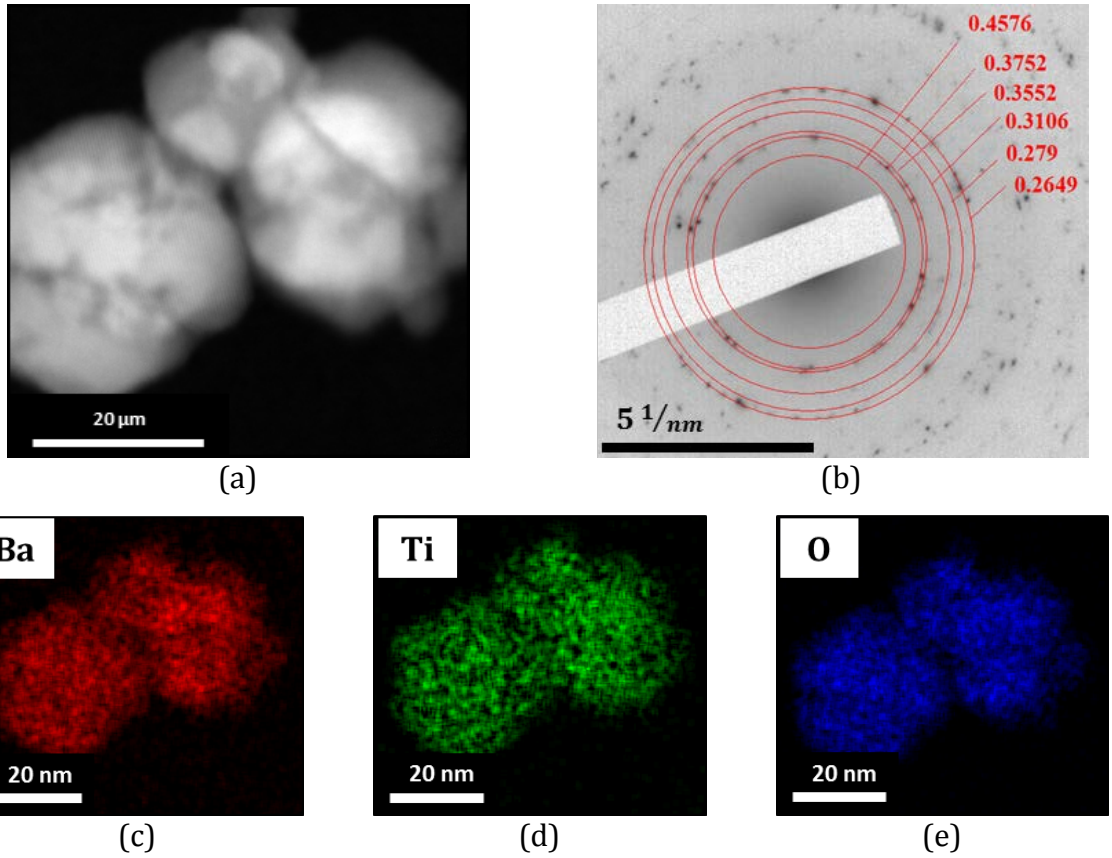

Figure 4.7: (a) TEM image of the nanoparticles obtained after EDAMM processed TaC_Ar_1 sample, (b) electron diffraction of the particles in (a) and (c-e) elemental distribution of those particles.

The elemental distribution obtained through scanning transmission electron microscopy (STEM) confirmed the uniformity of Ba and Ta in the particles observed, despite their irregular shape, and a global analysis of the map spectrum showed that Ba and Ti constituted 51.2 ± 0.86 at% and 48.8 ± 1.04 at%, respectively. All these analytical techniques proved the crystalline structure, chemical composition, and nanocrystalline character observed earlier on the XRD pattern.

An SEM analysis of the polished surface of the pellet (Fig. 4.8a) pressed from the same sample (TaC_Ar_1) showed that, apart from the nanoparticles, there were also larger particles as well. The averaged values of the spot EDS confirmed that the lighter grains

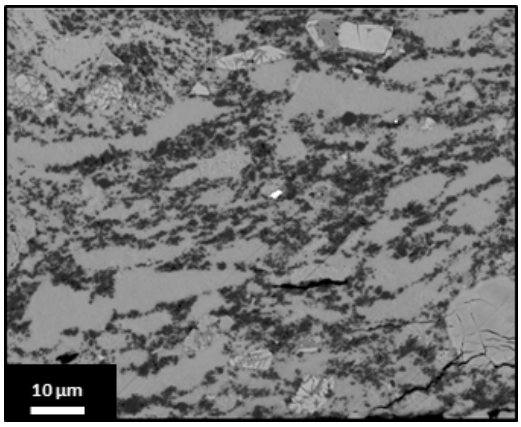

(a)

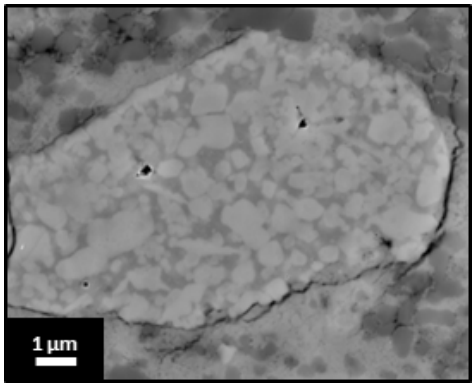

(b)

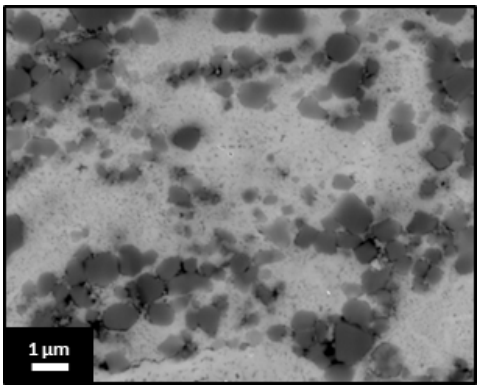

(c)

Figure 4.8: Back-scattered SEM images of the cross-section of the pellet pressed from the TaC_Ar_1 sample. (a) is an overview of the sample in low magnification, (b) partially processed $BaTiO_3$ particle and (c) area with TiO_2 particles (dark) and nanostructured $BaTiO_3$ (lighter).

have a chemical composition close to stoichiometric $BaTiO_3$ (Fig. 4.8b). The grain sizes of this phase suggested that, with the correlation to the XRD result, they corresponded to cubic $BaTiO_3$ phase, whereas a darker phase had a Ba:Ti ratio of ~1:2.5, which is close to the composition of $Ba_2Ti_6O_{13}$. In other areas of the pellet, there are Ti and Ba-rich areas that are related to the presence of starting powders.

According to the XRD results shown in Figure 4.5c, 2 minutes of processing in EDAMM is sufficient to transform the $BaO - TiO_2$ starting powders into a near single phase cubic $BaTiO_3$, denoted as TaC_Ar_2. Cubic crystals are often obtained during processing, but they are unstable and transform to a tetragonal form at room

temperature. The stabilisation of a cubic type of $BaTiO_3$ crystal structure could be due to the calcination temperature [92], the starting materials, grain sizes, and the preparation route [93]. The effect of grain size is summarized in [91] where the critical size needed to induce a cubic-tetragonal transformation was 25-200nm. Those results were compiled from processing methods such as precipitation from barium tytanyl oxalate tetrahydrate (BTOT), sol-gel, ground powder, hydrothermal, and thin film and powders crystallised from glass. It was further proven in [93], that cubic crystal can be further stabilised by increased stresses in the material and defects that hinder cubic-tetragonal phase transformation. It was long suspected that EDAMM processing could induce these levels of stresses in powder materials and now the experimental data seems to confirm this theory. Here, the cubic crystal structure is sustained even though the grain sizes exceed 200 nm.

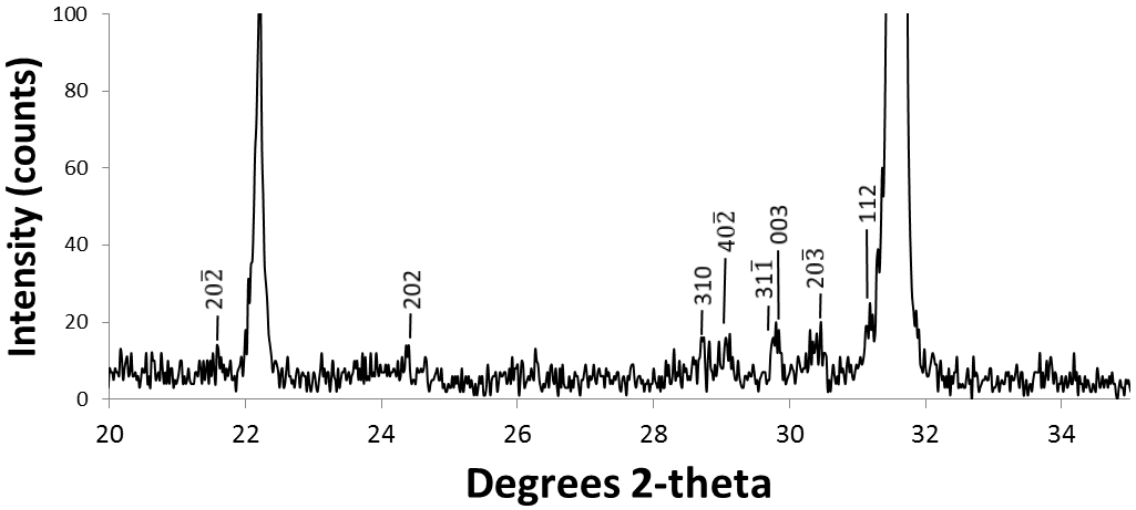

Figure 4.9: X-ray diffraction and indexing of the secondary phase found in TaC_Ar_2 and TaC_Ar_4 samples.

In the XRD pattern, the tetragonal crystal structure manifests itself as a double peak between 45-46 2-theta degrees. The magnified XRD pattern within that range, shown as an inset in Figure 4.5 shows there is no such split.

There is a range of smaller peaks close to the main, near 30 degrees 2-theta peak, whose positions were identified and assigned to $Ba_2Ti_4O_{13}$, with a monoclinic crystal structure that belongs to the space group 12, C12/m1 (Fig. 8).

Powder particles from the TaC_Ar_2 sample were pressed into a pellet to study their microstructural features. The structural integrity of the pellet was much better than TaC_Ar_1 and the particles were much more uniform in size. Moreover, back-scattered imaging revealed that most of the light grains (over 90%) have the same circular shape whereas the darker, secondary phase has an irregular shape which fills the spaces between the former one (Fig. 10b).

Figure 4.10b-f shows the elemental distribution obtained through EDS is shown. Through a quantitative analysis the light grains visible in Figure 4.10, the Ba:Ti ratio was assessed as approximately 1:1.1 which is consistent with previous XRD data (Fig. 4.5c) of cubic $BaTiO_3$. The elemental composition of this phase indicates a uniform distribution of Ba, Ti, and Ta elements, with the latter assessed to be ~0.8at%. Fe-contamination in the sample was localised and mainly in the secondary phase areawhere also traces of Al were found. The Ba:Ti ratio in this region was approximately 1:2.5.

The microstructure of the typical region of the TaC_Ar_4 pellet is shown in Figure 4.11a. The main phase of a lighter colour was assessed to make up around 85% of the total area of the particle, which seems to have sub-grains in its structure. Quantitative spot analysis of the grains revealed that the average Ba:Ti ratio is ~1.1, which corresponds to the $BaTiO_3$phase that was indexed before in the XRD pattern (Fig. 4.5d).

Those areas were found to be richer in Ta, but the level detected by EDS was less than 0.5 at%. However, the secondary phase has a much less uniform elemental distribution with areas rich in Fe, and Ti. A quantitative analysis shows that the Ba:Ti ratio in this region is ~1:2.5 which is consistent with the $Ba_2Ti_6O_{13}$ secondary phase

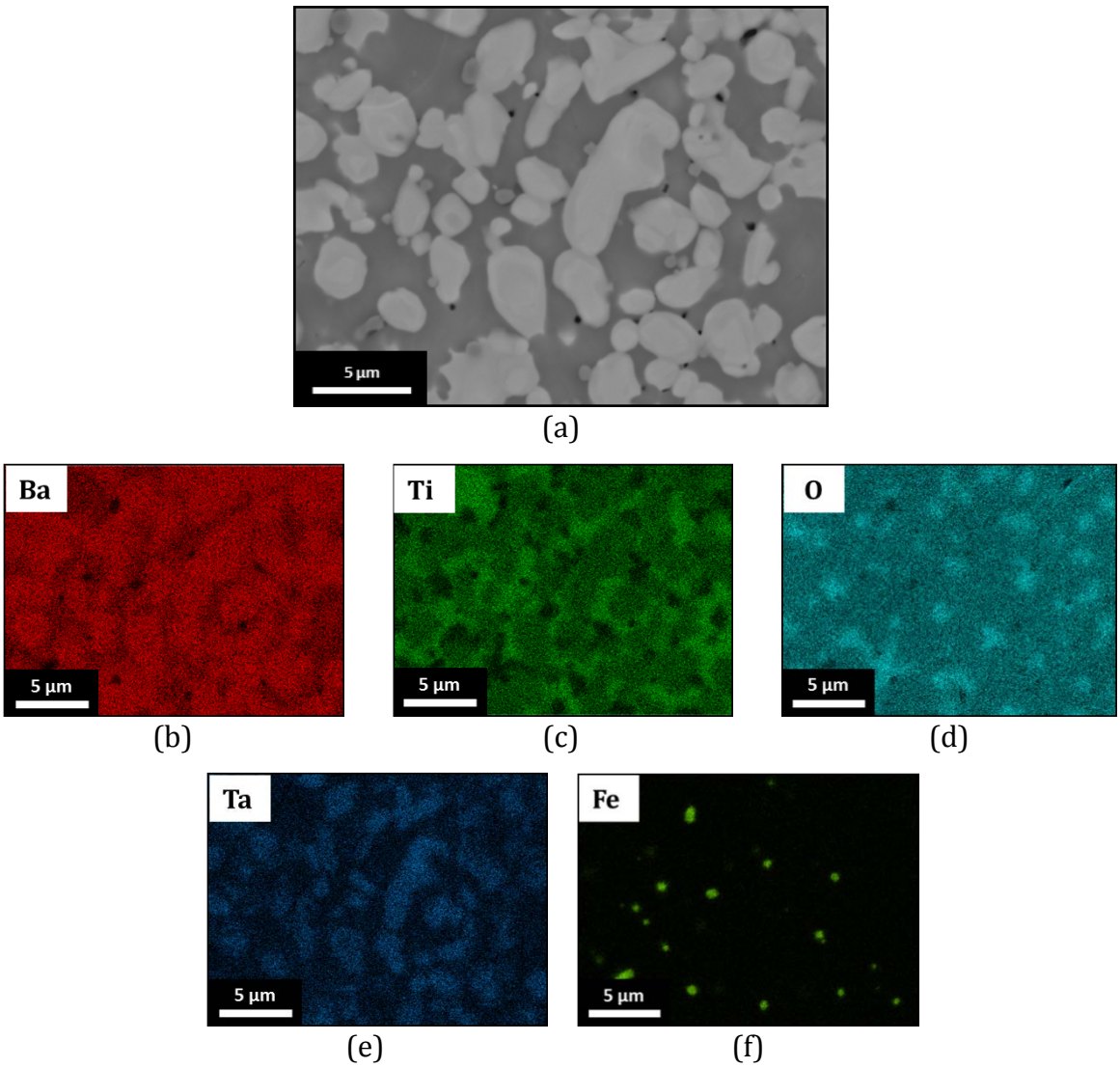

Figure 4.10: EDS mapping of the TaC_Ar_2 pellet. (a) backscattered electrons image, (b) quantitative analysis of the light and dark phases and (b-f) elemental distribution of the elements.

previously observed in the XRD pattern (Fig. 4.5). Having a locally increased Fe contamination level it may also exist as one of the isostructural phases with the same monoclinic C12/m1 space group, namely $Ba_2Ti_4Fe_2O_{13}$ or $Ba_4Ti_{10}Fe_2O_{27}$. Later in the thesis, the monoclinic phase, for simplicity reasons is going to be called monoclinic $Ba_2Ti_6O_{13}$ phase.

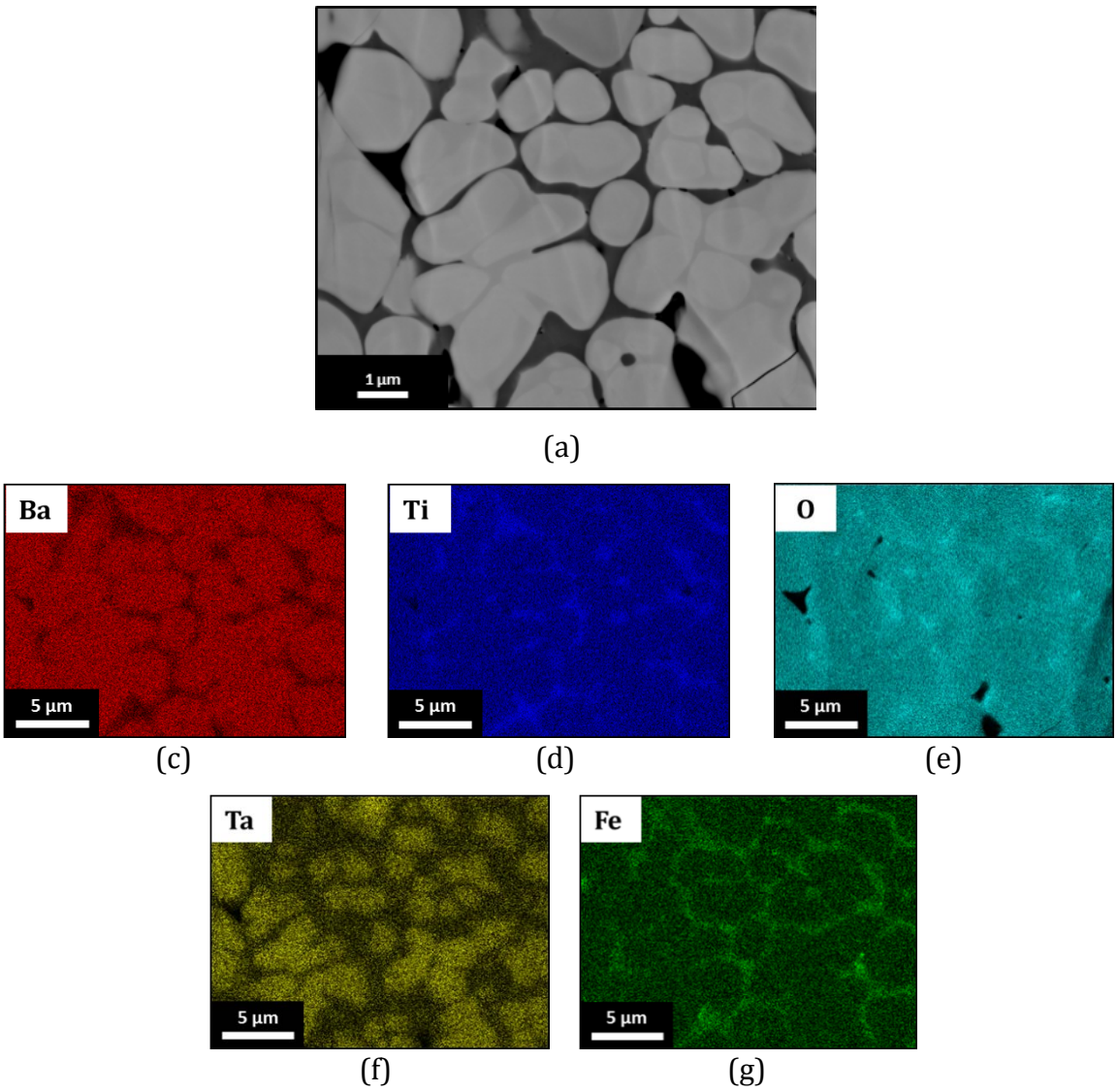

Figure 4.11: EDS mapping of the TaC_Ar_4 pellet. (a) backscattered electrons image, (b) quantitative analysis of the light and dark phases and (b-g) elemental distribution of the elements.

4.3.3 TaC coating on the stainless steel electrode- X-ray diffraction and SEM/EDS characterisation

The previous section shows how the TaC coating on the EDAMM electrode affects the final crystal structure of $BaTiO_3$. The cubic crystal structure of $BaTiO_3$, stable in the 120-1420 °C temperature range, was identified by an XRD and EDS quantitative analysis of the powder's cross-sections. In fact, unlike the sample of group Ar_B where no TaC coating was applied, hexagonal and cubic crystal structures prevailed even after 30 minutes of EDAMM processing. It is thought that the TaC coating affects the the plasma character, which was previously observed in [88]. As a result, the processing temperature decreased so that the lower temperature polymorph of $BaTiO_3$ could stabilise and its transformation to a hexagonal polymorph hindered.

The characterisation of the surface of the ball electrode after being coated with TaC is shown in Figure 4.12. X-ray analysis shows that the coating prepared from Ta and C powders has a crystal structure of TaC (PDF 03-1137). Additionally, some characteristic peaks contributing to pure Ta and the Fe_3C (stainless steel electrode) can be found.

EDS analysis of the TaC coated EDAMM electrode shown in Figure 4.12b-h shows that the coating is non-uniform. Ta-rich areas make up only 25% of the area shown in Figure 4.12c however a large amount of the surface is also Al,O-rich. The latter, although the electrode was thoroughly cleaned, is a remnant of the Al_2O_3 sand from the sand blasting surface cleaning. The underlying stainless steel material of the electrode on the other hand, manifests itself on the Fe map, shown in the Fig. 4.12d.

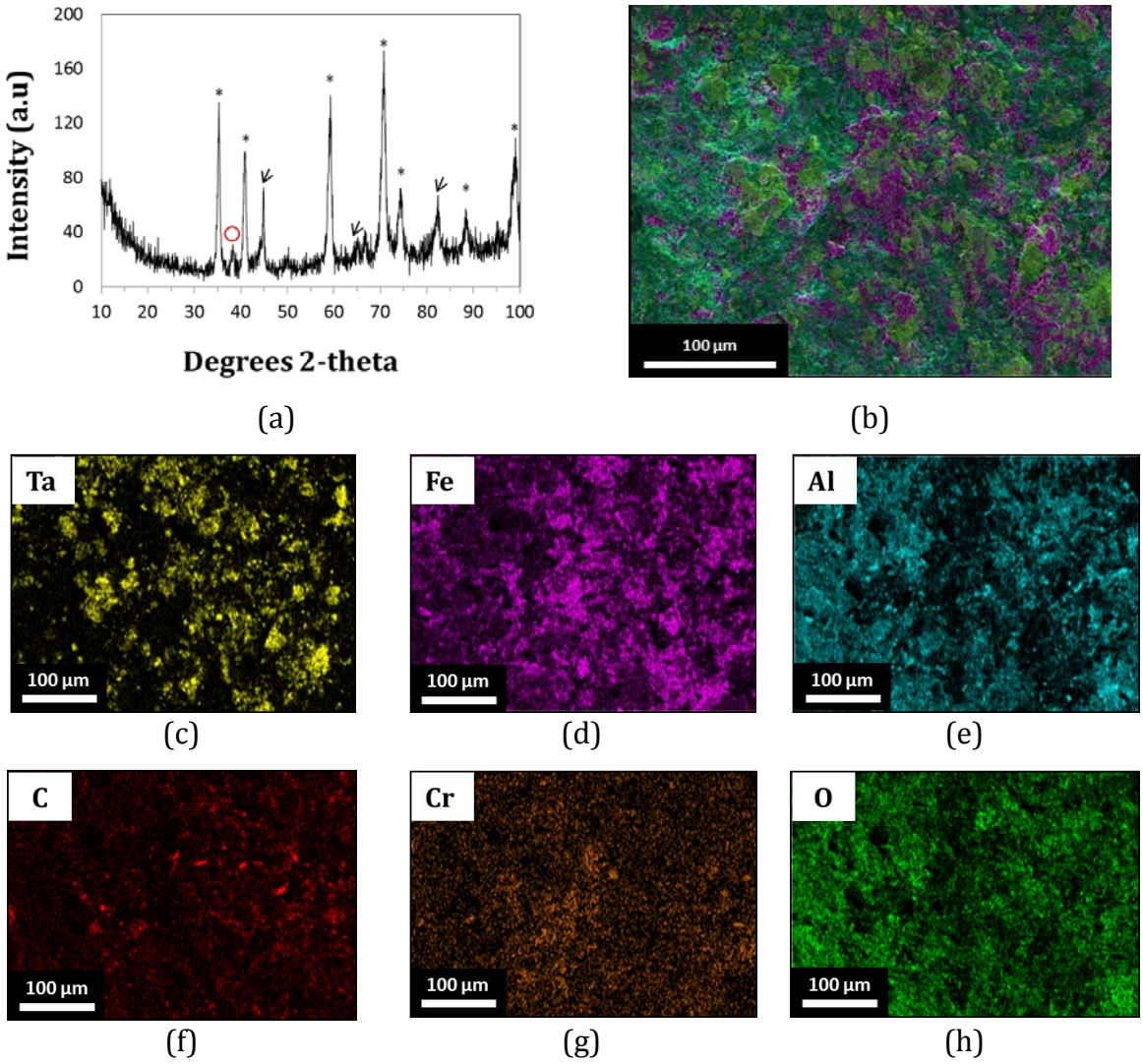

Figure 4.12: (a) XRD and (b) elemental distribution map of the EDAMM electrode surface after TaC coating, and (c-h) elemental distribution of each element. Legend: ↙- Fe_3C, *- TaC and ○- Ta.

The results presented above suggest that the surface properties of the EDAMM ball electrode changed due to the TaC coating treatment. It is believed that the electrons escaping the electrode's surface and forming the plasma discharge are therefore less efficient in the ionization of the Ar gas and so decreasing the overall temperature of the plasma during processing.

4.3.4 "O_2/Ar group" samples-
Electron microscopy and X-ray diffraction

The O_2/Ar group of samples represents the results of EDAMM processing where $10\%O_2$ was introduced into the otherwise inert Ar atmosphere. Details of the processing conditions are shown in Table 2.

The sequence at which the powders were processed involved low electrical conditions at the beginning of the process, followed by the pause in the electrical current input for a short period of time, while retaining the vibrations. It is thought that the initial stage of processing reduces the level of water absorbed on their surfaces and therefore improves their mixing efficiency, hence, the mixing of the powders without the electrical current was applied after the first 30 seconds. The next steps included sequenced increase of the pulse pulse on/off ratio and pulse intensity of the EDAMM power supply setting. These parameters were optimised to obtain the maximum amount of $BaTiO_3$ and the minimum amount of secondary phases and remnants of the starting powders.

Figure 4.13 shows the XRD patterns of $BaO - TiO_2$ processed in the O_2/Ar group of samples conditions are shown for up to 4 minutes of processing. It has been found that the hexagonal and cubic types of $BaTiO_3$ crystal structures could be indexed after just 1 minute of EDAMM processing (Fig. 4.13b). The starting powder peaks were also indexed at this stage.

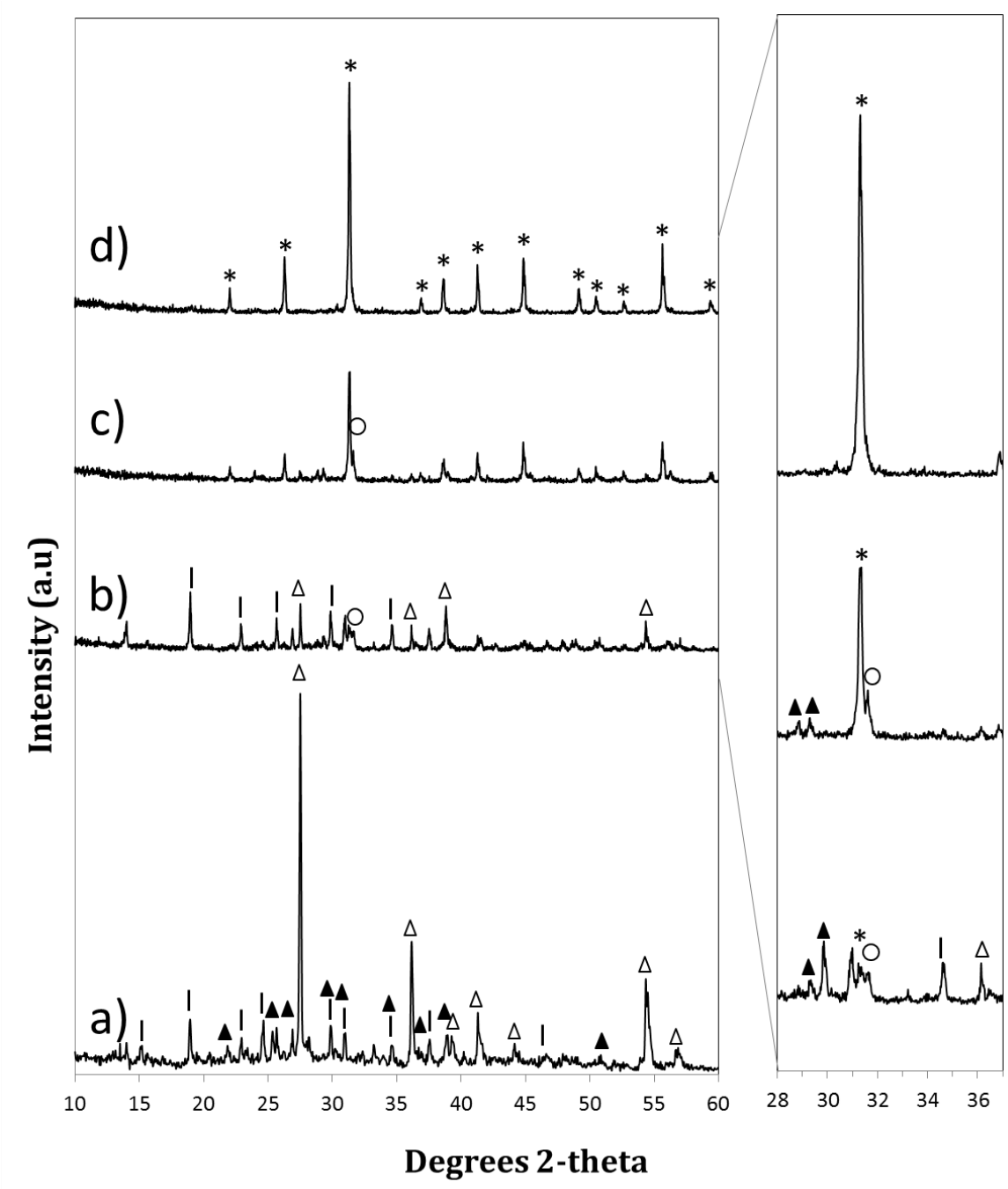

Figure 4.13: XRD patterns of a) $BaO - TiO_2$ starting powders, and O_2/Ar group powders processed in EDAMM for b)1 min, c)2 min, d)4min. On the right hand side a magnified patterns around 28-37 degrees 2-theta are shown. Legend: Δ - TiO_2 rutile, | - BaO, ▲- BaO_{1-x}, ○ - cubic $BaTiO_3$ and * - hexagonal $BaTiO_3$.

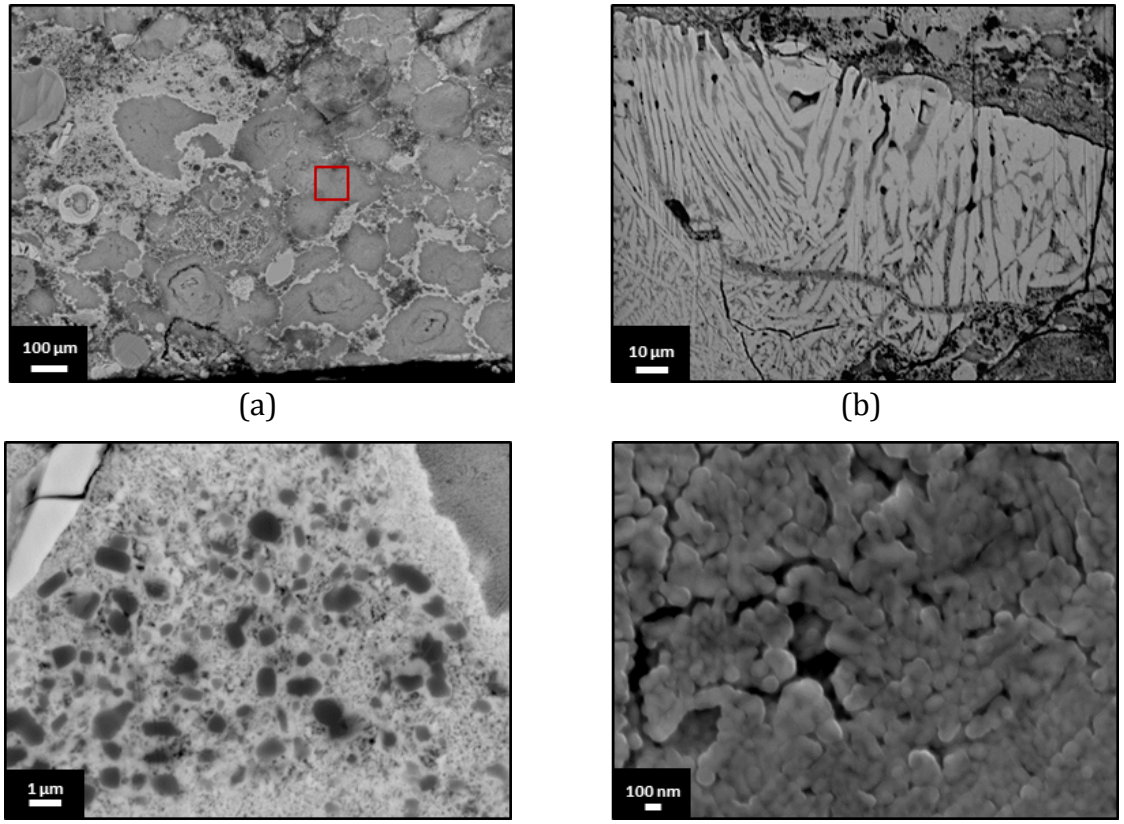

(a) (b)

(c) (d)

Figure 4.14: Back-scattered SEM images of the cross-section of the pellet pressed from the O_2/Ar_1 sample. (a) is an overview of the sample in low magnification, (b) partially processed $BaTiO_3$ particle, (c) the area with TiO_2 particles (dark) and nanostructured $BaTiO_3$ (lighter), and (d) nanoparticles observed in the area marked by a red square in (a.)

The SEM image of backscattered electrons of the cross section of an O_2/Ar_1 pellet (Fig. 14a) shows some regions with vastly different chemistries that contributed to the remnants of the starting powders (Fig. 14c) mentioned previously, as well as some fully processed particles (Fig. 14b). This is an important result because it shows that even intermediate electrical conditions (50% pulse module and 80% pulse intensity, O_2/Ar) already result in the growth of a high temperature stable polymorph of $BaTiO_3$.

Additionally, large amount of nanoparticles were observed (Fig. 14d) which were assessed by point EDS analysis to have an approximately 1:0.9, Ba:Ti ratio. Due to a previous XRD examination and the presence of the above mentioned hexagonal crystal structure, it is safe to assume that those particles are monocrystalline cubic $BaTiO_3$ particles.

In order to improve the efficiency of EDAMM processing in O_2/Ar atmosphere, the electrical conditions were increased further, and after 2 minutes of EDAMM processing majority of the phase was indexed as hexagonal $BaTiO_3$ with a small amount of cubic polymorph and secondary phase (Fig. 13c). In terms of the microstructure, the SEM backscattered electrons image of a cross section of the O_2/ Ar_2 pellet (Fig. 15a) shows that some regions with chemistries contributed to the starting powders (Fig. 15c), as well as some fully processed particles (Fig. 15b). It should be noted that the microstructure of the grains observed in this sample differs from the characteristic cubic $BaTiO_3$ grains presented earlier for the TaC_Ar samples. These microstructural features are well known for the martensitic transformation that occurs in martensitic steels, where FCC austenite transforms into the BCT (body centered tetragonal) crystal structure upon quenching from a high temperature. Although the speed at which EDAMM processed powders is not yet known, their microstructural characterisation gives some indication into the possible processes.

Interestingly, in the regions where particles were apparently not processed, high magnification imaging revealed a large amount of fibrous structures that were approximately 165 nm in diameter, which is a slightly larger than 135nm diameter particles processed for 1 minute. An EDS analysis of these regions revealed either pure Ba or Ba with up to 20-33at% of Ti.

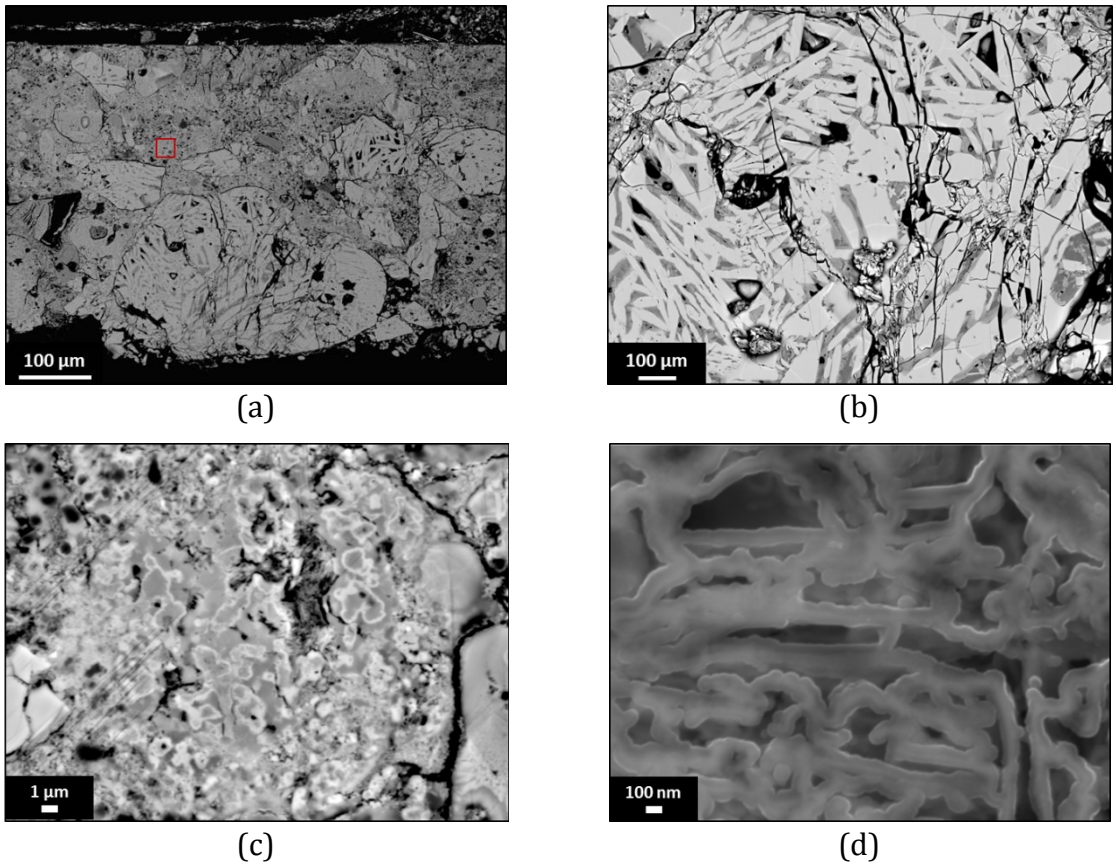

(a) (b)

(c) (d)

Figure 4.15: (a) Cross-sectional view of the O_2/Ar_2 sample pellet, (b) BSE image showing typical microstructural features, (c) area with only partially processed powders, and (d) nanorods observed in a region denoted as a red square in (a).

XRD analysis of the powders processed for 4 minutes in EDAMM and denoted as O_2/Ar_4 suggested that most of the powders consisted of hexagonal $BaTiO_3$, and indeed, the BSE image presented in Figure 4.15 a shows that the elongated grains are almost 81% of the total area of the analysed particle. Moreover, EDS mapping of the particle indicates there was almost no change of the Ba:Ti ratio in the elongated grains and secondary phase, but the latter does contain a much larger amount of Fe; this result is similar to the sample TaC_Ar_2 and TaC_Ar_4 (Fig. 4.10 and 11).

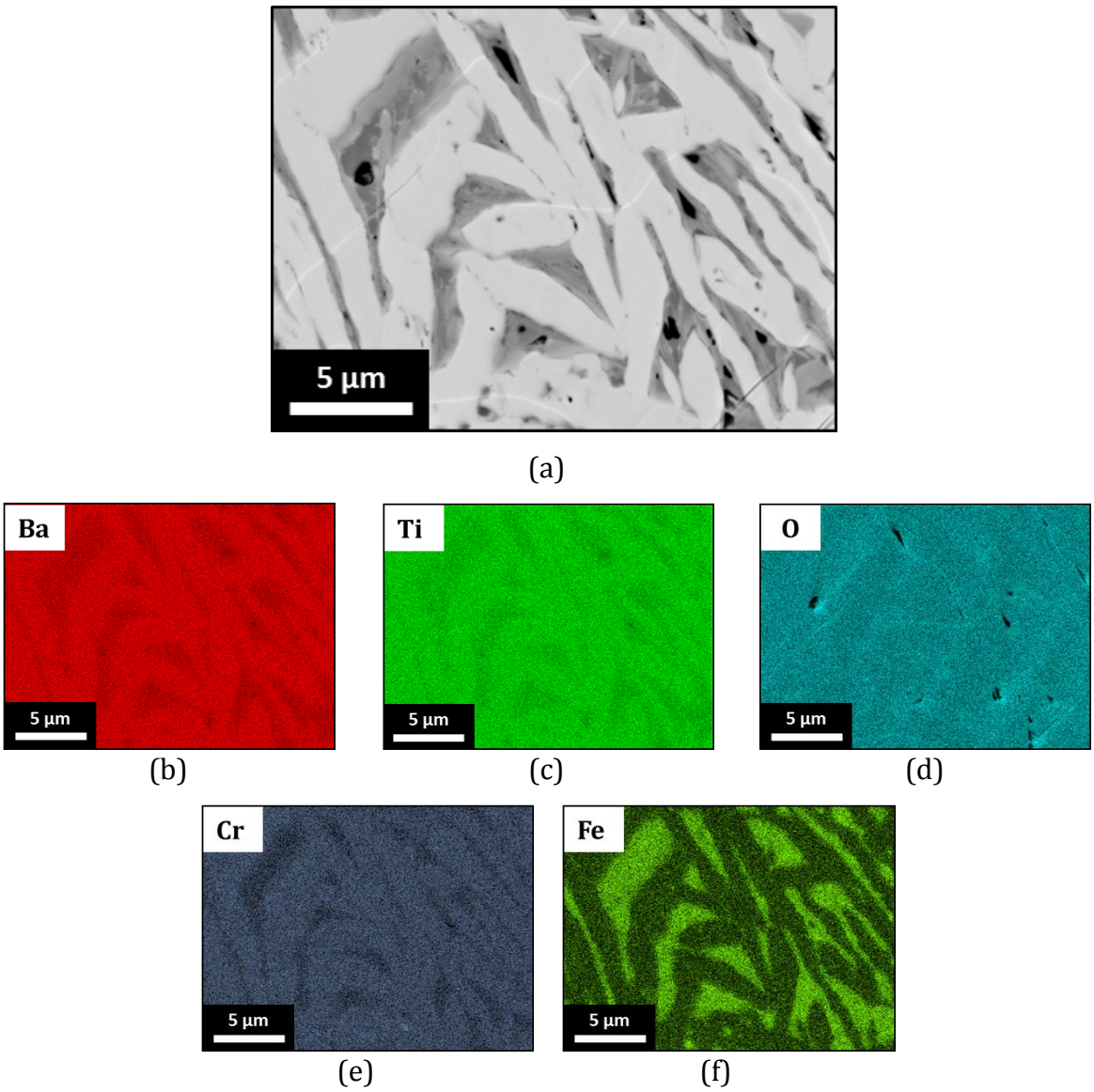

Figure 4.16: EDS mapping of the O_2/Ar_2 sample pellet. (a) backscattered electrons image, (b)quantitative analysis of the light and dark phases and (b-f) elemental distribution of the elements.

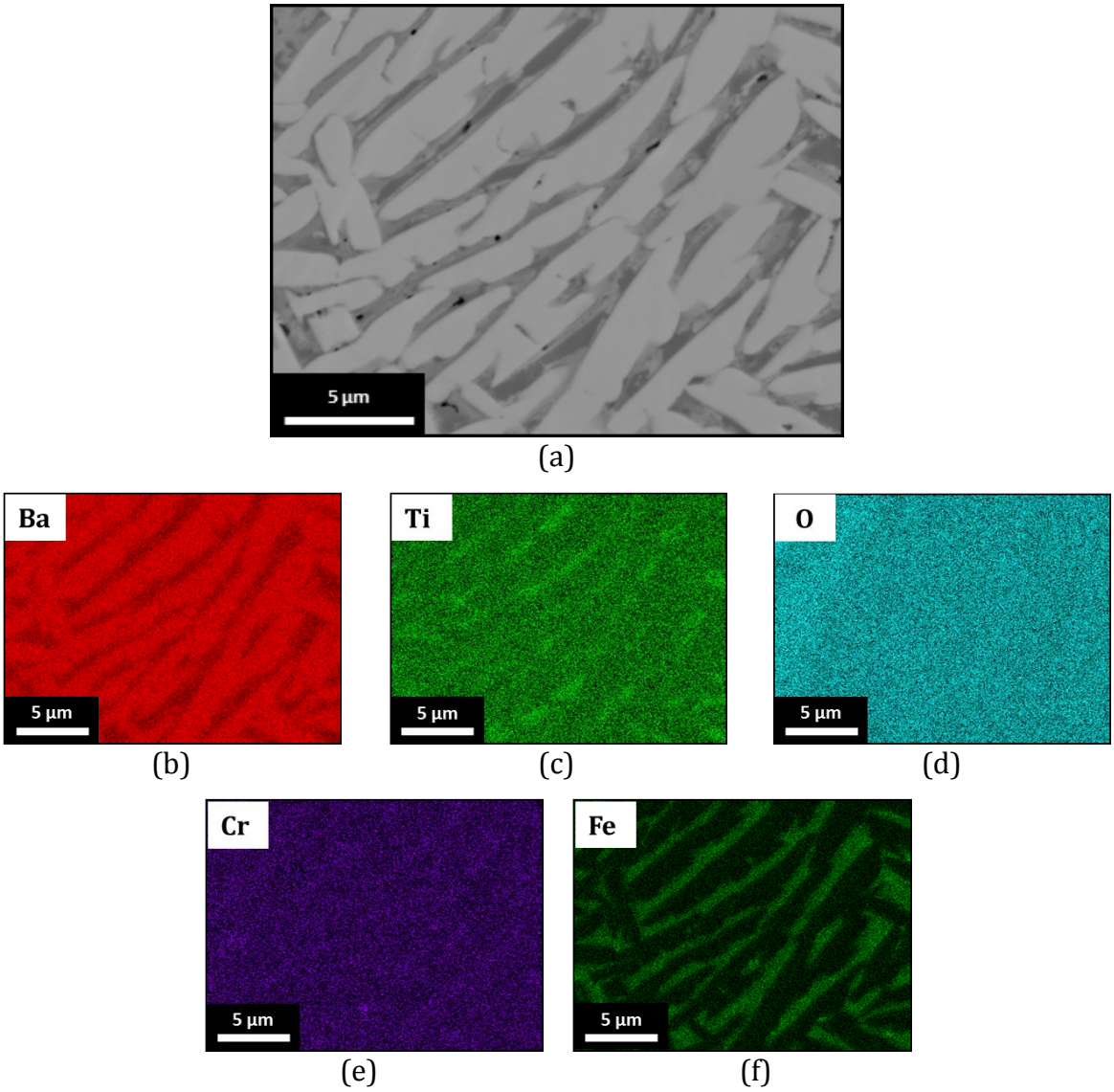

Figure 4.17: EDS mapping of the O_2/Ar_4 sample pellet. (a) backscattered electrons image, (b) quantitative analysis of the light and dark phases, and (c-f) elemental distribution of the elements.

4.3.5 Supplementary experiments

This section presents other results that provide more information about the influence of a certain group of elements on the processing conditions and $BaTiO_3$ synthesis. In previous sections it was shown that the TaC coating on the electrode has a significant influence on the type of $BaTiO_3$ crystal structure obtained during EDAMM processing.

4.3.5.1 Ta doped $BaTiO_3$

Perovskite structures can effectively accommodate large amounts of foreign atoms in their crystal structure. Due to the EDAMM components heating up during the processing, it is likely to observe some elements being transferred/diffuse into the milled powders. The main contaminant of stainless steel components is Fe but when one electrodes is coated with TaC those elements will probably be transferred. It was shown in the previous sections that in this case, low levels of Ta were found in $BaTiO_3$ grains, but the level of carbon concentration had not increased.

In the following experiment, starting powders of $BaO - TiO_2$ were mixed in stoichiometric ratios and then an additional amount of 11wt% of Ta powder was added. The powders were then processed for 4 minutes in EDAMM in the same conditions as the TaC_Ar samples. XRD analysis revealed that the final crystal structure of $BaTiO_3$ has cubic and hexagonal crystal structures with majority of the former. It seems that doping $BaO - TiO_2$ powders with small amounts of Ta stabilises the cubic crystal structure although the uneven distribution of Ta powder means that some areas remain unaffected by the addition of Ta. Perhaps longer milling times and a sequential approach to the addition of Ta powder would reveal the complete formation mechanism; this will be considered in future work on this subject.

Nevertheless, unlike the samples milled in pure Ar and without the TaC coating on the electrode, small amounts of additional Ta resulted in more cubic types of $BaTiO_3$ after

only 4 minutes of processing. It can therefore be concluded that Ta doping does not affect the sizes of the crystallite because the XRD peaks appear to have a similar width to previously observed samples of TaC_Ar.

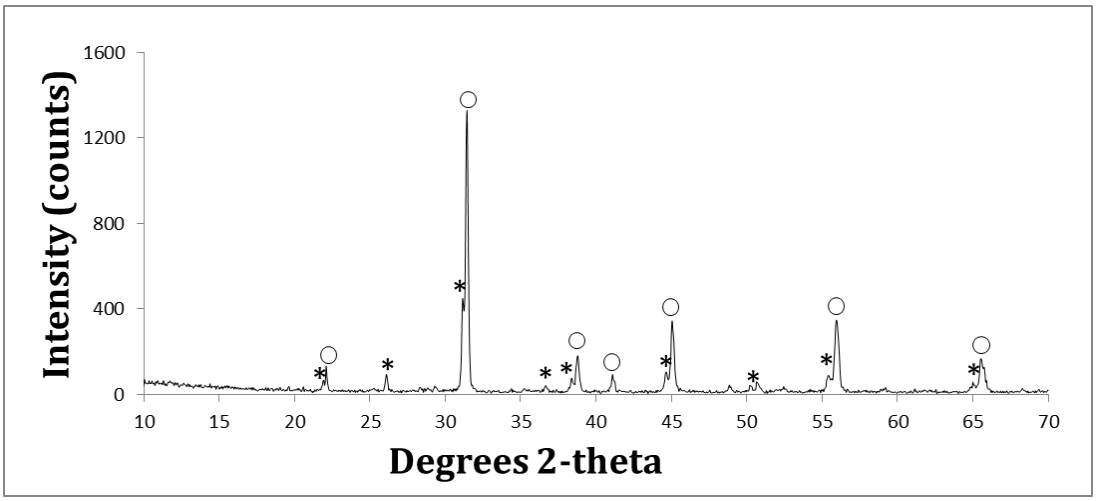

Figure 4.18: XRD pattern of the Ta-doped $BaTiO_3$. Legend: ○-cubic $BaTiO_3$ and *-hexagonal $BaTiO_3$.

4.3.5.2 C doped $BaTiO_3$

To assess the influence of C doping on the formation of $BaTiO_3$, 2.75 wt% of loose graphite was added to the $BaO - TiO_2$ starting powders and the mixture was processed for 4 minutes in EDAMM in Ar with a clean electrode. It was found that the particle sizes of as-prepared powders were much smaller (1.4± 0.3 μm) than the previously examined $BaTiO_3$ (Fig. 19a) doped with Ta.

Figure 19b shows the XRD pattern obtained from the loose sample doped with C; here the crystal structure and particle size are completely different from the $BaTiO_3$ doped with Ta because it seems that only a hexagonal type of $BaTiO_3$ with some minor possibly $Ba_2Ti_6O_{13}$, was obtained in this experiment.

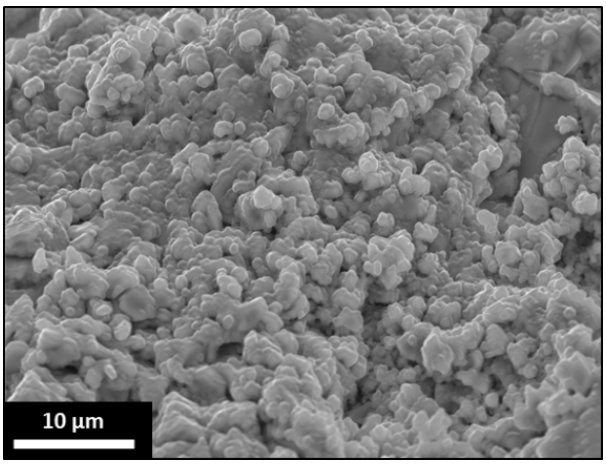

(a)

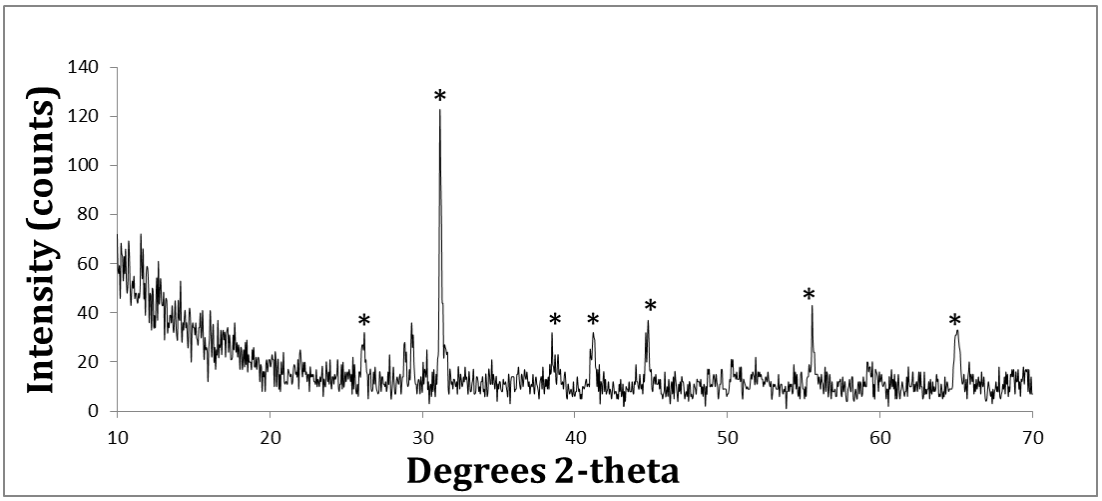

(b)

Figure 4.19: (a) SEM image of the broken pellet of C doped $BaTiO_3$ and (b) XRD of the C-doped $BaTiO_3$, where * - hexagonal $BaTiO_3$.

Since C is a reducing agent in the many oxide reducing reactions recently reviewed in [94], the so-called carbothermic reactions reduce the grain and particle sizes to the micro or even nanometer level in many instances, then enables development of devices based on nanoscience and nanotechnology. The stoichiometry of the starting materials and strict atmospheric control is a fundamental requirement for obtaining single phase, reduced oxides in this type of chemical reaction. It is possible to use a variety of carbon sources such as graphite, carbon black or carbon nanotubes but based the literature review, no global analysis of the efficiency of using different sources has yet been undertaken. It is possible that the carbothermic reduction

mentioned above did take place when processing $BaO-TiO_2$ powders, but since the hexagonal polymorph of $BaTiO_3$ is oxygen deficient, and many $BaTi^{IV}_{1-x}Ti^{III}_{x}O_{3-x/2}$ ($0<x<0.30$) powders with varied stoichiometry were reported previously in [95], it is highly likely that such a reduction took place here as well. However, a double effect in the EDAMM processing was thought to occur in this experiment because; (1) adding carbon to the starting powder reduces the Ti^{IV} ions to Ti^{III}, and bonds with the "excess" oxygen atoms leading to a hexagonal type of $BaTiO_3$ and CO/CO_2, (2) BaO and TiO_2 undergo reduction in the first place, which results in nonsoichiometric BaO_{1-x} and possibly Ti_2O_3, Ti_xO_y or TiO_xC_y [96] from which an oxygen deficient hexagonal type of $BaTiO_3$ is formed.

4.4. Phase formation sequence for TaC_Ar samples

In this research an influence of TaC coating on EDAMM processed BaO-TiO2 starting powders in Ar atmospheres was studied (Fig. 4.20). It was found that the first stage of processing, where only a few seconds of high energy discharge pulses are applied to the starting powders the desorption of water particles from BaO occurs (eq 1.1), and although water evaporates at 100°C, the water particles that are absorbed on the surface of BaO can withstand much higher temperatures. This is an important fact because as suggested previously, water molecules can affect the final phase composition of synthesized materials [97]. Moreover, TiO_2 anatase transforms irreversibly into TiO_2 rutile and depending on the particle size, preparation conditions and atmosphere can occur anywhere between 600-1200°C. In a comprehensive review [39], the authors state that inert or reducing atmospheres can result in increased amounts of oxygen vacancies in the crystal structure which then results in a faster transformation towards rutile. Additionally, further studies into the effect that the atmosphere has on the transformation temperature, revealed that transition metals also promote the formation of rutile above 700°C [98, 99]. Since those oxygen vacancies can also be created by the reducing character of C in TaC coating, this result

suggests that the efficiency of TiO_2 anatase → rutile transformation is very high (eq.1.2).

An oxygen deficient TiO_2 rutile structure and BaO and BaO1-x under highly localised DC discharges are then forming an orthorhombic type of $BaTiO_3$ (eq.1.3). It was proven in the following chapter that these types of crystallites formed particles of ~1 μm in diameter, which proves that EDAMM processing is a unique tool for obtaining phases which cannot be seen in traditional processing methods and therefore should be investigated further. It was observed in [90], that ferroelectric nanoparticles provide dielectric properties that are good for detectors or thermal imaging.

<u>First few seconds</u>

$$Ba(OH)_2 \bullet xH_2O \xrightarrow{S.S+TaC} BaO_{1-x} + BaO + H_2O \uparrow \quad (1.1)$$

$$TiO_{2(A)} \xrightarrow{S.S+TaC} TiO_{2(R)} \quad (1.2)$$

<u>1 minute of EDAMM</u>

$$BaO + BaO_{1-x} + TiO_{2(R)} \xrightarrow{S.S+TaC} BaTiO_{3(O)} \quad (1.3)$$

<u>2 minutes of EDAMM</u>

$$TiO_{2(R)} + BaTiO_{3(O)} \xrightarrow{S.S+TaC} BaTiO_{3(C)} + Ba_2Ti_6O_{13} \quad (1.4)$$

<u>4 minutes of EDAMM</u>

Grain growth of $BaTiO_{3(C)}$

Figure 4.20: Proposed phase formation sequence for the TaC, where A-anatase, R-rutile, O-orthorhombic $BaTiO_3$, C- cubic $BaTiO_3$

Orthorhombic transformation to a cubic polymorph upon heating normally occurs through another ferroelectric phase – tetragonal $BaTiO_3$, after which tetragonal distortion is realised by the displacement of Ti^{3+} in the crystal to give it ferroelectric properties [100]. During EDAMM processing however, transformation leads to

transformation into a cubic polymorph without the tetragonal crystal distortion (eq. 1.3). This sequence is once again thought to be due to highly localised discharges which make the transformations much more efficient; because this type of transformation is displacive it can occur almost instantaneously. Simultaneously to cubic $BaTiO_3$ formation, $Ba_2Ti_6O_{13}$ secondary phase was identified which most likely occurs due to the Ti-rich regions and local non-stoichiometry in the powders.

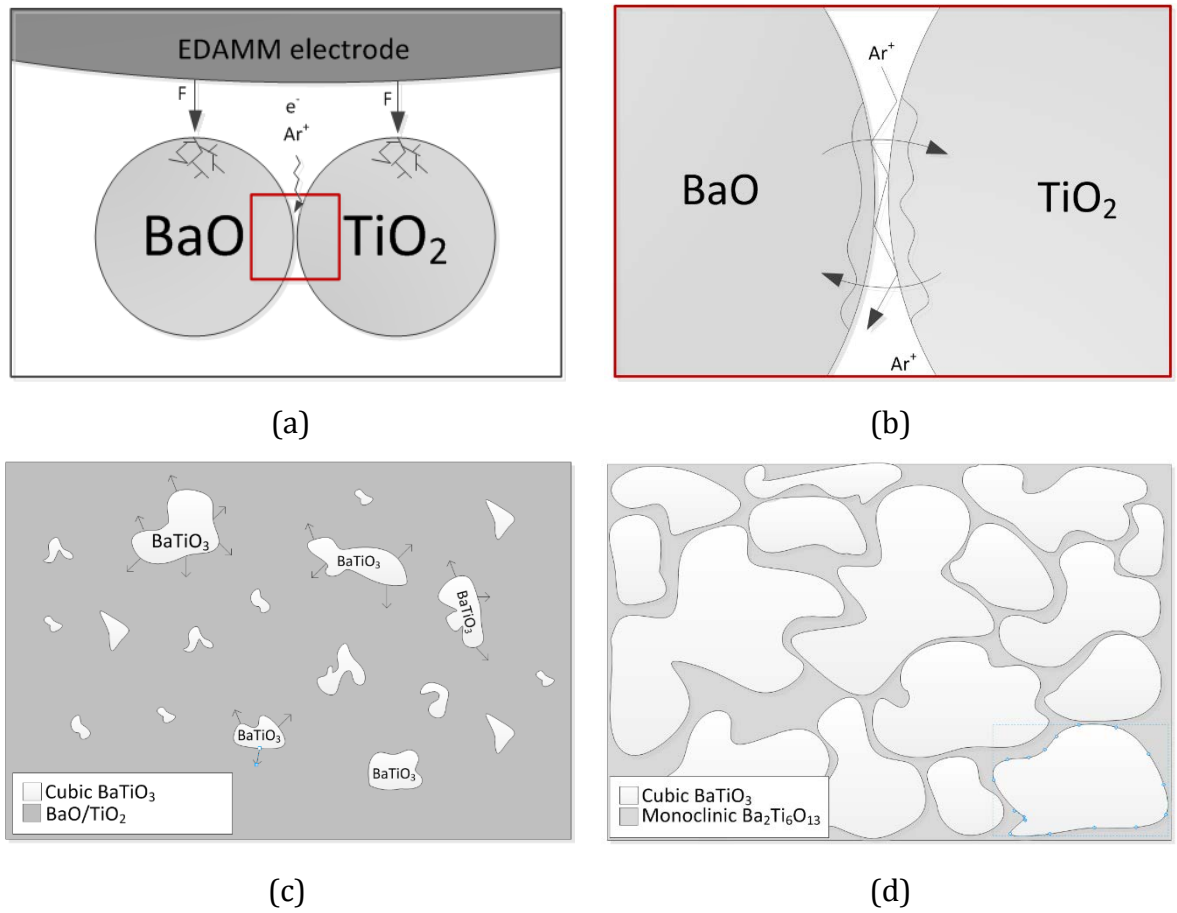

Figure 4.21 Cubic $BaTiO_3$ grain growth model in EDAMM processed powders. (a) starting powders in EDAMM environment with (b) an inset of fast, short-distance diffusion in activated powders, (c) nucleation od cubic $BaTiO_3$ grains and initial grain growth and (d) final microstructure of sample containing exclusively cubic $BaTiO_3$.

In terms of the microstructure change due to the processing discussed above, a cubic $BaTiO_3$ grain growth model observed in the TaC_Ar sample is presented in the Figure

4. 21. During the EDAMM processing where Ar ions and electrons are charge carriers, their impact on the processed powders was modified by introducing of the TaC coating on the ball electrode. This resulted in the cubic $BaTiO_3$ grain nucleation from the BaO-TiO2 starting powder. The grains were initially observed to be randomly distributed in the $Ba_xTi_yO_z$ matrix where x,y,z were varying significantly depending on the analysed region. Further processing resulted in the cubic $BaTiO_3$ grain growth which comprised majority of the observed particles with a small amount of $Ba_2Ti_6O_{13}$ secondary phase.

4.5 Phase formation sequence for O_2/Ar samples

While EDAMM processing $BaO - TiO_2$ starting powders in O_2/Ar atmosphere, a high temperature hexagonal $BaTiO_3$was synthetised. Although similar to the TaC_Ar samples, the first step in processing involved the desorption of water particles from BaO powder and the transformation of TiO_2 anatase to rutile; further processing reveals a different scheme (Fig. 4.21).

<u>First few seconds</u>

$$Ba(OH)_2 \xrightarrow{S.S} BaO_{1-x} + BaO + H_2O \uparrow \quad (2.1)$$

$$TiO_{2(A)} \xrightarrow{S.S} TiO_{2(R)} \quad (2.2)$$

<u>1 minute of EDAMM</u>

$$BaO + BaO_{1-x} + TiO_{2(R)} \xrightarrow{S.S} BaTiO_{3(C)} + BaTiO_{3(H)} \quad (2.3)$$

<u>2 minutes of EDAMM</u>

$$TiO_{2(R)} + BaTiO_{(C)} \xrightarrow{S.S} BaTiO_{(H)} + Ba_2Ti_6O_{13} \quad (2.4)$$

<u>4 minutes of EDAMM</u>

Grain growth of $BaTiO_{3(H)}$

Figure 4.22: Proposed phase formation sequence for O_2/Ar where A-anatase, R-rutile, H-hexagonal $BaTiO_3$, C- cubic $BaTiO_3$.

Here, the final crystal structure of hexagonal $BaTiO_3$was preceded by cubic rather than orthorhombic crystallites. Based on an XRD investigation it appears that further processing during the first minute results in the formation of both cubic and hexagonal crystal structures. However, a cubic crystal structure is the first one formed after heating between 120-1430°C, so we propose that the mechanism whereby hexagonal $BaTiO_3$ is formed in EDAMM always involves an intermediate step with cubic crystals. This conclusion is also based on the facts presented in the section with O_2/Ar samples where we indicated that the processing conditions involve a gradual increase of electrical conditions in order to minimise the amount of contamination and secondary phases, and to maximise the amount of hexagonal $BaTiO_3$. Because of the fact that cubic → hexagonal $BaTiO_3$ transformation is of the martensitic type, it happens extremely fast often described as occurring at the speed of sound. We believe that EDAMM discharges which enable microsecond pulses supply enough energy to enable the transformation of the materials which are usually lengthy in preparation and, on the other hand, utilise this energy for short periods of time to prevent them from melting. This might also suggest that the short time in which the discharge is acting on the particle prevents excessive grain growth.

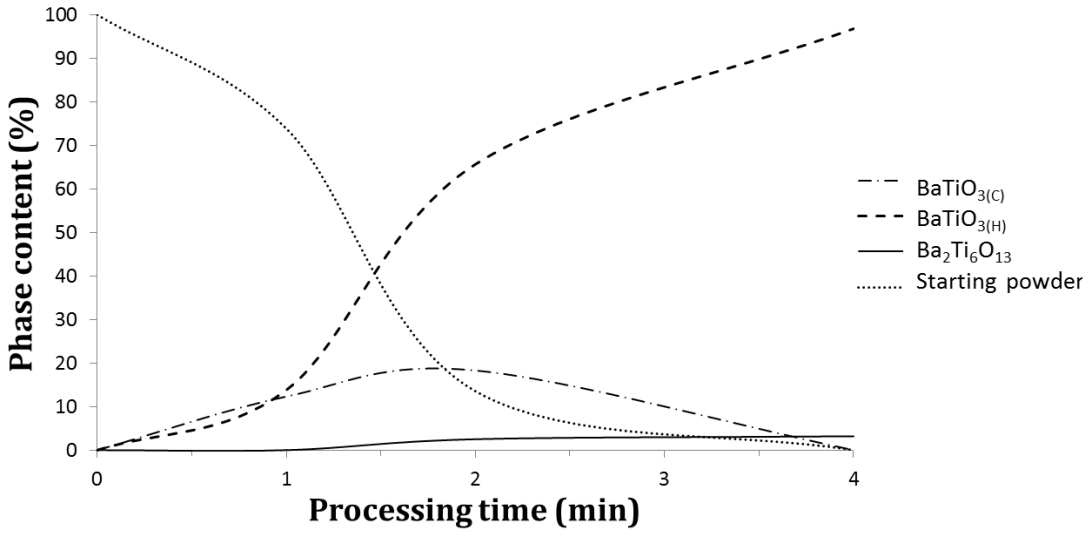

Figure 4.23: Phases content in the EDAMM processed O_2/Ar samples.

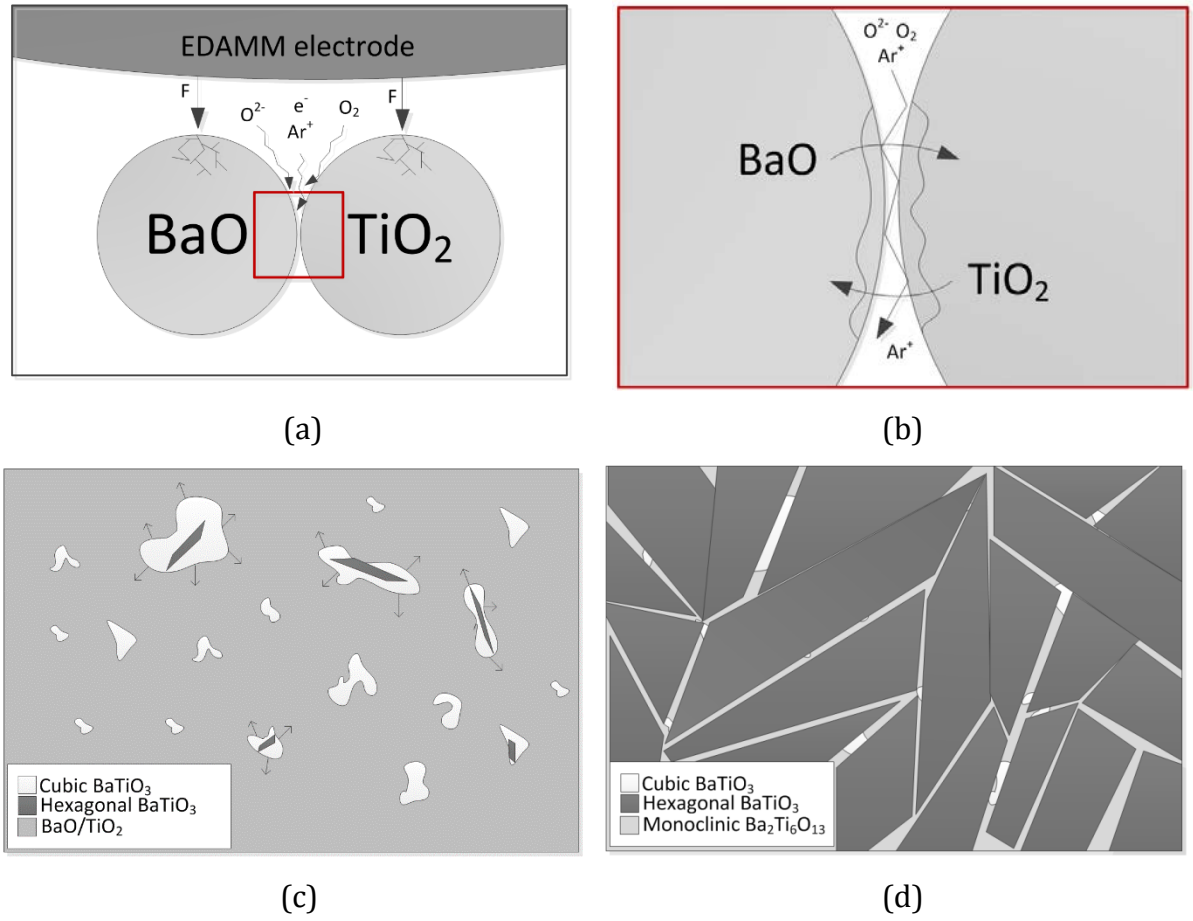

Figure 4. 24 Hexagonal $BaTiO_3$ grain growth model in EDAMM processed powders. (a) Starting powders in EDAMM environment with (b) an inset of fast, short-distance diffusion in activated powders, (c) nucleation od cubic $BaTiO_3$ grains and start of the cubic-hexagonal phase transformation and (d) final microstructure of hexagonal $BaTiO_3$ grains with retained cubic grains.

Change in the microstructure during the EDAMM processing observed in the O_2/Ar samples (Fig. 4.22) are significantly different in comparison to the TaC_Ar samples. The initial stages of the processing included BaO-TiO_2 starting powders being affected by the plasma where apart from electrons and Ar ions an additional factor played O_2 molecules. The latter, being di-atomic molecules, have higher energy than Ar ions and increased the temperature of the processing, resulting in simultaneous low temperature stable cubic $BaTiO_3$, but also high temperature stable hexagonal

polymorph. This fact is also elucidated on the Figure 4.23, where the data was obtained from the X-ray diffraction analysis of the peaks corresponding to the starting material and cubic, hexagonal and monoclinic phases. After 1 and 2 min of processing the amount of cubic $BaTiO_3$ is making up even 20% of the materials phase content but later in the process it decreases and the hexagonal phase's content dramatically increases. This is also illustrated on the Figure 4. 23. The final microstructure consists of hexagonal platelet-like $BaTiO_3$ grains, $Ba_2Ti_6O_{13}$ secondary and retained cubic $BaTiO_3$ grains.

4.6 Conclusions

In the above chapter BaO-TiO_2 starting powders were processed in EDAMM in two optimized conditions; (i) by applying the TaC on the stainless steel electrode and (ii) by processing in 10%O_2/Ar instead of pure Ar gas.

Phase transformations induced by EDAMM were studied in detail. The cubic-hexagonal phase transformation in synthesized $BaTiO_3$ was used to help further interpret what occurs during EDAMM processing. It was found that use of the TaC coating applied on the electrode reduces the overall temperature of the processing, as evaluated on the basis of the microstructural and crystallographic analysis of products. Only the low temperature $BaTiO_3$ polymorph was formed from BaO and TiO_2 starting powders within 4 min and a nucleation and grain growth model of formation of cubic $BaTiO_3$ polymorph was derived. In the first stages of the processing powder particles are crushed and mixed within the EDAMM chamber and plasma species such as Ar^+ ions, electrons, free radicals and excited species activate the freshly formed surfaces. Fast, short-distance diffusion of the atoms and oxides takes place at the particle interfaces and migration of species occurs. This results in nanocrystalline precursors of cubic $BaTiO_3$ in a form of orthorhombic nanoparticles. In further stages of the processing orthorhombic→cubic $BaTiO_3$ transformation, nucleation and grain growth takes place. The final microstructure contains almost entirely cubic type of $BaTiO_3$, which implies that the processing temperature with TaC

coating in Ar atmosphere did not exceed the temperature characteristic for formation of hexagonal $BaTiO_3$ which, based on the phase diagram is ~1430°C (Figure 3.7).

From $BaTiO_3$ experiments performed in an O_2/Ar atmosphere it was concluded that the addition of O_2 to Ar gas increases the temperature of the processing in EDAMM. This could be inferred from the final microstructures and phases present in the representative particles processed under these conditions, where a majority phase present was the high temperature hexagonal $BaTiO_3$ polymorph. The final microstructure is attributable to the high energy O_2 based species present in plasma environment that enable heating of the powder particles to much higher temperatures, inducing an instant transformation from cubic $BaTiO_3$ to hexagonal $BaTiO_3$.

CHAPTER 5

Orientation relationship analysis of the phases in $BaO - TiO_2$ system

The objective of the following chapter is a crystallographic analysis of the phases in synthetized $BaTiO_3$ powder particles and a determination of the relationships between the phases present. Two complimentary methods were used to determine the orientation relationships (ORs) between the phases present so that phase formation and evolution during EDAMM could be assessed, and the data presented in Chapter 5 complemented. These methods were as follows: (i) determining the local orientation relationships between adjacent phases using the classical method of transmission electron microscopy (TEM) with selected area electron diffraction (SAD), and (ii) a statistical analysis of orientation relationships over a large area using electron back-scattering diffraction (EBSD) combined with a new, advanced computational method. The latter is a major advancement in the field of EBSD analysis that has never been presented before; it makes it possible to analyse the interphase grain boundaries globally and then extrapolate the data to enable the formation and transformation mechanisms in the studied materials to be determined.

As shown previously, X-ray diffraction shows the development of cubic or hexagonal $BaTiO_3$ as the predominant phase in EDAMM processed TaC_Ar or O_2/Ar samples. In both processing regimes the secondary phase was monoclinic $Ba_2Ti_6O_{13}$, so the following paragraphs are any analysis of the orientation relationship of three classes of interphase boundaries, namely; cubic-hexagonal, cubic-monoclinic, and hexagonal-monoclinic.

5.1 Phase transformations and expected orientation relationships in $BaO - TiO_2$ system

Solid state transformations have been studied widely since the 20th century so their definitions are based on experimental data and thermodynamic considerations, but regardless of how simple the process of phase transformation may seem, it involves a mechanism that is typical for a certain group of materials but not always easily categorised. Almost 200 different solid-state mechanisms are known to modern science so far with similar or common characteristics[101]. The sole fact that there

are such a great number of them imply specific classification criteria so we must be mindful that those mechanisms may depend on the method, the observation tools, and many other factors.

$BaTiO_3$ is most commonly obtained from $BaCO_3$ or BaO and TiO_2 starting powders, which is why formation mechanisms have been widely reviewed and presented in literature, especially for solid-state reactions [66, 102, 103]. As-received $BaTiO_3$, undergoes crystal structure transformations in a temperature range from -90 to ~1480°C; orthorhombic → tetragonal → cubic → hexagonal (Fig. 5.1). These transformations are then classified as martensitic because of their slight rearrangement of the atoms in the structure having a displacive, diffussionless and temperature-dependent character. They are of the particular interest for a deeper understanding of the EDAMM method presented in this thesis because they display a temperature dependent transformation accompanied by typical microstructural features; however, they are also important for industrial applications where various crystal structures display different dielectric properties[104]. The following section therefore concentrates on the relationships of the phases obtained in a crystallographic sense in order to derive more precise mechanisms of transformation in EDAMM conditions.

Orientation relationship analyses are traditionally undertaken using selected-area electron diffraction at an interphase boundary in a transmission electron microscope. In case of $BaTiO_3$, the orientation relationship between tetragonal (t, also referred to as pseudo-cubic) and hexagonal (h) $BaTiO_3$ was first predicted in Ref. [105] on the basis of theoretical crystallographic considerations; the coalescence of octahedral faces in cubic crystals $\{111\}_t$ on hexagonal basal face -$(0001)_h$. Following this, Wu et al. [106] used transmission electron microscopy and selected-area diffraction to further determine multiple orientation relationships and then showed them on superimposed $(111)_t$ and $(0001)_h$ pole figures. Furthermore, Zheng at al. [107] determined the orientation relationship between the tetragonal $BaTiO_3$ and equilibrium monoclinic (m) $Ba_6Ti_{17}O_{40}$ phases as $(1\bar{1}\bar{1})_t$ || $(001)_m$ and $(1\bar{1}2)_t$ ||

$(60\bar{2})_m$ and $[110]_t$ || $[0\bar{1}0]_m$. This was subsequently re-confirmed by Burbure et al. [108] as $(111)_t$ || $(001)_m$ and $[\bar{1}01]_t$ || $[010]_m$. In the former study, the samples were prepared by sintering in air at 1200°C and 1300°C for extended periods of time; this resulted in exaggerated grain growth (~200 μm) of the tetragonal $BaTiO_3$ grains and thin, plate-shaped $Ba_6Ti_{17}O_{40}$ grains located at tetragonal $BaTiO_3$ triple junctions. Since the sintering temperatures were below the eutectic point, the secondary monoclinic $Ba_6Ti_{17}O_{40}$ phase was said to have formed as a result of solid rather than liquid -state sintering. Interestingly, there is no data available in open literature on the orientation relationship between the cubic $BaTiO_3$ and monoclinic $Ba_2Ti_6O_{13}$ phases. The latter intermediate phase is fairly uncommon and is only believed to form in highly reducing atmospheres and relatively high temperatures (Fig. 5.1)[47]. It should be noted that the monoclinic $Ba_2Ti_6O_{13}$ phase contains both Ti^{3+} and Ti^{4+} ions, which is typical of reducing atmospheres, and it was formed during EDAMM in Ar or 10% O_2/Ar atmospheres.

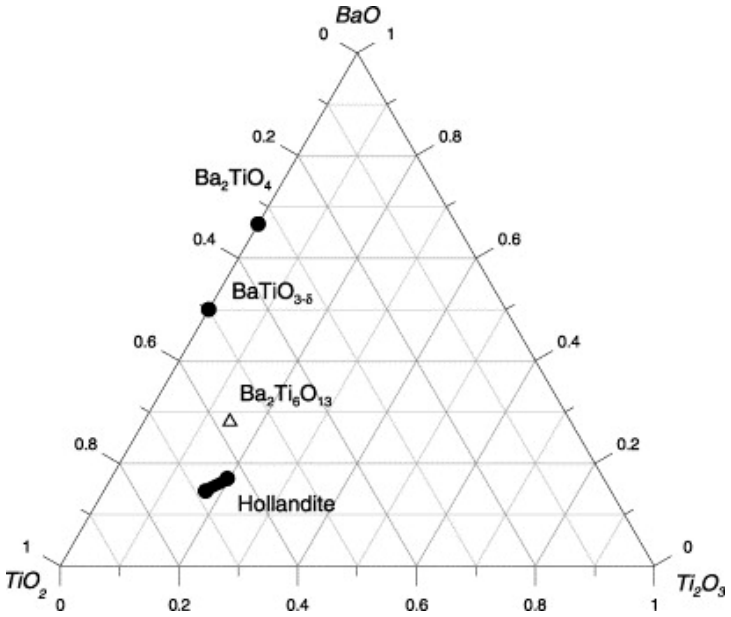

Figure 5.1: BaO-TiO_2-Ti_2O_3 ternary phase diagram under reducing conditions at temperatures over 1300°C [47].

5.2 Results

5.2.1 Orientation relationships via selected area electron diffraction

Cubic-hexagonal interphase boundaries

The orientation relationship analysis involving cubic and hexagonal grains was carried out on lamella prepared from powder particles from the TaC_Ar group of $BaTiO_3$ samples. The area of the lamella lift-out was decided upon the initial EBSD mapping where the distinction between chemically equivalent phases was made based on crystallographic information obtained from previous XRD analysis (section 4.1). For more information on the sample preparation conditions and classification see Table 4.1.

The interphase boundary between cubic and hexagonal grains is shown on the bright field image in Figure 5.2a. The size of the hexagonal grain is significantly smaller than the cubic one which is a typical microstructural feature observed in TaC_Ar samples. Selected area diffraction performed on the cubic $BaTiO_3$ grain was done along the $[111]_c$ zone axis and paralellism of hexagonal $[0001]_h$ direction was found (Fig. 5.2b) and c. The selected-area images are deliberately shown as separate as some of the diffraction spots of the cubic and hexagonal phases are directly superimpose on each other, thereby making it impossible to differentiate between the two phases in a single image. The weaker spots in Fig. 5.2c are attributed to double reflections. Indexing the diffraction patterns in Fig. 5.2b and c reveals that the cubic-hexagonal phases have the following orientation relationship: $(111)_c$ || $(0001)_h$ and $[1\bar{1}0]_c$ || $[11\bar{2}0]_h$; this is further confirmed by the diffraction simulations shown in Figure 5.2d and e. There is little evidence in the literature on the orientation relationships between cubic and hexagonal $BaTiO_3$, however, current result agrees with a report in the literature for this type of parallelism between pseudo cubic barium titanate [106]. The parallelism in planes and directions also conforms to the well-known Shoji-Nishiyama (S-N) orientation relationship previously characterised for fcc austenite

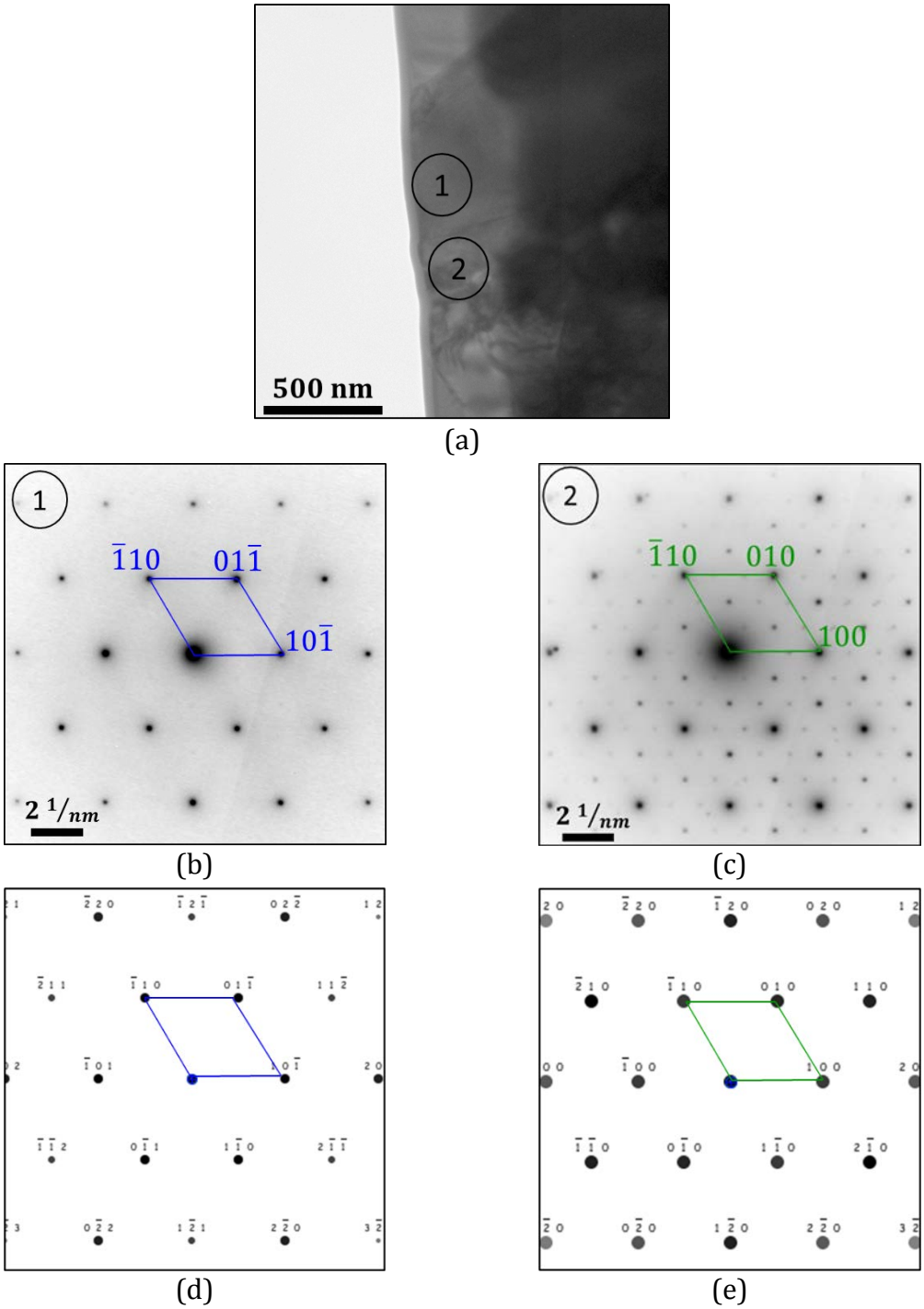

Figure 5.2: (a) Bright-field image of the cubic-hexagonal interphase boundary, selected-area electron diffraction of the (b) cubic grain along the $[111]_c$ zone axis, and (c) hexagonal grain along the $[0001]_h$ zone axis, and (d,e) equivalent diffraction simulations.

and hcp ε-martensite phases of high Mn transformation-induced plasticity steels [109] and the fcc TiAl γ-matrix and hcp Ti_3 Al α_2-precipitates in γ-based Ti-Al alloys [110-112] .

Cubic-monoclinic interphase boundaries

The orientation relationship analysis involving cubic and monoclinic grains was carried out on lamella prepared from powder particles from the TaC_Ar group of $BaTiO_3$ samples, while the lift-out area was determined by previous EBSD mapping. For more information on the sample preparation conditions and classification see Table 4.1.

There is no evidence in the literature of this OR being found for the cubic $BaTiO_3$ and monoclinic $Ba_2Ti_6O_{13}$ phases, however, an orientation relationship between the bcc (t) martensite matrix and the Ni-containing monoclinic precipitates in an 21 wt.% cobalt iron alloy was observed before on following zone axis: $[120]_\alpha$ || $[001]_m$[109].

Distinct grain boundary interphase between the cubic and monoclinic ($Ba_2Ti_6O_{13}$) phases can be observed in the bright-field image in Figure 5.3a, which is notable due to the chemical compositions between phases. Selected area diffraction on the cubic $BaTiO_3$ grain was carried out along the $[001]_c$ zone axis and a parallelism in the monoclinic $[0\bar{1}0]_m$ direction was found (Fig. 5.3b). In order to re-confirm the orientation relationship in cubic-monoclinic interphase boundary, the beam was tilted to reach the [002]c zone axis which caused distortion (elipticity) in the diffraction pattern; this distortion was corrected using the "Ellipse Fitting Analysis" script from the website [31]. Diffraction patterns were then taken at $(002)_c$ || $(0\bar{2}0)_m$. Finally, indexing the diffraction pattern based on the available crystallographic data and diffraction simulation (Fig. 5.3c) reveals that the cubic-monoclinic phases shares the following orientation relationship: $(002)_c$ || $(0\bar{2}0)_m$ and $[120]_c$ || $[001]_m$.

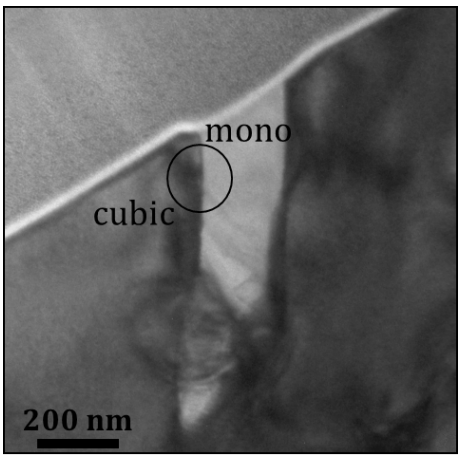

(a)

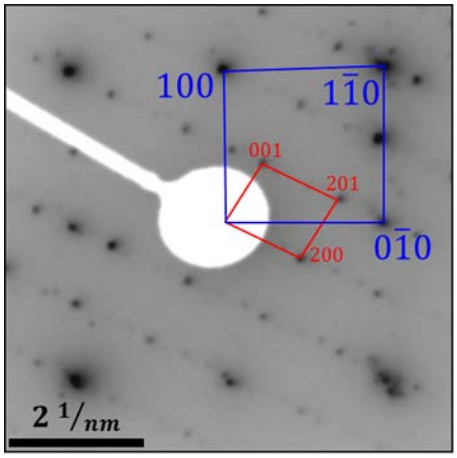

(b)

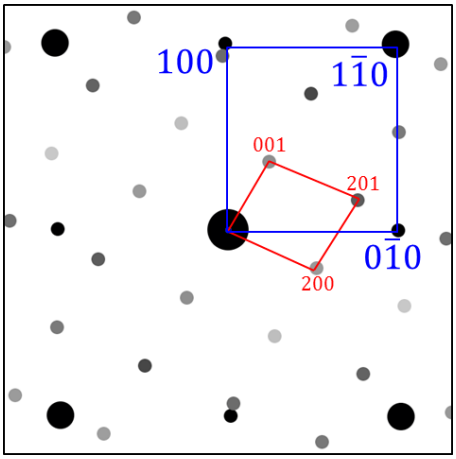

(c)

Figure 5.3: (a) Bright-field image of the cubic-monoclinic interphase boundary, (b) selected-area electron diffraction of the cubic grain along the$[001]_c$ zone axis and the monoclinic grain along the $[0\bar{1}0]_m$ zone axis, and (c) the equivalent diffraction simulation.

Hexagonal-monoclinic interphase boundaries

An orientation relationship analysis involving cubic and monoclinic grains was carried out on lamella prepared from powder particles from the Ar group of $BaTiO_3$ samples. Similarly to the previous electron diffraction analysis, the lift-out area was determined by previous EBSD mapping. With this particular interphase boundary, finding the orientation relationship proved much more difficult than the other two examples because of the lack of symmetry of monoclinic crystal structure and low symmetry of

hexagonal crystals. For more information on the sample preparation conditions and classification see Table 4.1

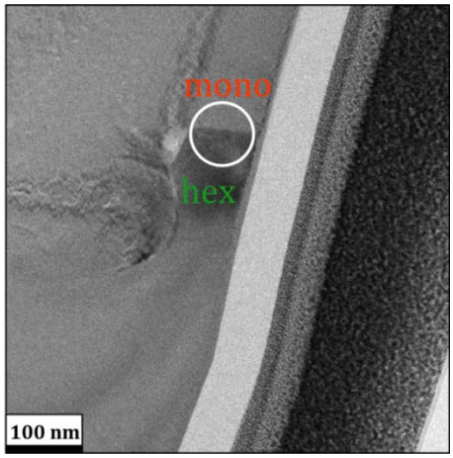

(a)

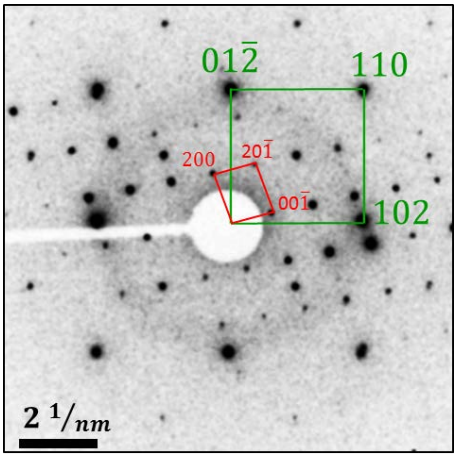

(b)

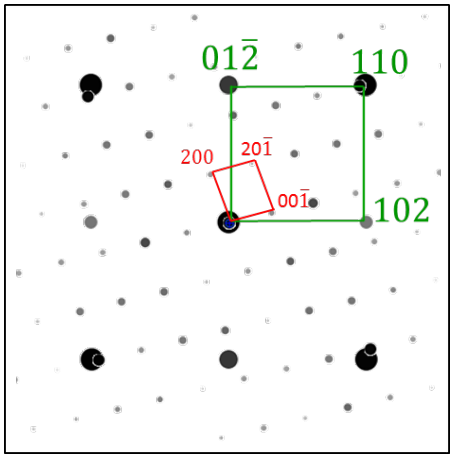

(c)

Figure 5.4: (a) Bright-field image of the hexagonal-monoclinic interphase boundary, and (b) selected-area electron diffraction of the hexagonal grain along the $[\bar{2}201]_h$ zone axis and monoclinic grain along the $[010]_m$ zone axis axis, and (c) the equivalent diffraction simulation.

Cubic and hexagonal $BaTiO_3$, having the same chemical composition, do not display a distinct interphase grain boundary, as seen in the bright field image in Fig. 5.4a. Selected area electron diffraction of the interphase boundary, where hexagonal grain was tilted to the $[\bar{2}201]_h$ zone axis revealed that the $[010]_m$ zone axis of the

monoclinic grain display parallelism and the diffraction spots of both directions can be indexed, as shown in Fig. 5.4b. Indexing of the diffraction pattern and confirmation by the diffraction simulation (Fig. 5.4c) shows that the hexagonal-monoclinic phases shared a new and previously unknown orientation relationship between them with: $(10\bar{1}2)_h$ || $(\bar{2}02)_m$ and $[\bar{2}201]_h$ || $[010]_m$.

The result obtained in the above sections, especially the cubic- monoclinic and hexagonal-monoclinic interphase boundary orientation relationships present a significant advancement in the knowledge of $Ba_2Ti_6O_{13}$ phase correlation with the well-known cubic and hexagonal $BaTiO_3$ phases. As presented in the Fig. 4.9, where the indexing of the secondary, monoclinic $Ba_2Ti_6O_{13}$ was shown, and based on the literature information, the phase is exclusively found in the high pressure and temperature systems. Here, its presence and orientation relationship with the cubic and hexagonal $BaTiO_3$ phases was undoubtedly confirmed. The implications from the results for the EDAMM processing technique are substantial because the results prove that the method can form unusual and possibly metastable phases. The sole presence of this phase indicates that extreme stresses may be implied on the processed particles which, with a high temperature, results in the nucleation and growth of the phases which cannot be formed in equilibrium conditions.

5.2.2 Orientation relationships via electron back-scattering diffraction

Electron back-scattering diffraction principles

Within an EBSD map, each pixel contains phase and orientation information based on a user-specified macroscopic co-ordinate system, and this orientation relationship across an interphase boundary segment can be described using the angle-axis representation. As per Euler's theorem, and given a fixed macroscopic reference frame, grain orientation can be defined by a set of three angles(ϕ_1, Φ, ϕ_2). It follows that misorientation is the angular difference in crystallographic orientation between any two grains within a polycrystalline aggregate. Alternatively, misorientation between any two grains of the same phase/crystal system can also be defined as the rotation angle (θ) around a common rotation axis [uvw] needed to bring the crystal co-ordinate systems into coincidence.

In keeping with the above definition and in the case of interphase boundary segments, the misorientation angle between any two phases can be calculated and the rotation axes defined in terms of the individual phases/crystal systems. Therefore, although two rotation axes are used to define an interphase boundary segment, the unit cells of both phases/crystal systems share a common, pre-defined macroscopic co-ordinate system. It follows that an orientation relationship across an interphase boundary segment is defined by a certain misorientation angle and a set of two unique rotation axes. When two phases share an orientation relationship, a histogram plot of their misorientation angles contains a peak at a particular value. Within a reasonable deviation from the particular misorientation angle value comprising the peak in the histogram plot, a unique rotation axes of the two phases/crystal systems also recurs. Therefore the interphase boundaries can be statistically quantified in the above manner.

Since selected-area electron diffraction provides the orientation relationship between the adjacent phases, it can be used in conjunction with the relationship between the abovementioned rotation axes to determine the misorientation angle distribution of the ideal orientation relationship in the whole analysed EBSD large area map. This orientation relationship deviation is expected to occur in materials processed under non-equilibrium conditions due to external stresses during the processing. Such behavior was previously observed in Kurdjumov-Sachs (K-S) orientation relationship type in ferrite-austenite interphase boundaries where 0-5° misorientation angle deviation was reported for unstressed samples, and even 5-10° with applied external stresses [113]. It was concluded that the orientation relationship between ferrite and austenite is weakened by the applied external stress and therefore it can serve as an indicator of the processing conditions. Consequently, EDAMM processed BaO and TiO_2 and the transformation of resultant phases where such deviations in the orientation relationship may occur is paramount in deepening our understanding of this processing.

Electron back-scattering diffraction post-processing technique

---

A specialised code was developed within Matlab using the MTex toolbox (Azdiar A. Gazder, UOW) to return the misorientation angle distribution and rotation axes in the reference frames of the two phases/crystal systems across interphase boundary segments for a given EBSD map. It should be noted that the method presented in this chapter is new in its entity and has not been reported before for the orientation relationships analysis of two crystallographically different phases. The only resemblance of the method presented is the one used for the analysis of twins, where the orientation between the same types of crystal structures is known[114]. In this case however, information about the crystal symmetry, angle–axis pairs, and quantification based only on the same crystal type is used. Such an approach was used in the twin boundaries in steels [115] and magnesium alloys [116-118] a unified approach for multi-phase analysis in the form presented in this chapter has not been presented in the literature yet.

Since the orientation relationship between two phases/crystal systems (determined previously by the transmission electron diffraction) is defined by a set of parallel planes and directions, the pole figures are representations of these planes and the directions can therefore be computed. As a result, the pole figure of the specific crystal type with a given orientation can be superimposed on the pole figure of the adjacent crystal and evaluated in terms of the overlap. The overlapping diffraction spots displayed on as-generated pole figures assign the interphase boundary as non-OR boundary or an OR boundary with the deviation from an ideal relationship as a misorientation plot.

Consequently, all grain boundaries are assigned as either non-OR boundaries, such as low angle intraphase boundaries (LABs) or high angle interphase boundaries (HABs), amongst which the differentiation between OR compliant and non-compliant boundaries is made. Such an approach carried out for the whole EBSD map allows for a statistical analysis of all the boundaries and therefore aids in understanding the mechanism of transformation of all the material studied. In the following section, EBSD maps of TaC_Ar and O_2/Ar samples are analysed with the aid of the previously obtained orientation relationships between the three phases, namely; cubic-hexagonal, cubic-monoclinic, and hexagonal-monoclinic (Fig. 5.5). A detailed quantification of the phase fractions is shown in Table 5.1 where zero solutions are the blank pixels which did not conform to any of the phases.

Table 5.1: Phase fractions in the TaC_Ar atmosphere and a mixture of O_2/Ar samples.

Sample type	**Zero solutions**	**Phase fractions**		
		Monoclinic	**Cubic**	**Hexagonal**
TaC_Ar	0.2	7.8	91.5	0.5
O_2/Ar	1.1	7.3	2.4	89.2

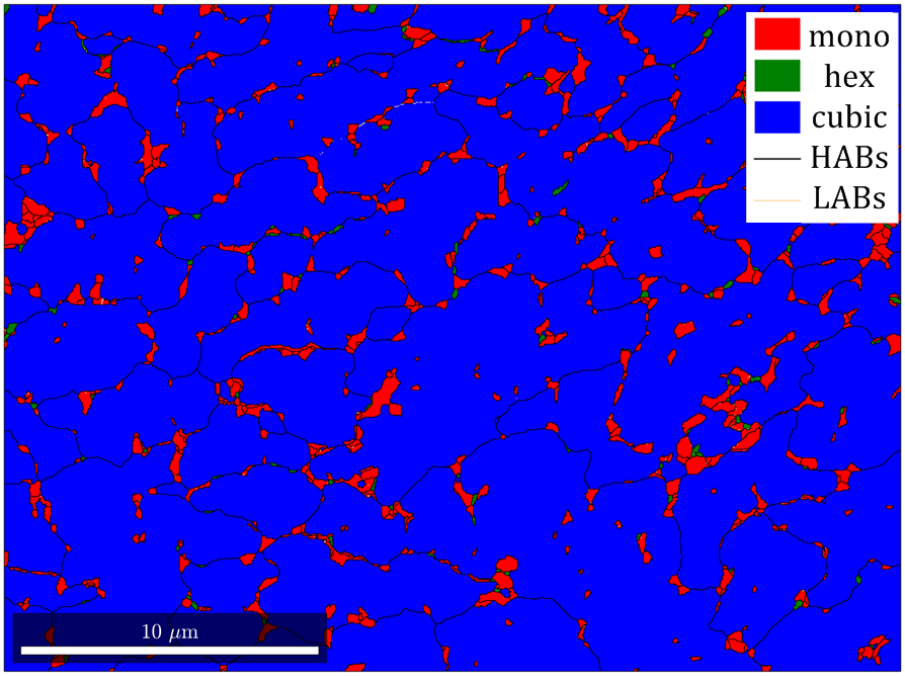

(a)

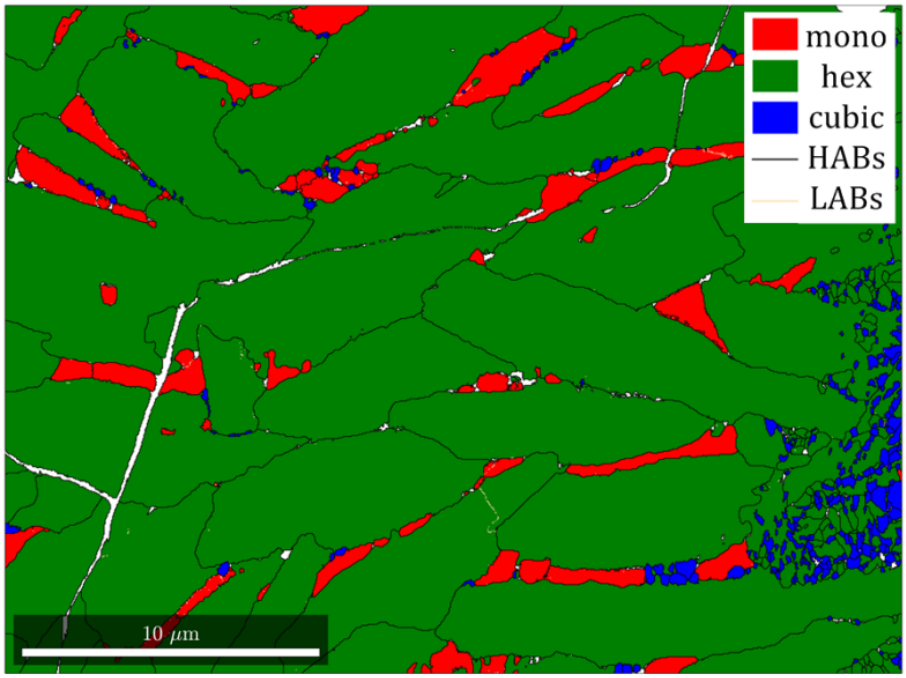

(b)

Figure 5.5: Representative phase maps of the EDAMM processed (a) TaC_Ar samples and (b) O_2/Ar samples. Legend: red = monoclinic $Ba_2Ti_6O_{13}$, green = hexagonal $BaTiO_3$, blue = cubic $BaTiO_3$, white = zero solutions, black = high-angle grain boundaries (HABs) and yellow = low-angle grain boundaries (LABs).

EBSD mapping together with the specialised computational method was then used to obtain intraphase and interphase boundaries fractions. The results of the quantification are listed in the Table 5.2 and Table 5.3.

Cubic-monoclinic interphase boundaries in TaC_Ar sample comprise over 58% of all grain boundaries visible on the map, with very low unindexed fraction (zero solutions) (Table 5.2). Because e such a large number of interphases available it is a good candidate for statistical analysis and will be used later on for the computational method analysis for cubic-monoclinic interphase.

Table 5.2: Intraphase and interphase boundary population (in percent) for the TaC_Ar sample.

	Zero solutions (intraphase)	**Monoclinic**	**Cubic**	**Hexagonal**
Monoclinic	0.6	8.3	58.2	2.6
Cubic	6.9		17.8	5.4
Hexagonal	0.1			0.1

Table 5.3: Intraphase and interphase boundary population (in percent) for the O_2/Ar samples.

	Zero solutions (intraphase)	**Monoclinic**	**Cubic**	**Hexagonal**
Monoclinic	5.2	0.9	1.8	20.6
Cubic	1.6		2.2	20
Hexagonal	23			24.7

On the other hand, the microstructure and EBSD intraphase and interphase quantification in the O_2/Ar samples map shows much higher amounts of the cubic-hexagonal and hexagonal-monoclinic interphases, comprising 20 and 24.7% of the whole grain boundary population, respectively (Table 5.3). In this case the map

provides a sufficient amount of the interphase data for a statistical analysis of the above mentioned interphases.

In this regard, representative examples of orientation relationship analyses are presented on the EBSD maps with the biggest percentage of interphase boundaries pair, such that:

I. cubic-hexagonal interphase- O_2/Ar sample map,
II. cubic-monoclinic interphase- TaC_Ar sample map,
III. hexagonal-monoclinic interphase- O_2/Ar sample map.

These quantifications classify the boundaries based solely on the crystal structure type, but it does not consider the orientation relationship between the phases. In the results presented below, such a distinction is made using the advanced computational method. It should be noted that in this case, the intraphase boundary population (i.e. – the boundaries between monoclinic-monoclinic, cubic-cubic and hexagonal-hexagonal grains) are excluded from the orientation analysis calculations.

Cubic-hexagonal interphase boundaries

The following section presents an analysis of cubic-hexagonal interphase boundaries based on an EBSD map of the O_2/Ar samples of $BaTiO_3$ (Fig. 5.6a). The intraphase LABs are marked by yellow lines whereas the colour of the interphase HABs display depends on the misorientation angle based on the cubic-hexagonal orientation relationship found previously in section 5.2.1. Considering the symmetry of the cubic-hexagonal crystals pair the maximum misorientation angle falls at 56.60°[119] and here it is re-confirmed with a higher precision as 56.6003° (red line in the Fig. 5.6b). If a random distribution of grains is assumed, the misorientation distribution of uncorrelated cubic-hexagonal interphase boundaries is called a McKenzie distribution and there is a cubic-hexagonal interphase, the peak falls at 45° [120]. The cubic-hexagonal misorientation distribution plotted from the data obtained from the map in Fig. 5.6a (using 1° class intervals) does not follow the random misorientation distribution, it shows a peak at 56.6003° (the forbidden zone limit); which in turn, conforms to the theoretical misorientation angle between the cubic and hexagonal phases for the Shoji-Nishiyama (S-N) orientation relationship [109].

It was found that within the HABs, over 78.97% of the cubic-hexagonal interphase boundary population is within a ±2.5° deviation of the theoretical misorientation angle for the S-N orientation relationship (Fig. 5.7, boundaries in purple). The inset shows that individual cubic and hexagonal grains tend to share entire interphase boundary segments with each other. When the misorientation of rotation axis distributions in the cubic and hexagonal crystal co-ordinate systems are plotted (Figs. 5.7b and 5.7c), a single peak is returned for both plots that is centred around the theoretical rotation axes and conforms to the S-N orientation relationship defined as $[uvw]_c$ = $[\overline{1.6918}\ \overline{2.2047}\ 0.7007]$ or ~$[\bar{2}\ \bar{3}\ 1]$ for the cubic crystal system, and $[UVTW]$ = $[\overline{3.3787}\ \overline{2.1239}\ 5.5026\ 3.4145]$ or ~$[\bar{2}\ \bar{1}\ 3\ 2]$ or $[uvw]_h$ = $\left[\overline{8.8813}\ \overline{7.6265}\ 3.4145\right]$ or ~$[\bar{3}\ \bar{2}\ 1]$ for the hexagonal crystal system.

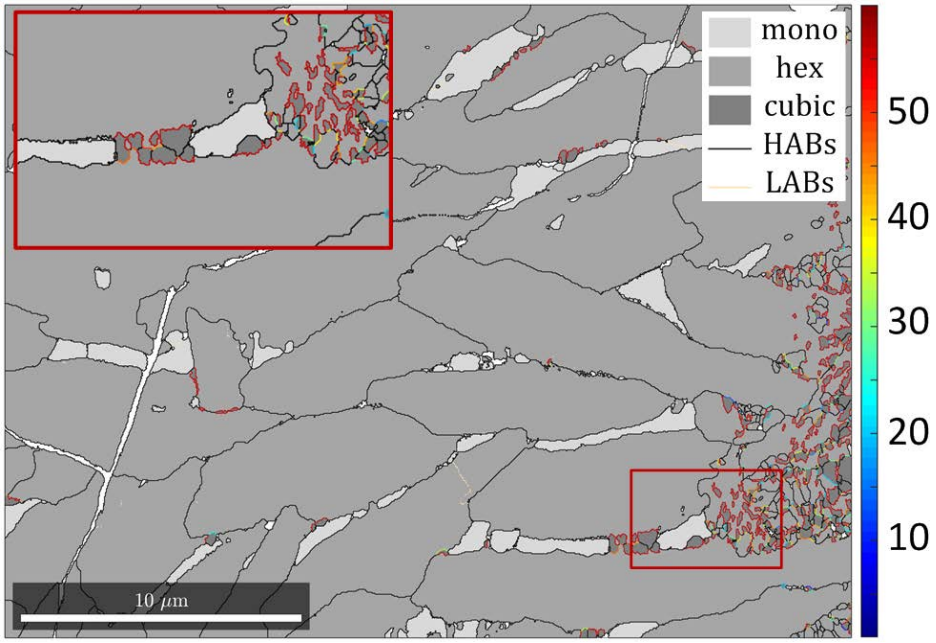

(a)

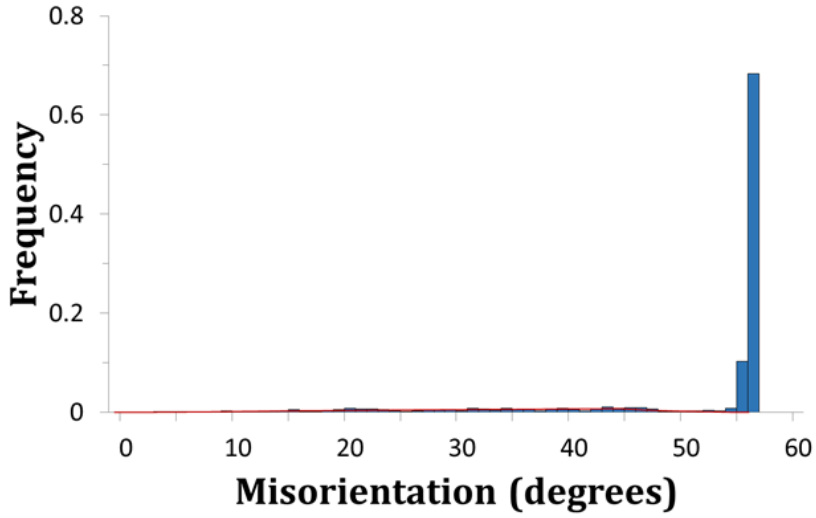

(b)

Figure 5.6: (a) Cubic-hexagonal interphase boundary misorientation map of EDAMM processed $BaTiO_3$ O_2/Ar sample, and (b) histogram of interphase misorientation distribution using 1° class intervals. Legend: (a) light grey = monoclinic $Ba_2Ti_6O_{13}$, medium grey = hexagonal $BaTiO_3$, dark grey = cubic $BaTiO_3$, white = zero solutions, black = high-angle grain boundaries (HABs) and ivory = low-angle grain boundaries (LABs).

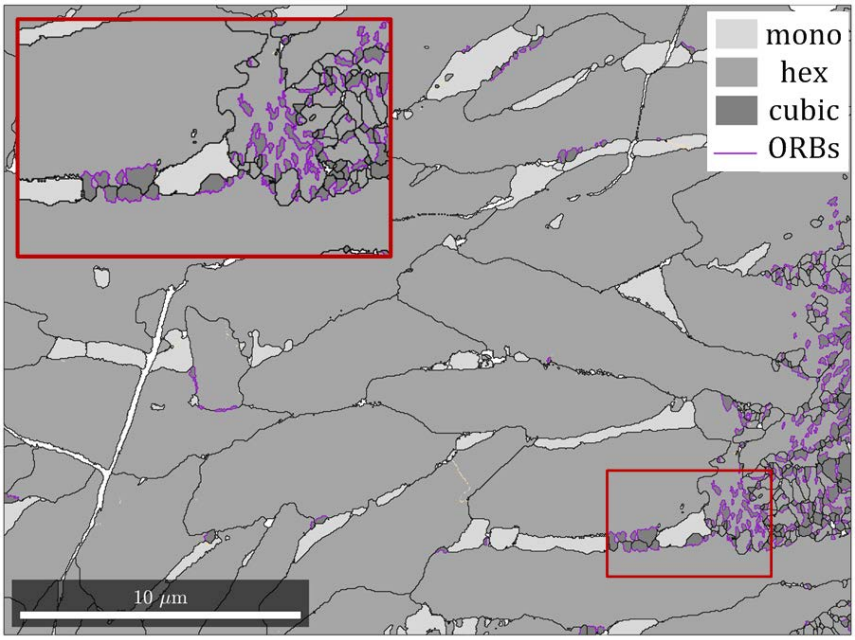

(a)

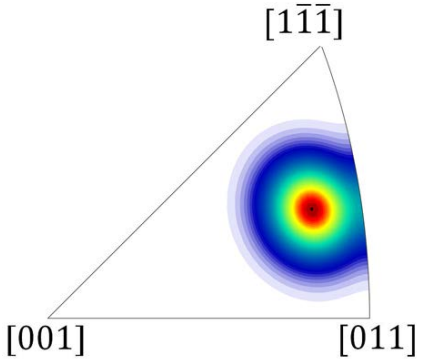

(b)

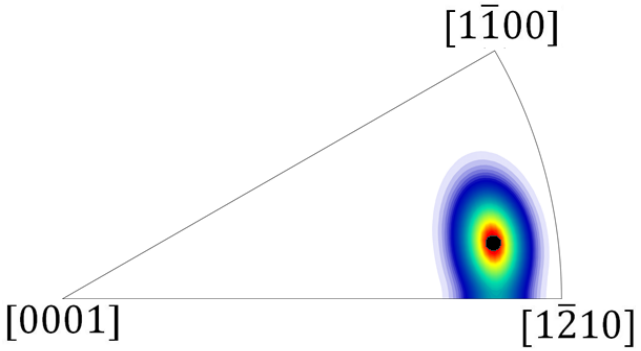

(c)

Figure 5.7: (a) The cubic-hexagonal interphase boundary population within a ±2.5° deviation of the theoretical misorientation angle for the S-N orientation relationship (in purple). Rotation axis distributions in the (b) cubic and (c) hexagonal crystal co-ordinate systems.

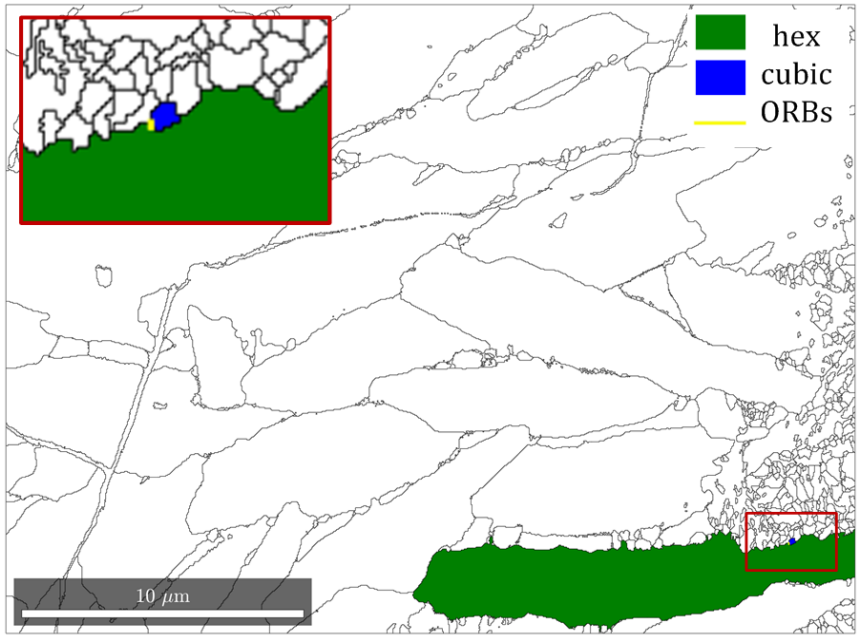

(a)

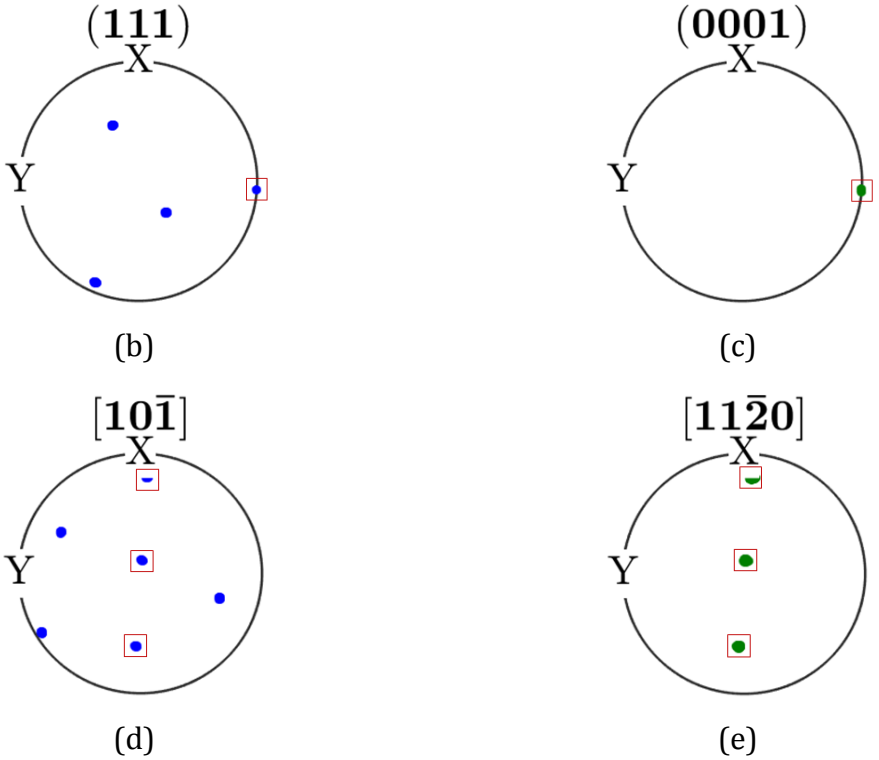

(b) (c)

(d) (e)

Figure 5.8: (a) An interphase boundary segment chosen at random between cubic and hexagonal crystal systems. Pole figure (b, c) planes and (d, e) directions for the (b, d) cubic and (c, e) hexagonal crystal systems for the S-N orientation relationship described as: $(111)_c$ || $(0001)_h$ and $[1\bar{1}0]_c$ || $[11\bar{2}0]_h$.

To re-confirm the orientation relationship between the cubic-hexagonal crystal systems as per the TEM based notation scheme shown in Figure 5.2b-e, an interphase boundary segment was chosen at random (Fig. 5.8). Since the S-N orientation relationship is described as: $(111)_c$ || $(0001)_h$ and $[1\bar{1}0]_c$ || $[11\bar{2}0]_h$, the pole figures of the respective planes and directions for the cubic and hexagonal crystal systems are plotted (Figure 5.8b-e). The overlap between the diffraction spots is highlighted with red squares for both sets of planes and directions, and they confirm the S-N orientation relationship between the cubic and hexagonal grains of $BaTiO_3$. In summary, the S-N orientation relationship between cubic and hexagonal crystal systems can described as: $(111)_c$ || $(0001)_h$ and $[1\bar{1}0]_c$ || $[11\bar{2}0]_h$ with a theoretical misorientation angle of 56.6003° and rotation axes of $[uvw]_c$ = $[\overline{1.6918}\ \overline{2.2047}\ 0.7007]$ or $\sim[\bar{2}\ \bar{3}\ 1]$ for the cubic crystal system and $[UVTW]$ = $[\overline{3.3787}\ \overline{2.1239}\ 5.5026\ 3.4145]$ or $\sim[\bar{2}\ \bar{1}\ 3\ 2]$ or $[uvw]_h$ = $\left[\overline{8.8813}\ \overline{7.6265}\ 3.4145\right]$ or $\sim[\bar{3}\ \bar{2}\ 1]$ for the hexagonal crystal system.

Cubic-monoclinic interphase boundaries

The following section presents an analysis of cubic-hexagonal interphase boundaries based on an EBSD map of the TaC_Ar samples of $BaTiO_3$ (Fig. 5.9a). The intraphase LABs are marked by yellow lines whereas the colour of the interphase HABs depends on the misorientation angle based on the cubic-hexagonal orientation relationship found previously in section 5.2.1. A histogram of the cubic-hexagonal interphase boundaries misorientation distribution using 1° class intervals and the uncorrelated cubic-monoclinic interphase boundaries McKenzie distribution are shown in Figure 5.9b. The maximum theoretical misorientation angle for the cubic-monoclinic crystal pair was 62.7994° at the forbidden zone limit (in red), with a peak 45°. Once again, the interphase boundary distribution does not follow the McKenzie distribution with a peak at 34.6651°; which in turn, conforms to the theoretical misorientation angle between cubic and hexagonal phases for the $(002)_c$ || $(0\bar{2}0)_m$ and $[120]_c$ || $[001]_m$ orientation relationship (Figure 5.3b and c).

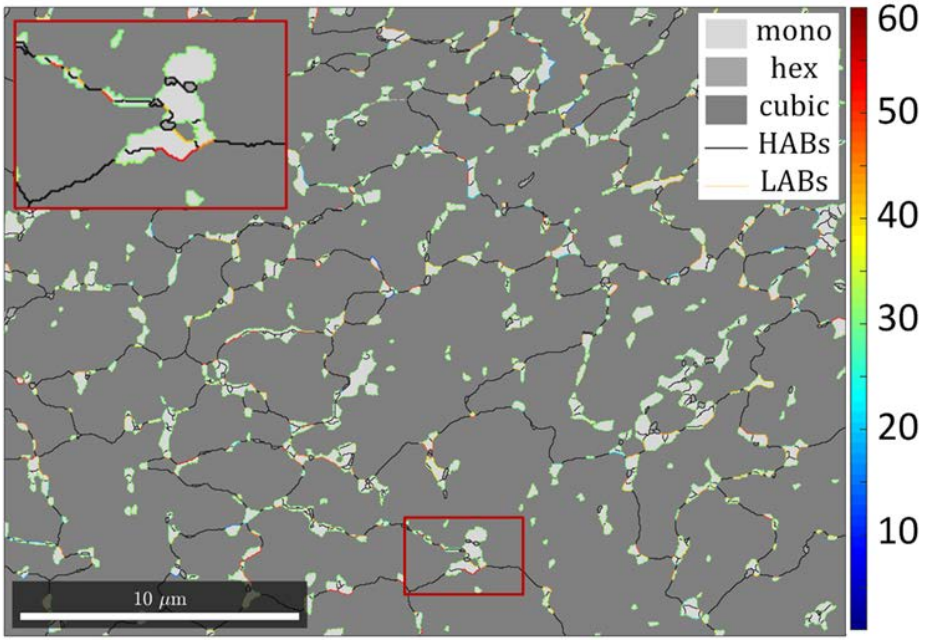

(a)

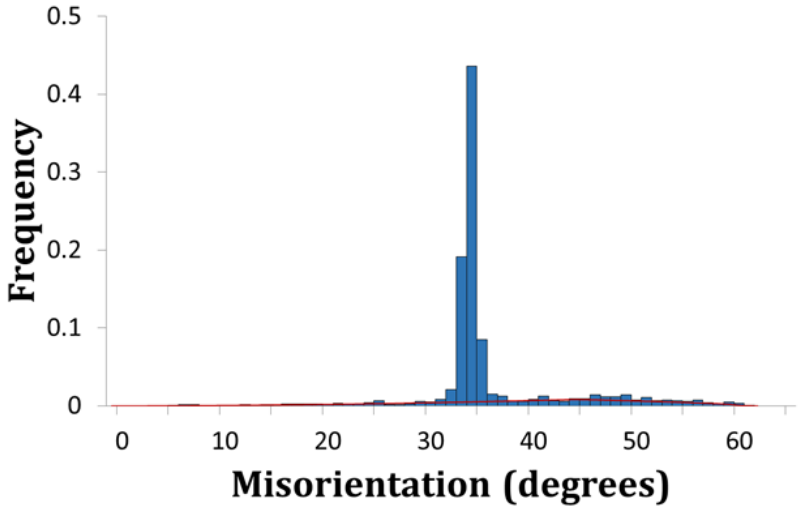

(b)

Figure 5.9: (a) Cubic-monoclinic interphase boundary misorientation map of EDAMM processed $BaTiO_3$ TaC_Ar sample and (b) histogram of interphase misorientation distribution using 1° class intervals. Legend: (a) light grey = monoclinic $Ba_2Ti_6O_{13}$, medium grey = hexagonal $BaTiO_3$, dark grey = cubic $BaTiO_3$, white = zero solutions, black = high-angle grain boundaries (HABs) and ivory = low-angle grain boundaries (LABs).

In this regard, 69.9% of the cubic-monoclinic interphase boundary population is within a ±2.5° deviation of the theoretical misorientation angle for the above orientation relationship (Figure 5.10a, boundaries in purple). As shown in the inset, it can be clearly seen that individual cubic and monoclinic grains tend to share entire interphase boundary segments with each other. When the misorientation (rotation) axis distributions in the cubic and monoclinic crystal co-ordinate systems are plotted (Fig. 5.10b and c), there is a single peak for both plots that is centred around the theoretical rotation axes and conforms to the $(002)_c$ || $(0\bar{2}0)_m$ and $[120]_c$ || $[001]_m$ orientation relationship defined as $[uvw]_c$ = [0 2.866 0] or ~[0 1 0] for the cubic crystal system and $[uvw]_m$ = [0 3.953 0] or ~[0 4 0] for the monoclinic crystal system.

In order to re-confirm the orientation relationship between the cubic-monoclinic crystal systems as per the TEM based notation scheme shown in Figure 5.3b and c, an interphase boundary segment was chosen at random (Fig. 5.11a). Since the orientation relationship is described as: $(002)_c$ || $(0\bar{2}0)_m$ and $[120]_c$ || $[001]_m$ the pole figures of the respective planes and directions for the cubic and monoclinic crystal systems are plotted in Fig. 5.11b and c. Overlaps highlighted by red squares for both planes and directions serve as confirmation the existence of the above orientation relationship between the cubic and monoclinic crystal systems.

In summary, the orientation relationship between cubic and monoclinic crystal systems can be described as: $(002)_c$ || $(0\bar{2}0)_m$ and $[120]_c$ || $[001]_m$ with a theoretical misorientation angle of 34.6651° and rotation axes of $[uvw]_c$ = [0 2.866 0] or ~[0 1 0] for the cubic crystal system and $[uvw]_m$ = [0 3.953 0] or ~[0 4 0] for the monoclinic crystal system.

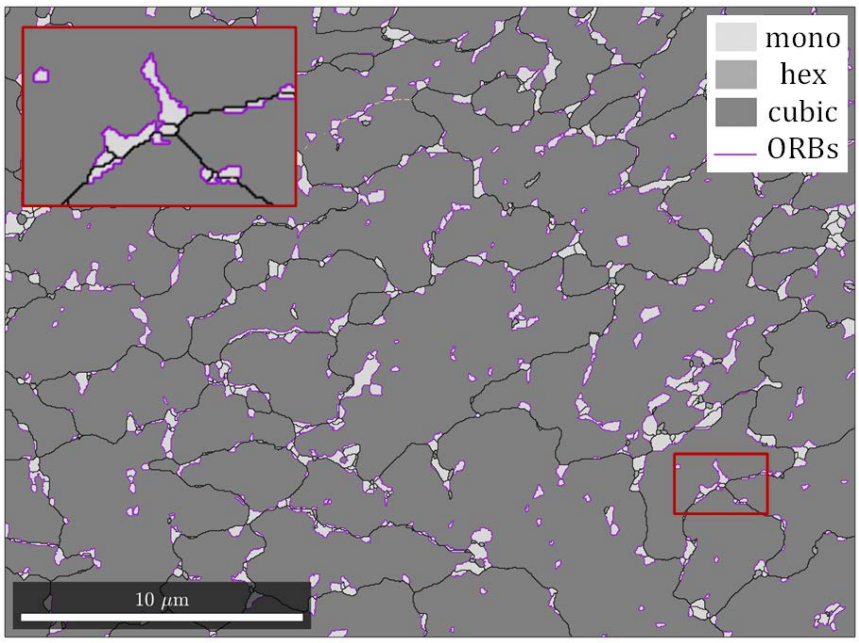

(a)

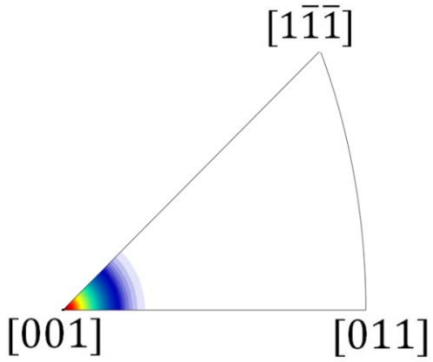

(b)

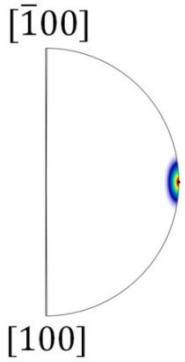

(c)

Figure 5.10: (a) The cubic-monoclinic interphase boundary population within a ±2.5° deviation of the theoretical misorientation angle for the $(002)_c$ || $(0\bar{2}0)_m$ and $[120]_c$ || $[001]_m$ orientation relationship (in purple). Rotation axis distributions in the (b) cubic and (c) monoclinic crystal co-ordinate systems.

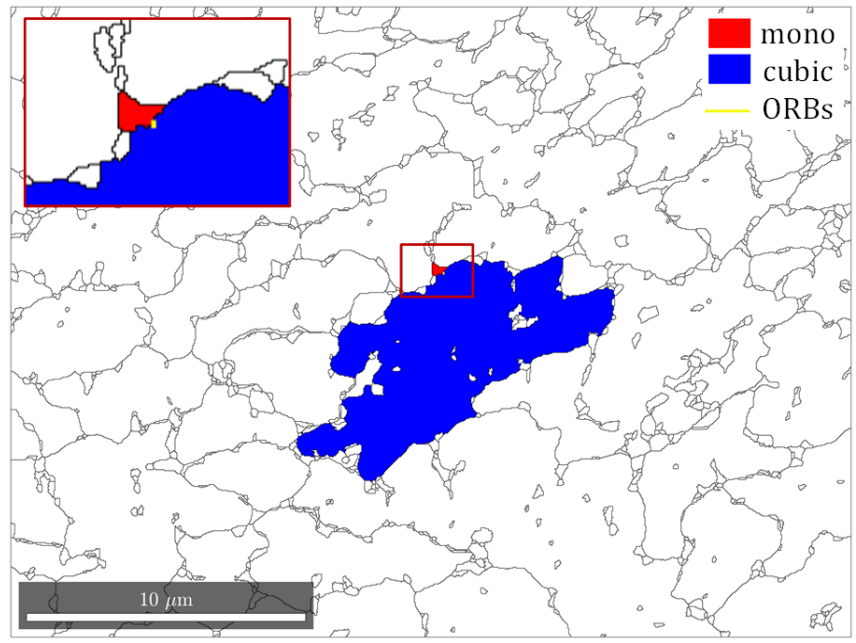

(a)

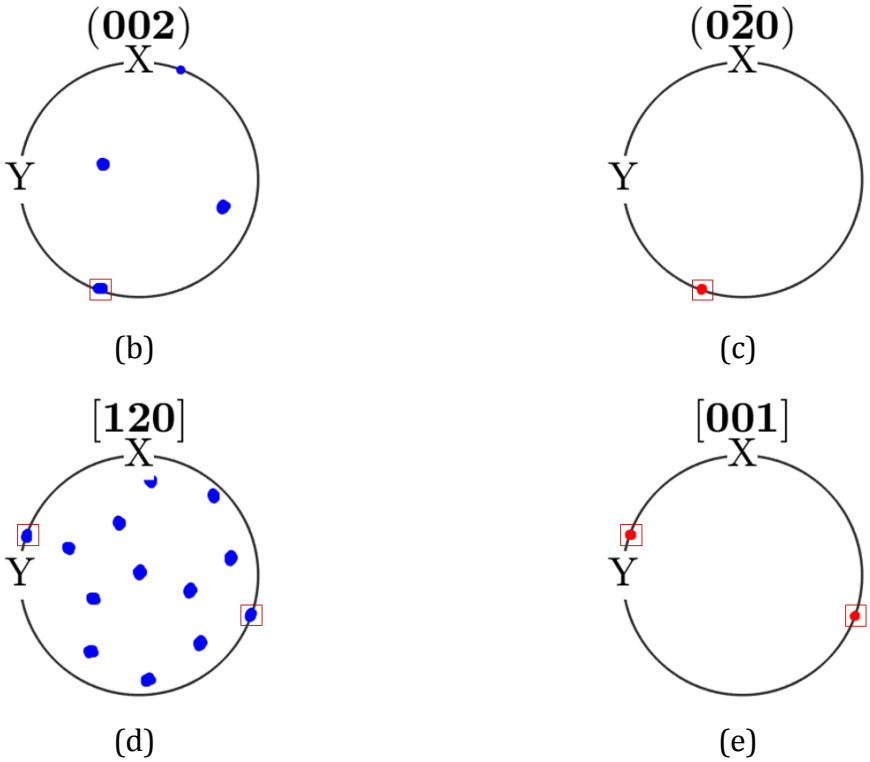

(b) (c)

(d) (e)

Figure 5.11: (a) An interphase boundary segment chosen at random between cubic and monoclinic crystal systems. Pole figure (b, c) planes and (d, e) directions for the (b, d) cubic and (c, e) monoclinic crystal systems for the orientation relationship described as: $(002)_c$ || $(0\bar{2}0)_m$ and $[120]_c$ || $[001]_m$.

Hexagonal-monoclinic interphase boundaries

The following section cubic-hexagonal interphase boundaries analysis based on the EBSD map of the O_2/Ar samples of $BaTiO_3$is presented (Fig. 5.12a). The intraphase LABs are marked by yellow lines whereas the colour of the interphase HABs display depends on the misorientation angle based on the cubic-hexagonal orientation relationship found previously in section 5.2.1. This last type of interphase boundary proved to be the most difficult to analyse because of the lack of symmetry of the monoclinic crystal structure and a large amount of possibilities to form the orientation relationships with hexagonal crystal. Once the troublesome orientation relationship was found through multiple FIB lamellae TEM analysis, the results were included in the computational method of EBSD data analysis.

Typical microstructure of O_2/Ar samples of $BaTiO_3$ together with high and low angle grain boundaries (LABs and HABs) are shown in Figure 5.12. It should be noted that the angle within which the high angle boundaries are considered in this case is near 90°, whereas for the cubic-hexagonal and cubic-monoclinic interphases its maximum was found to be at 56.6003° and 62.7994°, respectively. This breadth of angular distribution may give much more possibilities of an orientation relationship between the two phases, but it also makes them more difficult to find. Figure 5.12b shows that the McKenzie random distribution of uncorrelated hexagonal-monoclinic interphase boundaries has a maximum theoretical misorientation angle of 93.8410° at the forbidden zone limit (in red). Once more, the interphase boundary distribution does not follow the McKenzie distribution with a peak at 84.5379°; which in turn, conforms to the theoretical misorientation angle between hexagonal and monoclinic phases for the $(10\bar{1}2)_h \parallel (\bar{2}02)_m$ and $[\bar{2}201]_h \parallel [010]_m$ orientation relationship (Fig. 5.4b and c).

In this case only 29.4% of the hexagonal-monoclinic interphase boundary population is within a ±2.5° deviation of the theoretical misorientation angle for the above orientation relationship (Figure 5.13, boundaries in purple). The inset shows that individual hexagonal and monoclinic grains tend to share entire interphase boundary

segments with each other. When the misorientation (rotation) axis distributions in the hexagonal and monoclinic crystal co-ordinate systems are plotted (Fig. 5.13b and c), there is a single peak for both plots that are centred around the theoretical rotation axes and conform to the $(10\bar{1}2)_h$ || $(\bar{2}02)_m$ and $[\bar{2}201]_h$ || $[010]_m$ orientation relationship, and are defined as [UVTW] = $\left[1.995\ 3.4316\ \overline{5.4267}\ 3.9531\right]$ or ~[1 2 $\bar{3}$ 2] or $[uvw]_h$ = [7.4217 8.8583 3.9531] or ~[2 2 1] for the hexagonal crystal system, and $[uvw]_m$ = [5.2296 3.5321 2.0999] or ~[5 4 2] for the monoclinic crystal system.

In order to re-confirm orientation relationship between the hexagonal-monoclinic crystal systems as per the TEM based notation scheme shown in Figure 5.4b and c, an interphase boundary segment was chosen at random (Figure 5.14a). Since the orientation relationship is described as: $(10\bar{1}2)_h$ || $(\bar{2}02)_m$ and $[\bar{2}201]_h$ || $[010]_m$ the pole figures for the respective planes and directions of the hexagonal and monoclinic crystal systems are plotted in Fig. 5.14d-e. Overlaps in both planes and directions, highlighted by red squares, serve as re-confirmation of the existence of the above orientation relationship between the hexagonal and monoclinic crystal systems.

In summary, the orientation relationship between hexagonal and monoclinic crystal systems can described as: $(10\bar{1}2)_h$ || $(\bar{2}02)_m$ and $[\bar{2}201]_h$ || $[010]_m$ with a theoretical misorientation angle of 84.5379° and rotation axes of [UVTW] = $\left[1.995\ 3.4316\ \overline{5.4267}\ 3.9531\right]$ or ~[1 2 $\bar{3}$ 2] or $[uvw]_h$ = [7.4217 8.8583 3.9531] or ~[2 2 1] for the hexagonal crystal system and $[uvw]_m$ = [5.2296 3.5321 2.0999] or ~[5 4 2] for the monoclinic crystal system.

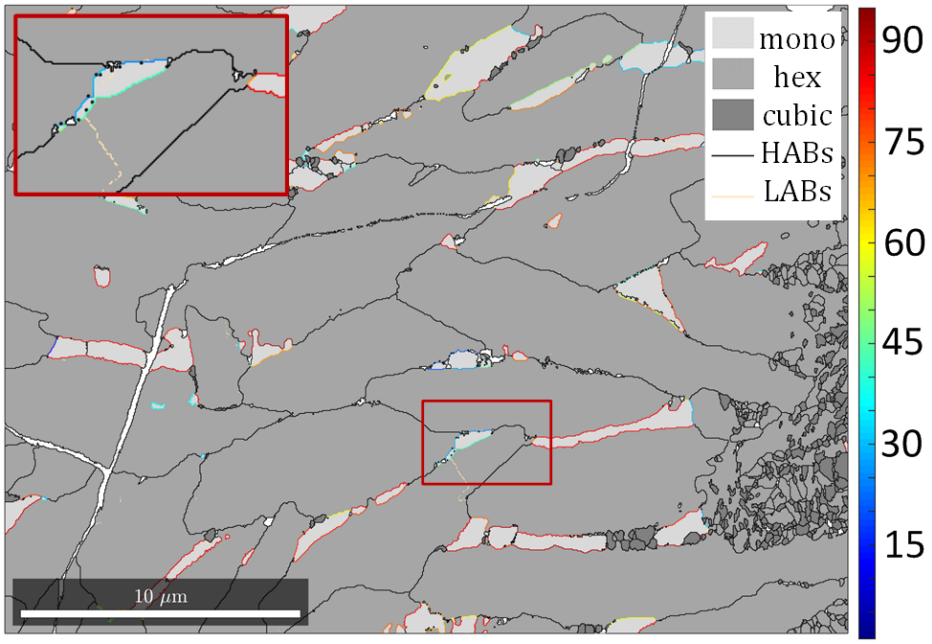

(a)

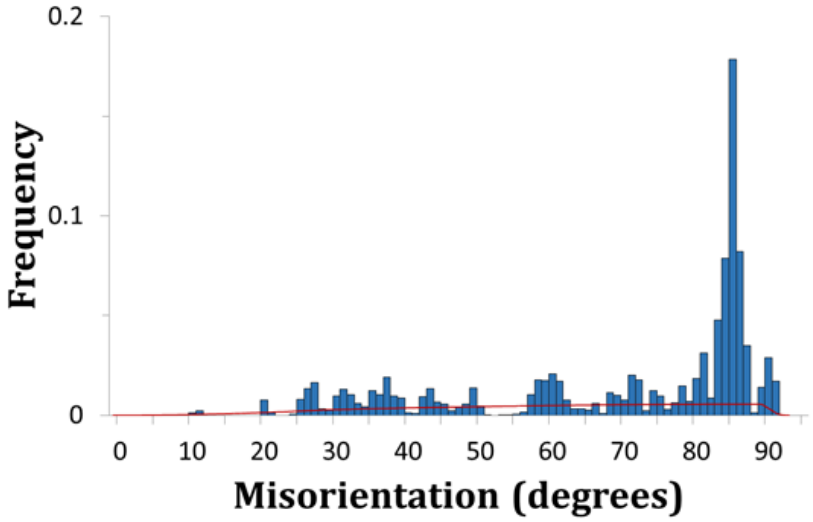

(b)

Figure 5.12: (a) Hexagonal-monoclinic interphase boundary misorientation map of EDAMM processed $BaTiO_3$ O_2/Ar sample and (b) histogram of interphase misorientation distribution using 1° class intervals. Legend: (a) light grey = monoclinic $Ba_2Ti_6O_{13}$, medium grey = hexagonal $BaTiO_3$, dark grey = cubic $BaTiO_3$, white = zero solutions, black = high-angle grain boundaries (HABs) and ivory = low-angle grain boundaries (LABs).

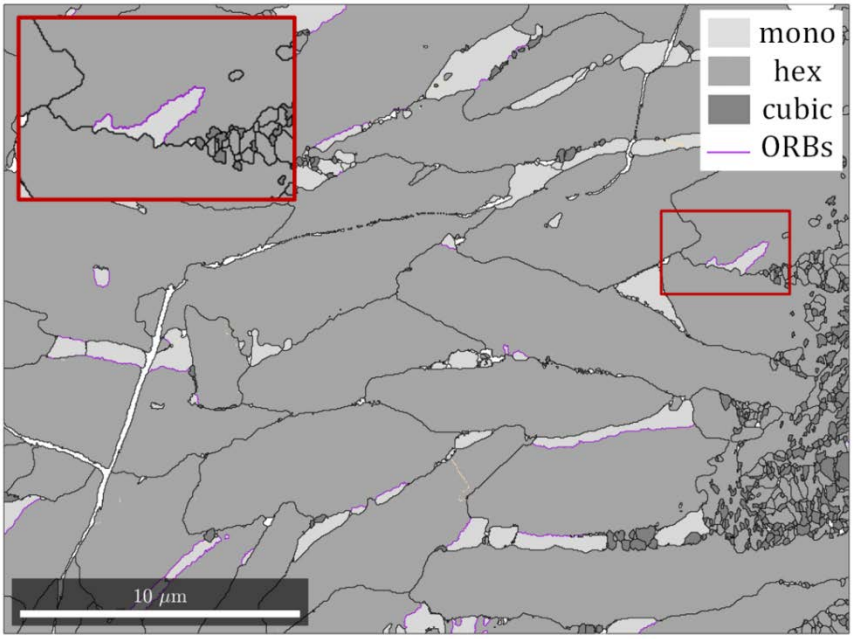

(a)

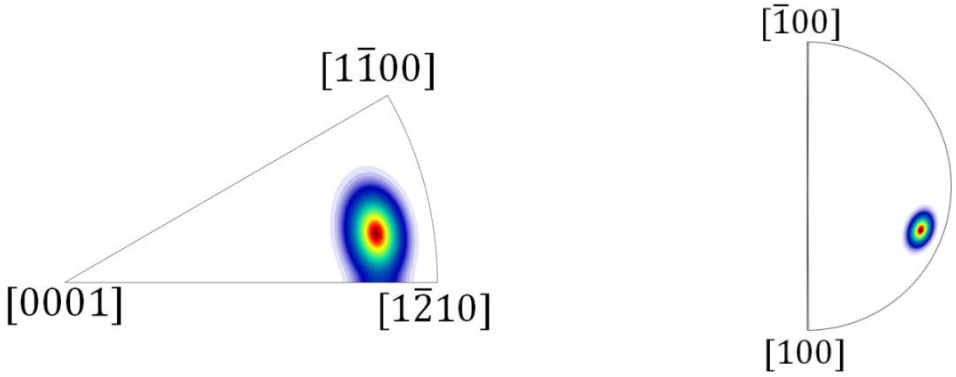

(b) (c)

Figure 5.13: (a) The hexagonal-monoclinic interphase boundary population within a ±2.5° deviation of the theoretical misorientation angle for the $(10\bar{1}2)_h$ || $(\bar{2}02)_m$ and $[\bar{2}201]_h$ || $[010]_m$ orientation relationship (in purple). Rotation axis distributions in the (b) hexagonal and (c) monoclinic crystal co-ordinate systems.

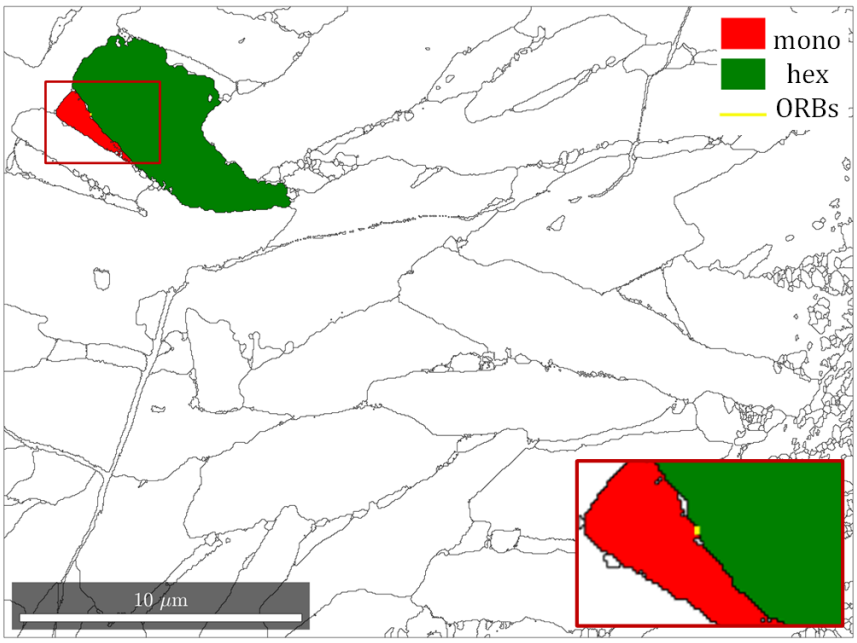

(a)

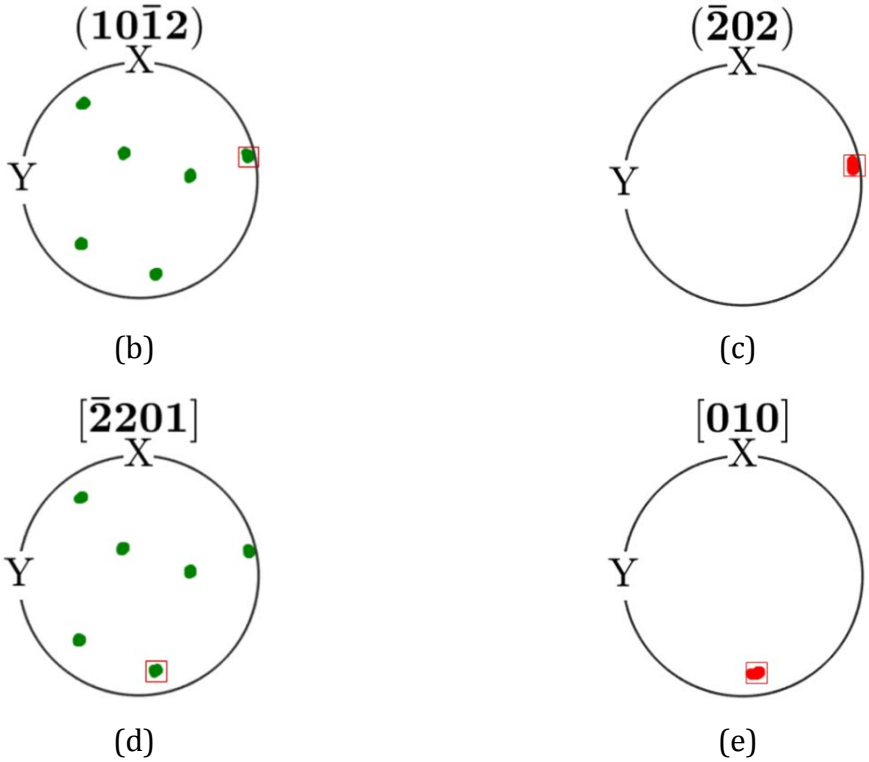

(b) (c)

(d) (e)

Figure 5.14: (a) An interphase boundary segment chosen at random between hexagonal and monoclinic crystal systems. Pole figure (b, c) planes and (d, e) directions for the (b, d) hexagonal and (c, e) monoclinic crystal systems for the orientation relationship described as: $(10\bar{1}2)_h$ || $(\bar{2}02)_m$ and $[\bar{2}201]_h$ || $[010]_m$.

5.3 Discussion

This chapter deals with a crystallographic analysis of the orientation relationships between phases obtained in EDAMM processed BaO-TiO_2 powders to form $BaTiO_3$. The samples used in the analysis were TaC_Ar, most of which was of the cubic $BaTiO_3$ phase and O_2/Ar samples that were mostly of the hexagonal $BaTiO_3$ phase. In both cases there was a secondary monoclinic $Ba_2Ti_6O_{13}$ phase and the relationship between the three phases was analysed using a new computational technique to correlate the data obtained from TEM and EBSD techniques.

Statistical analysis of data obtained through analysis of the computational approach of EBSD mapping with regard to the orientation relationship boundaries distribution

In the first section of this chapter it was proven that in both TaC_Ar and O_2/Ar samples all the phases had displayed an orientation relationship between each other (summary in Table 5.4). The presence of an orientation relationship means that the two adjacent grains share a common crystallographic plane which enabled them to grow from one another at some point during processing. This phenomenon, well-known as the parent-daughter relationship, showed the best fit between the two adjacent grains and is vital when talking about phase transformations. Theoretical analysis of chosen crystal types and their possible orientation relationships (i.e. variants) typically gives a large amount of possibilities (ex. 24 variants in Kurdjumow-Sachs [121]) but only few of them are typically dominant and serve as an indication of the transformation mechanism. When the orientation relationship of a large number of grains is analysed, the information can then be correlated with the direction of growth.

Formation of the phases during BaO-TiO_2 EDAMM processing seems to consist of two different phenomena: a solid-state martensitic transformation of cubic↔hexagonal $BaTiO_3$ and the grain growth of these phases at the expense of monoclinic $Ba_2Ti_6O_{13}$.

Table 5.4: Summary of misorientation angles and orientation relationships for the cubic-hexagonal, cubic-monoclinic and hexagonal-monoclinic phases in EDAMM processed BaO-TiO_2 powders.

$BaTiO_3$ interphase boundary type	**Misorientation angle**	**Orientation relationship**	
		Planes	**Directions**
Cubic $BaTiO_3$ - hexagonal $BaTiO_3$	56.6003	$(111)_c \parallel (0001)_h$	$[1\bar{1}0]_c \parallel [11\bar{2}0]_h$
Cubic $BaTiO_3$ - monoclinic $Ba_2Ti_6O_{13}$	34.6651	$(002)_c \parallel (0\bar{2}0)_m$	$[120]_c \parallel [001]_m$
Hexagonal $BaTiO_3$ - monoclinic $Ba_2Ti_6O_{13}$	84.5379	$(10\bar{1}2)_h \parallel (\bar{2}02)_m$	$[\bar{2}201]_h \parallel [010]_m$

5.3.1 Cubic-monoclinic interphase boundaries

Formation of the phases during BaO-TiO_2 EDAMM processing seems to consist of two different phenomena: solid-state martensitic transformation of cubic↔hexagonal $BaTiO_3$ and grain growth of these phases at the expense of monoclinic $Ba_2Ti_6O_{13}$. A clear evidence of it is the formation mechanism patterns developed in Chapter 4, based on the microscopic observations and XRD analysis (Fig. 4.20, Fig. 4.21). It has been shown that in case of TaC_Ar sample, 2 min of the processing resulted in formation of the orthorhombic type of $BaTiO_3$ which within the next minute transforms into the cubic $BaTiO_3$. From the micrographs of typical microstructure of the samples produced after 2 min, the amount of the secondary phase with the chemistry near the monoclinic $Ba_2Ti_6O_{13}$is significant; however its amount after another 2 min of processing is significantly reduced. This, together with an orientation

relationship between the cubic and secondary monoclinic $Ba_2Ti_6O_{13}$ suggests that within than time of the processing the transformation from orthorhombic to cubic $BaTiO_3$ crystals occurred, but also, that the final microstructure was developed at the expense of the secondary phase.

It was found that almost 70% of the cubic $BaTiO_3$-monoclinic $Ba_2Ti_6O_{13}$ interphase boundaries with the deviation of 2.5° agree with the conditions of orientation relationship, what clearly shows that there is a strong correlation between the two phases. As some studies show, there are many reasons as to why this number is not even higher and, as pointed out in [122], may be due to the scan accuracy, which in our view because of the large features we can ignore in this case. More importantly, the fact that EBSD is a surface analysis technique means that plenty of features of a 3D microstructure remain undetected. In the case of a textured material sample preparation involves appropriate cut enabling observation of some specific grain orientations but powder particles with quite random grain distribution and orientation cannot be prepared in the same manner. Decreasing the tolerance of the deviation from the orientation relationship to ±0.25° results in a decrease of interphase boundaries compliant with it to 5.48% which suggests that those interphase boundaries have formed at some point in the process but were likely displaced, resulting in presence of internal stresses and deformation of the interphase boundary. As grain boundaries tend to accumulate dislocations upon the plastic deformation, breaking down the orientation relationship can occur when prolonged processing times are applied.

Cubic $BaTiO_3$-monoclinic $Ba_2Ti_6O_{13}$ interphases in the O_2/Ar samples reveal a similar trend where the 2.5° deviation of misorientation angle returns the value of OR-compliant boundaries of 29.80% and for ±0.25° the value decreases to 0.45%. In this case the amount of available grain boundaries is much smaller, and the lower value of OR compliant grain boundaries was expected due to higher stresses connected with additional transformations of cubic to hexagonal crystals and therefore additional stresses in the lattices. An example of such behavior can be found in martensitic and

bainitic transformations where the matrix (in our case monoclinic $Ba_2Ti_6O_{13}$) is said to accommodate the shape strain of the transformation[123].

Table 5.5: Population of interphase boundaries deviating (δ) from the theoretical orientation relationship in the Ar atmosphere and a mixture of O_2/Ar samples.

Sample type	**Interphase boundary type**	**Population of interphase boundaries deviating from theoretical OR (%)**	
		δ = ±0.25°	**δ = ±2.5°**
TaC_Ar	Cubic $BaTiO_3$ - Hexagonal $BaTiO_3$	35.60	77.90
	Cubic $BaTiO_3$ - Monoclinic $Ba_2Ti_6O_{13}$	5.48	69.90
	Hexagonal $BaTiO_3$ - Monoclinic $Ba_2Ti_6O_{13}$	0.10	39.90
O_2/Ar	Cubic $BaTiO_3$ - Hexagonal $BaTiO_3$	52.3	78.97
	Cubic $BaTiO_3$ - Monoclinic $Ba_2Ti_6O_{13}$	0.45	29.80
	Hexagonal $BaTiO_3$ - Monoclinic $Ba_2Ti_6O_{13}$	0.13	29.40

5.3.2 Hexagonal-monoclinic interphase boundaries

It was indicated in the previously developed O_2/Ar sequence of phase formation (Fig. 4.22), that the hexagonal grains are formed from the cubic ones in the process called martensitic transformation involving small displacements of the atoms which result in the change of the crystal structure. The transformation was observed in much larger extent in the O_2/Ar sample but some small grains have been observed also in the TaC_Ar sample where the temperature of the EDAMM processing is thought to be

much smaller. Since the change in lattice parameter during the cubic→hexagonal transformation occurs, the same type of orientation relationship may not be sustained anymore due to strains in the material. Hence, a new relationship was observed for hexagonal $BaTiO_3$-monoclinic $Ba_2Ti_6O_{13}$ interphase boundaries (Table 5.4) and the amount of grain boundaries which are compliant with the orientation relationship is even smaller (Table 5.5). Additionally, the spread from the ideal orientation relationship is much larger than in the previously discussed interphase where only a minute fraction of OR-compliant boundaries are within the 0.25° misorientation deviation.

5.3.3 Cubic-hexagonal interphase boundaries

The biggest amount of OR-compliant interphase boundaries was found for a cubic $BaTiO_3$ -hexagonal $BaTiO_3$ pair. In case of both TaC_Ar samples and O_2/Ar samples the values of OR-compliant boundaries is very high- 77.90% and 78.97%, respectively, when the tolerance for the deviation from the OR of ±2.5° was used. Not surprisingly this high number was also recorded for the restriction of the OR-compliance conditions of ±0.25° where in case of TaC_Ar a value of 35.60% and for O_2/Ar 52.3% was recorded. This result is important as is shows that the variation of the OR-compliant boundaries is relatively small which proves a strong relationship between the phases.

Optimization of the EDAMM processing towards obtaining majority of cubic or hexagonal $BaTiO_3$, presented as samples of group TaC_Ar and O_2/Ar was proven to contain similar values of compliance of interphase boundaries to the specified orientation relationship. It can be stated that in case of TaC_Ar sample, the optimization of the conditions lead to the decrease of the processing temperature, as only a small amount (~0.5% based on the micrographs) of hexagonal phase was observed, which is a higher temperature polymorph of $BaTiO_3$. On the other hand, O_2/Ar samples were assessed to contain ~89% of the hexagonal grains, based on the micrographs with only minor amount of the cubic phase. This in turn proves that the

majority of the cubic phase was transformed into the hexagonal grains stable in higher temperature. Because of the martensitic character of the transformation, it is possible for the high temperature hexagonal $BaTiO_3$ phase to transform back to the cubic $BaTiO_3$ upon slow cooling, based on the equilibrium diagram. The fact that such mass transformation did not occur and the majority of the hexagonal $BaTiO_3$ was retained is yet another indication of fast cooling EDAMM processing. It also indicates that all the observed microstructures are observed upon fast cooling or even quenching.

Keeping this fact in mind, based on the phase diagram, cubic $BaTiO_3$ phase exists below 1539°C at the TiO_2 rich end and 1430°C at the BaO rich end. Above these temperatures, it is then fully transformed to hexagonal crystal structure, which is regarded as a maximum reached in Ar. It was pointed out in [124], these temperatures can be slightly altered depending on the speed of the temperature increase. It was found that slow ramp in temperature resulted in the persistence of the cubic phase even beyond the 1500°C but the experiment was carried out in a tube furnace with the upper temperature limit of ~1650°C. It is thought that during the EDAMM processing the plastic deformation plays an important role in formation of the many metastable phases but also in suppressing the transformations when the processing conditions are optimised. It has been previously shown that the mechanical activation by ball milling aids formation of nanocrystalline $BaTiO_3$ and lowers the calcination temperature [125].

5.3.4 Intermediate stage of EDAMM processing

The EBSD scan of the particle which was processed in the O_2/Ar sample conditions for 1 min is presented in Fig. 5.15. Both hexagonal and cubic $BaTiO_3$ phases are present in the particle with secondary phase of monoclinic $Ba_2Ti_6O_{13}$ marked in red. It can be noted that the number of interfaces between the cubic $BaTiO_3$ and monoclinic $Ba_2Ti_6O_{13}$ grains is significantly larger than these of hexagonal $BaTiO_3$-monoclinic $Ba_2Ti_6O_{13}$. It is thought, based on the XRD analyses and micrographs, that the cubic $BaTiO_3$grains together with monoclinic $Ba_2Ti_6O_{13}$ is formed simultaneously

in an intermediate stage of the processing. Later, transformation of the cubic $BaTiO_3$ to hexagonal $BaTiO_3$ takes place, where the grain growth of the hexagonal $BaTiO_3$ is most likely be halted on the monoclinic interphase. An indication of the latter is much higher misorientation angle between these two phases in comparison to the cubic-monoclinic interphase (Table 5.4).

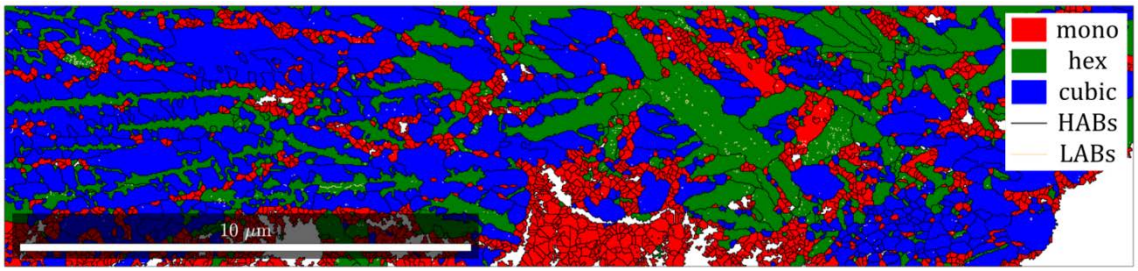

Figure 5.15: Representative phase map of the powder particle intermediate stage of EDAMM processed O_2/Ar sample. Legend: red - monoclinic $Ba_2Ti_6O_{13}$, green - hexagonal $BaTiO_3$, blue-= cubic $BaTiO_3$, white - zero solutions, black - high-angle grain boundaries (HABs).

5.4 Conclusions

In the above presented chapter the interphase boundary regions of the phases found in the TaC_Ar and O_2/Ar samples processed in EDAMM were analysed using the TEM and EBSD, with additional analysis of EBSD data the newly developed computational tool. In both of the samples the phases found were; cubic $BaTiO_3$, hexagonal $BaTiO_3$ and monoclinic $Ba_2Ti_6O_{13}$. Orientation relationships between these three phases were found, which proves that parent-daughter relationships between phases exist, and also demonstrates which phases were growing at the expense of each other during the EDAMM processing. The analysis of the deviation from the ideal orientation relationships were found to be the largest for the cubic $BaTiO_3$- monoclinic $Ba_2Ti_6O_{13}$ pair, and this is attributed to the formation of the cubic-monoclinic interface in the early stages of the processing and subsequent deformation and reorientation of crystals during grain growth and plastic deformation. In case of the TaC_Ar sample the growth of cubic $BaTiO_3$ grains happened at the expense of monoclinic $Ba_2Ti_6O_{13}$ and

only minute amount of the hexagonal phase was found. In the O_2/Ar samples on the other hand, the majority of the phase was found to be the hexagonal $BaTiO_3$ with a small percentage of retained cubic $BaTiO_3$ and monoclinic $Ba_2Ti_6O_{13}$. Analysis of these three interphases leads to the conclusion that the cubic $BaTiO_3$ grains grew at the expense of the monoclinic $Ba_2Ti_6O_{13}$ at the early stages of the processing. Further processing resulted in the hexagonal $BaTiO_3$ grain growth at the expense of cubic $BaTiO_3$, but here, the interphase boundaries were observed to comply well to the ideal orientation relationship. This indicates that; the cubic-hexagonal orientation relationship found through SAED is the dominant relationship in this phase transformation regime, (ii) the cubic→hexagonal transformation occurred by the end of the EDAMM processing and (iii) the powder particles in EDAMM are cooled extremely fast as the high temperature hexagonal $BaTiO_3$ polymorph is sustained in the room temperature.

CHAPTER 6

Summary and future work

This thesis has demonstrated new understanding of how Electric Discharge Assisted Mechanical Milling can induce phase transformations in variety of materials including: metals, carbides, oxides and high melting point ceramics. Analysis of the results leads us to believe that the *equivalent temperatures* of processes occurring in EDAMM under Ar are within the range; 600-1600°C, for the range of plasma pulse intensities trialled. Because of the fact that the Ar gas was found to result in highly localized plasma discharges and therefore large deviations of the temperatures during processing two modifications were introduced to address this problem. Firstly, a TaC coating on the EDAMM the electrode was applied in order to lower the processing temperature, which proved successful in a synthesis experiment involving production of the $BaTiO_3$ low temperature polymorph from BaO-TiO_2 staring powders. Secondly, an O_2/Ar was used to increase the processing temperature in order to obtain exclusively high temperature stable $BaTiO_3$ polymorph. An in-depth investigation of the BaO-TiO_2 staring powders processing products revealed formation of nanoparticles in the first stages of processing and further formation of larger particles in the later stages. A crystallographic and microstructural analysis enabled determination of the sequences of the phase formation during EDAMM when, (i) a TaC coated electrode or (ii) an O_2/Ar atmosphere was used. Extensive analysis of the boundary regions between the phases undergoing polymorphic transformation (cubic $BaTiO_3$↔hexagonal $BaTiO_3$) and phase transformation from a secondary monoclinic $Ba_2Ti_6O_{13}$ phase was performed. It was found that the cubic $BaTiO_3$ phase grows at the expense of monoclinic $Ba_2Ti_6O_{13}$. At higher temperatures, the cubic $BaTiO_3$ phase is sacrificed for the growth of hexagonal $BaTiO_3$ phase which typically occurs at ~1430˚C. It was also established that the particles produced at higher temperatures undergo rapid cooling and retaining the high temperature polymorph of $BaTiO_3$ and this result is attributed to the short time pulse discharge affecting them during the processing.

Due to the results presented in this thesis it is recommended to continue the research with the following;

- Exploring the alternatives to the TaC coating such as other carbides with high melting points and analysis of their influence on the processing in EDAMM,

- Further investigation into the influence of gases such N_2, H_2, pure O_2 and He on temperature of polymorphic transformations,
- Extending the investigation and optimized processing conditions in more complex multi-element oxides,
- Introducing spectrometer method to be a part of the EDAMM processing chamber to define the species taking part in the plasma processing which could further improve the knowledge about the exact processing temperatures.

References

1. Chen, Y. and J.S. Williams, *High-energy ball-milling-induced non-equilibrium phase transformations.* Materials Science and Engineering: A, 1997. **226-228**: p. 38-42.
2. Sharma, P., S. Sharma, and D. Khanduja, *On the Use of Ball Milling for the Production of Ceramic Powders.* Materials and Manufacturing Processes, 2015. **30**(11): p. 1370-1376.
3. Takacs, L., *Self-sustaining reactions induced by ball milling.* Progress in Materials Science, 2002. **47**(4): p. 355-414.
4. Radlinski, A.P. and A. Calka, *Mechanical alloying of high melting point intermetallics.* Materials Science and Engineering: A, 1991. **134**(0): p. 1376-1379.
5. Calka, A. and A.P. Radlinski, *Universal high performance ball-milling device and its application for mechanical alloying.* Materials Science and Engineering: A, 1991. **134**: p. 1350-1353.
6. Maurice, D.R. and T.H. Courtney, *The physics of mechanical alloying: A first report.* Metallurgical Transactions A, 1990. **21**(1): p. 289-303.
7. Cocco, G., F. Delogu, and L. Schiffini, *Toward a Quantitative Understanding of the Mechanical Alloying Process.* Journal of Materials Synthesis and Processing, 2000. **8**(3): p. 167-180.
8. Ghosh, B. and S.K. Pradhan, *Microstructural characterization of nanocrystalline SiC synthesized by high-energy ball-milling.* Journal of Alloys and Compounds, 2009. **486**(1): p. 480-485.
9. Singh, K.C. and A.K. Nath, *Barium titanate nanoparticles produced by planetary ball milling and piezoelectric properties of corresponding ceramics.* Materials Letters, 2011. **65**(6): p. 970-973.
10. Lohse, B.H., *The controlled ball milling of titanium and carbon to form TiC*, in *School of Mechanical, Materials and Mechatronic Engineering - Faculty of Engineering*. 2005, University of Wollongong.
11. Quan, Y., Z. Yong, and Y. Hai-zhou, *Rapid synthesis of Ti(C, N) powders by mechanical alloying and subsequent arc discharging* Trans. Nonferrous Met. Soc. China, 2011. **21**: p. 1545-1549.
12. Zhu M, D.L., Cao B, Ouyang LZ. 2007: China.
13. Dai, L.Y., et al., *A new method of synthesizing ultrafine vanadium carbide by dielectric barrier discharge plasma assisted milling.* International Journal of Refractory Metals and Hard Materials, 2012. **30**(1): p. 48-50.
14. Zhu, M., et al., *Synergism of mechanical milling and dielectric barrier discharge plasma on the fabrication of nano-powders of pure metals and tungsten carbide.* Journal of Alloys and Compounds, 2009. **478**(1–2): p. 624-629.
15. Sen, W., et al., *Comparative research of plasma-assisted milling and traditional milling in synthesizing AlN.* Plasma Science and Technology, 2017. **19**(6): p. 064005.
16. Scott, S.J., C.C. Figgures, and D.G. Dixon, *Dielectric barrier discharge processing of aerospace materials.* Plasma Sources Science and Technology, 2004. **13**(3): p. 461.
17. Dai, L.Y., B. Cao, and M. Zhu, *Comparison on refinement of iron powder by ball milling assisted by different external fields.* Acta Metallurgica Sinica (English Letters), 2006. **19**(6): p. 411-417.
18. Calka, A. and D. Wexler, *Mechanical milling assisted by electrical discharge.* Nature, 2002. **419**(6903): p. 147-151.

19. Calka, A. and D. Wexler, *Electrical Discharge Assisted Ball Milling: a promising materials synthesis and processing method.* Materials Science Forum 2002. **386-388**: p. 125-134.
20. Needham, S.A., et al., *Synthesis of functional oxides by a novel mechanical milling-electric discharge method.* Journal of Materials Chemistry, 2006. **16**(46): p. 4488-4493.
21. Needham, S.A., et al., *A new rapid synthesis technique for electrochemically active materials used in energy storage applications.* Electrochemistry Communications, 2006. **8**(3): p. 434-438.
22. Calka, A., D. Oleszak, and N. Stanford, *Rapid synthesis of TiC–Fe3C composite by electric discharge assisted mechanical milling of ilmenite (FeTiO3) with graphite.* Journal of Alloys and Compounds, 2008. **459**(1–2): p. 498-500.
23. Bishop, D. and A. Calka, *Phase transformations in ilmenite induced by electric discharge assisted mechanical milling.* Journal of Alloys and Compounds, 2009. **469**(1–2): p. 380-385.
24. Zhang, G. and O. Ostrovski, *Effect of preoxidation and sintering on properties of ilmenite concentrates.* International Journal of Mineral Processing, 2002. **64**(4): p. 201-218.
25. Calka, A., A.A. Chowdhury, and K. Konstantinov, *Rapid synthesis of functional oxides by electric discharge assisted mechanical milling method.* Journal of Alloys and Compounds, 2012. **536, Supplement 1**(0): p. S3-S8.
26. Chowdhury, A.A., et al., *High di-electric constant nano-structure ceramics synthesis using novel electric discharge assisted mechanical milling and magneto ball milling and its properties* International Journal of Nanotechnology, 2014. **11**(9/10/11): p. 728-736.
27. Whipple, E.C., *Potentials of surfaces in space.* Reports on Progress in Physics, 1981. **44**(11): p. 1197.
28. Maurer H. R., K.H., *On the heating of nano- and microparticles in the process plasmas.* J. Phys. D: Appl. Phys, 2011(44): p. 174029.
29. ; Available from: http://cod.iutcaen.unicaen.fr/.
30. Mayer, J., et al., *TEM Sample Preparation and FIB-Induced Damage.* MRS Bulletin, 2011. **32**(5): p. 400-407.
31. Mitchell, D.; Available from: www.dmscripting.com.
32. Calka, A., D. Wexler, and Z.L. Li, *Estimation of milling temperature from phase transformations under low energy milling conditions*, in *Rapidly quenched and metastable materials*, P.M. P. Duhaj, P.Svec, Editor. 1996, Elsevier: Bratislava. p. 191-194.
33. Sully, A.H. and E.A. Brandes, *Metallurgy of the Rarer Metals*. 1967: Butterworths Scientific Publications.
34. Dhananjayan, N. and T. Banerjee, *Crystallographic modifications of manganese and their transformation characteristics. In: Structure of Electro-Deposited Manganese.* 1969: National Metallurgical Labolatory, Jamshedpur. 3-28.
35. Kemmitt, R.D.W., *37 - MANGANESE*, in *The Chemistry of Manganese, Technetium and Rhenium*. 1973, Pergamon. p. 771-876.
36. Lawson A.C, L.A.C., Aronson M.C, Johnson S, Fisk Z, Canfield P.C, Thompson J.D, von Dreele R.B, *Magnetic and crystallographic order in alpha-manganese.* Journal of Applied Physics 1994. **76**: p. 7049-7051.
37. Karlsen O.B, K.A., Fjellvag H, Ravindran P, Vidya R, Hauback B.C, *Structure and magnetism of the beta-Mn-Co solid solution phase.* Journal of Alloys and Compounds, 2009. **476**: p. 9-13.
38. Wyckoff, R.W.G., *Crystal structures I*. Vol. 1 1963: Interscience Publishers.
39. Hanaor, D.A.H. and C.C. Sorrell, *Review of the anatase to rutile phase transformation.* J Mater Sci, 2011. **46**: p. 855–874.

40. Ghosh, T.B., S. Dhabal, and A.K. Datta, *On crystallite size dependence of phase stability of nanocrystalline TiO2.* Journal of Applied Physics, 2003. **94**(7): p. 4577-4582.
41. Hirano, M., et al., *Photoactivity and phase stability of ZrO2-doped anatase-type TiO2 directly formed as nanometer-sized particles by hydrolysis under hydrothermal conditions.* Journal of Solid State Chemistry, 2003. **170**(1): p. 39-47.
42. Kim, J., et al., *Dopants for synthesis of stable bimodally porous titania.* Journal of the European Ceramic Society, 2001. **21**(16): p. 2863-2872.
43. Berry, R.L. and G.V. Raynor, *The crystal chemistry of the Laves phases.* Acta Crystallographica, 1953. **6**(2): p. 178-186.
44. Bayat, O., A.R. Khavandi, and R. Ghasemzadeh, *Synthesis of TiCr2 intermetallic compound from mechanically activated starting powders via calcio-thermic co-reduction.* Physics of Metals and Metallography, 2017. **118**(5): p. 444-451.
45. Stein, F., M. Palm, and G. Sauthoff, *Structure and stability of Laves phases. Part I. Critical assessment of factors controlling Laves phase stability.* Intermetallics, 2004. **12**(7): p. 713-720.
46. Cupid, D.M., et al., *Thermodynamic assessment of the Cr-Ti and first assessment of the Al-Cr-Ti systems.* Intermetallics, 2011. **19**(8): p. 1222-1235.
47. Filimonov, D.S., Z.K. Liu, and C.A. Randall, *Phase relations in the BaO□TiO2−δ system under highly reducing conditions.* Materials Research Bulletin, 2003. **38**(4): p. 545-553.
48. Lee, S., C. Randall, and Z.-K. Liu, *Modified Phase Diagram for the Barium Oxide–Titanium Dioxide System for the Ferroelectric Barium Titanate*. Vol. 90. 2007. 2589-2594.
49. Aisyah, I.S., et al., *Rapid Transformation of Hexagonal to Cubic Silicon Carbide (SiC) by Electric Discharge Assisted Mechanical Milling.* Plasma Chemistry and Plasma Processing, 2016. **36**(4): p. 1177-1186.
50. Krishna, P. and R.C. Marshall, *The structure, perfection and annealing behaviour of SiC needles grown by a VLS mechanism.* Journal of Crystal Growth, 1971. **9**: p. 319-325.
51. http://www.gordonengland.co.uk/pft.htm.
52. Zhao, N., et al., *Microstructure and kinetics study on tantalum carbide coating produced on gray cast iron in situ.* Surface and Coatings Technology, 2016. **286**: p. 347-353.
53. Trignan-Piot, L., et al., *Influence of plasma spraying parameters on the carbon content and porosity of TaC coatings.* Surface and Coatings Technology, 1996. **79**(1): p. 113-118.
54. Drofenik, M., et al., *Anomalous Grain Growth in Donor-Doped Barium Titanate with Excess Barium Oxide.* Journal of the American Ceramic Society, 2002. **85**(3): p. 653-660.
55. Voisin, C., et al., *Influence of Oxygen Substoichiometry on the Dielectric Properties of BaTiO3-δ Nanoceramics Obtained by Spark Plasma Sintering.* International Journal of Applied Ceramic Technology, 2013. **10**: p. E122-E133.
56. Lin, T.-F., C.-T. Hu, and I.N. Lin, *Influence of Stoichiometry on the Microstructure and Positive Temperature Coefficient of Resistivity of Semiconducting Barium Titanate Ceramics.* Journal of the American Ceramic Society, 1990. **73**(3): p. 531-536.
57. Yu, J., et al., *Giant Dielectric Constant of Hexagonal BaTiO3 Crystal Grown by Containerless Processing.* Chemistry of Materials, 2004. **16**(21): p. 3973-3975.
58. Rheinheimer, W. and M.J. Hoffmann, *Grain growth transitions of perovskite ceramics and their relationship to abnormal grain growth and bimodal microstructures.* Journal of Materials Science, 2016. **51**(4): p. 1756-1765.
59. Bhuiyan, M.R.A., et al., *Synthesis and characterization of barium titanate (BaTiO3) nanoparticle.* IJMME, 2012. **1**: p. 21-24.
60. Ertuğ, B., *The overview of the electrical properties of barium titanate.* Americal journal of engineering research, 2013. **2**(8): p. 2320-0936.

61. Ramoška, T., et al., *Dielectric investigations of La-doped barium titanate*. Vol. 4. 2010.
62. Kim, Y.J., et al., *Microstructural Characterization and Dielectric Properties of Barium Titanate Solid Solutions with Donor Dopants.* Bull. Korean Chem. Soc. , 2009. **30**(6): p. 1267.
63. Vanderah, T.A., J.M. Loezos, and R.S. Roth, *Magnetic Dielectric Oxides: Subsolidus Phase Relations in the BaO:Fe2O3:TiO2System.* Journal of Solid State Chemistry, 1996. **121**(1): p. 38-50.
64. Hennings, D.F.K., R. Janssen, and P.J.L. Reynen, *Control of Liquid-Phase-Enhanced Discontinuous Grain Growth in Barium Titanate.* Journal of the American Ceramic Society, 1987. **70**(1): p. 23-27.
65. Nien, C.-H., et al., *Grain growth in BaTiO3 ceramics assisted by an intergranular glass film.* Ceramics International, 2014. **40**(1, Part A): p. 1051-1058.
66. Kambale, K.R., A.R. Kulkarni, and N. Venkataramani, *"Grain growth kinetics of barium titanate synthesized using conventional solid state reaction route".* Ceram. Int. , 2014. **40** p. 667–673.
67. Brzozowski, E. and M.S. Castro, *Synthesis of barium titanate improved by modifications in the kinetics of the solid state reaction.* Journal of the European Ceramic Society, 2000. **20**(14–15): p. 2347-2351.
68. Pavlović, V.P., et al., *Microstructure evolution and electric properties of mechanically activated BaTiO3 ceramics.* Journal of the European Ceramic Society, 2007. **27**: p. 575-579.
69. Sasirekha, N. and B. Rajesh, *Hydrothermal Synthesis of Barium Titanate: Effect of Titania Precursor and Calcination Temperature on Phase Transition.* Industrial & Engineering Chemistry Research, 2008. **47**(6): p. 1868-1875.
70. Dutta, P.K. and J.R. Gregg, *Hydrothermal synthesis of tetragonal barium titanate (BaTiO3).* Chemistry of Materials, 1992. **4**(4): p. 843-846.
71. Li, W., et al., *Structure and electrical properties of BaTiO3 prepared by sol–gel process.* Journal of Alloys and Compounds, 2009. **482**(1): p. 137-140.
72. Wu, Y., et al., *Notable grain-size dependence of converse piezoelectric effect in BaTiO3 ceramics.* Ceramics International, 2016. **42**(8): p. 9815-9820.
73. Huan, Y., et al., *Grain size effect on piezoelectric and ferroelectric properties of BaTiO3 ceramics.* Journal of the European Ceramic Society, 2014. **34**(5): p. 1445-1448.
74. Phanichphant, N.P.a.S., *"Study on Electrical Properties of Mn-doped 6h-BaTiO3 Ceramics Using Impedance Spectroscopy",.* J. Sci. , (2007). **34**((3)): p. 297-308
75. Murugesan, G., R. Nithya, and S. Kalainathan, *"Hexagonal BaTiO3 (h-BaTiO3) Single Crystal growth by Optical Floating zone technique".* ICMCT, 2014. **6** (3): p. 1633-1636
76. Jaffe, B., W.R. Cook Jr, and H. Jaffe, *Piezoelectric ceramics*, ed. A. Press. 1971.
77. Botther, R., et al., J. Phys. Condens. Matter, 2008. **20**: p. 505209.
78. Yu, J., et al., *Giant Dielectric Constant of Hexagonal BaTiO3 Crystal Grown by Containerless Processing.* Chem. Mater., 2004. **16**(21): p. 3973-3975.
79. Kelly, A. and K.M. Knowles, *Crystallography and crystal defects*. 2012: John Wiley & sons, Ltd.
80. Hippel, A.v., *Ferroelectricity, domain structure and phase transitions of Barium Titanate.* Reviews of physics, 1950. **22**(3): p. 221-237.
81. Maso, N., et al., *Electrical properties of Fe-doped BaTiO3.* J. Mater. Chem. , 2006. **16**: p. 1626-1633.
82. Mishra, A. and N. Mishra, *Iron-doped BaTiO3: Influence of iron on physical properties.* International Journal of Materials Science and Applications., 2012. **1**(1): p. 14-21.

83. Mahbub, R., T. Fakhrul, and M.F. Islam, *Enhanced Dielectric Properties of Tantalum Oxide Doped Barium Titanate based Ceramic Materials.* Procedia Engineering, 2013. **56**: p. 760-765.
84. Li, Z.C. and B. Bergman, *Electrical properties and ageing characteristics of BaTiO3 ceramics doped by single dopants.* Journal of the European Ceramic Society, 2005. **25**(4): p. 441-445.
85. Baranov, A.N. and Y.-J. Oh, *Microwave frequency dielectric properties of hexagonal perovskites in the Ba5Ta4O15–BaTiO3 system.* Journal of the European Ceramic Society, 2005. **25**(15): p. 3451-3457.
86. Tomsia, A.P. and A.M. Glaeser, *Control at the Atomic Level*. Ceramic Microstructures. 1996: Springer.
87. Arend, H. and L. Kihlborg, *Phase composition of reduced and reoxidized Barium Titanate.* Journal of the Americal Ceramic Society, 1969. **52**(2): p. 63-65.
88. Aksenczuk, A., in *EIS*. 2017, University of Wollongong.
89. Kawamoto, T., et al., *Room-Temperature Polar Ferromagnet ScFeO3 Transformed from a High-Pressure Orthorhombic Perovskite Phase.* Journal of the American Chemical Society, 2014. **136**(43): p. 15291-15299.
90. Ram, S., A. Jana, and T.K. Kundu, *Ferroelectric BaTiO3 phase of orthorhombic crystal structure contained in nanoparticles.* Journal of Applied Physics, 2007. **102**(5): p. 054107.
91. Arlt, G., D. Hennings, and G.d. With, *Dielectric properties of fine-grained barium titanate ceramics.* Journal of Applied Physics, 1985. **58**(4): p. 1619-1625.
92. Gallagher, P.K. and F. Schrey, *Thermal Decomposition of Some Substituted Barium Titanyl Oxalates and Its Effect on the Semiconducting Properties of the Doped Materials.* Journal of the American Ceramic Society, 1963. **46**(12): p. 567-573.
93. Yen, F.-S., C.T. Chang, and Y.-H. Chang, *Characterization of Barium Titanyl Oxalate Tetrahydrate.* Journal of the American Ceramic Society, 1990. **73**(11): p. 3422-3427.
94. Orlandi, M.O., et al., *Carbothermal Reduction Synthesis: An Alternative Approach to Obtain Single-Crystalline Metal Oxide Nanostructures*, in *Recent Advances in Complex Functional Materials: From Design to Application*, E. Longo and F.d.A. La Porta, Editors. 2017, Springer International Publishing: Cham. p. 43-67.
95. Sinclair, D.C., et al., *Structure and electrical properties of oxygen-deficient hexagonal BaTiO3.* Journal of Materials Chemistry, 1999. **9**(6): p. 1327-1331.
96. Dewan, M.A.R., G. Zhang, and O. Ostrovski, *Carbothermal Reduction of Titania in Different Gas Atmospheres.* Metallurgical and Materials Transactions B, 2009. **40**(1): p. 62-69.
97. Gorelov, B.M., et al., *Adsorption of water molecules on yttrium barium cuprate superconductors.* Technical Physics, 2000. **45**(9): p. 1147-1153.
98. Shannon, R.D. and J.A. Pask, *Kinetics of the Anatase-Rutile Transformation.* Journal of the American Ceramic Society, 1965. **48**(8): p. 391-398.
99. Riyas, S., G. Krishnan, and P.N.M. Das, *Anatase–rutile transformation in doped titania under argon and hydrogen atmospheres.* Advances in Applied Ceramics, 2007. **106**(5): p. 255-264.
100. Zhang, Q., T. Cagin, and W.A. Goddard, *The ferroelectric and cubic phases in BaTiO(3) ferroelectrics are also antiferroelectric.* Proceedings of the National Academy of Sciences of the United States of America, 2006. **103**(40): p. 14695-14700.
101. Mnyukh, Y., *Fundamentals of Solid-State Phase Transitions, Ferromagnetism and Ferroelectricity,*. 2nd (2010) Edition ed. (2001): Authorhouse.

102. Gomez-Yañez, C., C. Benitez, and H. Balmori-Ramirez, *Mechanical activation of the synthesis reaction of BaTiO3 from a mixture of BaCO3 and TiO2 powders.* Ceramics International, 2000. **26**(3): p. 271-277.
103. Brzozowski, E. and M.S. Castro, *Synthesis of barium titanate improved by modifications in the kinetics of the solid state reaction.* J. Eur. Ceram. Soc. , 2000. **20**: p. 2347-2351.
104. Malis, T. and H. Gleiter, *On the structure of the ferroelectric-paraelectric transformation interface in barium titanate. I. Basic structure and characteristics.* Journal of Applied Physics, 1979. **50**(7): p. 4920-4923.
105. Burbank, R.D. and H.T. Evans, *'The Crystal Structure of Hexagonal BaTiO3.* Acta Crystallogr., 1948. **1**: p. 330–6.
106. Wu, Y.-C. and H.-Y. Lu, *Crystallographic Orientation Relationships Between Hexagonal and Tetragonal Barium Titanate.* Journal of the American Ceramic Society, 2005. **88**(11): p. 3154-3161.
107. Zheng, S.J., et al., *TEM and STEM investigation of grain boundaries and second phases in barium titanate.* Philosophical Magazine, 2007. **87**(34): p. 5447-5459.
108. Burbure, N.V., P.A. Salvador, and G.S. Rohrer, *Orientation and Phase Relationships between Titania Films and Polycrystalline BaTiO3 Substrates as Determined by Electron Backscatter Diffraction Mapping.* Journal of the American Ceramic Society, 2010. **93**(9): p. 2530-2533.
109. Komolwit, P., *The Effect of Cobalt and Carbon the Microstructure and Mechanical Properties of Martensitic Precipitation Strengthened Stainless Steels*. 2009, Carnegie Mellon University: Pittsburgh.
110. Kumagai, T., et al., *Microstructural evolution of massively transformed γ-TiAl during isothermal aging.* Scripta Materialia, 1997. **36**(5): p. 523-529.
111. Sharma, G., R.V. Ramanujan, and G.P. Tiwari, *Interphase precipitation in a γ-TiAl alloy.* Materials Science and Engineering: A, 1999. **269**(1): p. 21-25.
112. Kumagai, T., et al., *The γ → α phase transformation in γ-based TiAl alloy.* Scripta Materialia, 1996. **34**(2): p. 235-242.
113. Kang, J.H., et al., *Effect of external stress on the orientation distribution of ferrite.* Scripta Materialia, 2003. **48**(1): p. 91-95.
114. Li, Y., L. Wan, and K. Chen, *A look-up table based approach to characterize crystal twinning for synchrotron X-ray Laue microdiffraction scans.* Journal of Applied Crystallography, 2015. **48**(Pt 3): p. 747-757.
115. Koumatos, K. and A. Muehlemann, *A theoretical investigation of orientation relationships and transformation strains in steels.* Acta Crystallographica Section A, 2017. **73**(2): p. 115-123.
116. Barbier, D., et al., *EBSD for analysing the twinning microstructure in fine-grained TWIP steels and its influence on work hardening.* Journal of Microscopy, 2009. **235**(1): p. 67-78.
117. Yang, P., *Dependency of deformation twinning on grain orientation in an FCC and a HCP metal.* Frontiers of Materials Science in China, 2007. **1**(4): p. 331-341.
118. Rampton, T.M., *Deformation Twin Nucleation and Growth Characterization in Magnesium Alloys Using Novel EBSD Pattern Analysis and Machine Learning Tools*, in *Department of Mechanical Engineering*. 2015, Brigham Young University Provo.
119. Krakow, R., et al., *On three-dimensional misorientation spaces.* Proceedings. Mathematical, Physical, and Engineering Sciences, 2017. **473**(2206): p. 20170274.
120. Mason, J.K. and C.A. Schuh, *The generalized Mackenzie distribution: Disorientation angle distributions for arbitrary textures.* Acta Materialia, 2009. **57**(14): p. 4186-4197.

121. Kurdjumow, G. and G. Sachs, *Über den Mechanismus der Stahlhärtung.* Zeitschrift für Physik, 1930. **64**(5): p. 325-343.
122. Verbeken, K., et al., *Evaluation of the Crystallographic Orientation Relationships between FCC and BCC Phases in TRIP Steels.* ISIJ International, 2009. **49**(10): p. 1601-1609.
123. Miyamoto, G., N. Takayama, and T. Furuhara, *Accurate measurement of the orientation relationship of lath martensite and bainite by electron backscatter diffraction analysis.* Scripta Materialia, 2009. **60**(12): p. 1113-1116.
124. Kirby, K.W. and B.A. Wechsler, *Phase relations in the Barium Titanate—Titanium Oxide System.* Journal of the American Ceramic Society, 1991. **74**(8): p. 1841-1847.
125. Ashiri, R., *On the solid-state formation of BaTiO3 nanocrystals from mechanically activated BaCO3 and TiO2 powders: innovative mechanochemical processing, the mechanism involved, and phase and nanostructure evolutions.* Royal Society of Chemistry, 2016. **6**: p. 17138–17150.

Appendices

Appendix A: Description of cubic crystal structure

Space group (No., Name)	Lattice parameters a	b	c	α	β	γ
221, Pm − 3m	4.006	4.006	4.006	90.000	90.000	90.000

Structure parameters Atom	Descr.	x	y	z	Occ.	Wp	Sym.
Ba	Ba1	0.500	0.500	0.500	1.000	1b	m-3m
Ti	Ti1	0.000	0.000	0.000	1.000	1a	m-3m
O	O1	0.500	0.000	0.000	1.000	3d	4/mm.m

Appendix B:

Space group (No., Name)	Lattice parameters a	b	c	α	β	γ
194, P63 /mmc	5.7238	5.7238	13.9649	90.000	90.000	120.000

Structure parameters Atom	Descr.	x	y	z	Occ.	Wp	Sym.
Ba	Ba1	0.000	0.000	0.250	1.000	2b	-6m2
Ba	Ba2	0.333	0.667	0.097	1.000	4f	3m.
Ti	Ti1	0.000	0.000	0.000	1.000	2a	-3m.
Ti	Ti2	0.333	0.667	0.846	1.000	4f	3m
O	O1	0.519	0.037	0.250	1.000	6h	mm2
O	O2	0.835	0.670	0.080	1.000	12k	.m.

Appendix C:

Space group (No., Name)	Lattice parameters a	b	c	α	β	γ
12, C12/m1	15.0040	3.9530	9.0850	90.000	98.010	90.000

Structure parameters Atom	Descr.	x	y	z	Occ.	Wp	Sym.
Ba	Ba1	0.448	0.000	0.222	1.000	4i	m
Ti	Ti1	0.122	0.000	0.100	0.333	4i	m
Ti	Ti2	0.122	0.000	0.100	0.667	4i	m
Ti	Ti3	0.169	0.000	0.444	0.333	4i	m
Ti	Ti4	0.169	0.000	0.444	0.667	4i	m
Ti	Ti5	0.248	0.000	0.777	0.333	4i	m
Ti	Ti6	0.248	0.000	0.777	0.667	4i	m
O	O1	0.000	0.000	0.000	1.000	4i	2/m
O	O2	0.241	0.000	0.247	1.000	4i	m
O	O3	0.072	0.000	0.301	1.000	4i	m
O	O4	0.299	0.000	0.571	1.000	4i	m
O	O5	0.129	0.000	0.619	1.000	4i	m
O	O6	0.373	0.000	0.888	1.000	4i	m
O	O7	0.171	0.000	0.917	1.000	4i	m